The biogeochemistry of particulate trace elements and isotopes in the North Atlantic Ocean

Pamela M. Barrett

A dissertation

submitted in partial fulfillment of the

requirements for the degree of

Doctor of Philosophy

University of Washington

2015

Reading Committee:

Joseph A. Resing, Chair

James W. Murray

Bruce K. Nelson

Program Authorized to Offer Degree:

School of Oceanography

University of Washington

Abstract

The biogeochemistry of particulate trace elements and isotopes in the North Atlantic Ocean

Pamela M. Barrett

Chair of Supervisory Committee:
Dr. Joseph A. Resing, Affiliate Assistant Professor
School of Oceanography

The distributions and bioavailability of trace metals and their isotopes are strongly controlled by partitioning between the dissolved phase and suspended and sinking biotic and abiotic particles. This work presents new particulate trace element data from CLIVAR section A16N in the North Atlantic collected during two occupations in 2003 and 2013. ED-XRF methods were adapted for trace element analysis of marine suspended particulate matter at sub-nanomolar concentrations. Paired analyses of particulate Al, P, Ca, V, Mn, Fe, Ni, Cu, Zn, and Pb concentrations using samples collected from the upper water column in the Atlantic and Pacific Oceans show that ED-XRF and HR ICP-MS methods produce comparable data for many trace elements of oceanographic interest. By quantifying changes in the concentrations of subsurface particulate Al and Fe and mixed-layer dissolved Al in the equatorial North Atlantic, we estimate dust deposition to surface waters in the eastern North Atlantic increased by approximately 15% between 2003 and 2013. Increased concentrations of dissolved Al in subtropical mode waters suggest that dust deposition may have also increased in the western basin. Particulate calcium distributions and total alkalinity measurements along A16N in 2003 and 2013 were used to estimate shallow-water carbonate dissolution. In the tropical North Atlantic, water masses at

intermediate depths were undersaturated with respect to aragonite. Carbonate dissolution rates were estimated to be 0.7–0.9 mmol m^{-2} d^{-1}, indicating this region is a hotspot for shallow carbonate dissolution in the Atlantic basin. Finally, the enriched $\delta^{65}Cu$ of particulate matter samples suggests that adsorptive and passive scavenging processes likely dominate the fractionation of Cu stable isotopes in the upper ocean and result in isotopically heavy particulate Cu. Incorporating this new data into an isotopic mass balance for Cu in the surface ocean, we estimate an atmospheric flux of 1.2 x 10^8 mol Cu yr^{-1} to the surface ocean and a particle export flux from the base of the mixed layer of 2.6 x 10^9 mol Cu yr^{-1}.

Acknowledgements

I would like to thank my advisor, Joe Resing, for his mentorship and encouragement to pursue diverse professional and personal opportunities throughout my graduate career. I would also like to thank the members of my doctoral committee for their valuable guidance: Jim Murray, Dick Feely, Chuck Nittrouer, and Bruce Nelson.

This research would not have been possible without the contributions of many individuals, including: Nathan Buck at the Joint Institute for the Study of the Atmosphere and Ocean; John Bullister at the Pacific Marine Environmental Laboratory; Peter Morton, Rachel Shelley, and Bill Landing at Florida State University; Chris Measures at the University of Hawaii; Bruce Nelson and Scott Kuehner at the University of Washington Isotope Geochemistry Laboratory; Cheryl Zurbrick at the University of California, Santa Cruz. I also thank the CLIVAR/CO_2 Repeat Hydrography Program and the science party, captain, and crew of the *NOAA Ship Ronald H. Brown* during the 2013 occupation of A16N.

I would also like to thank the University of Washington Program on Climate Change and the University of Washington IGERT Program on Ocean Change for providing an interdisciplinary community as well as academic and research opportunities that greatly enriched my degree program.

Finally, I'd like to thank the family and friends who have provided endless support, humor, and love during my graduate work, most of all my husband David.

Funding for this research was provided by the Joint Institute for the Study of the Atmosphere and Ocean (JISAO), the National Oceanic and Atmospheric Administration, the University of Washington School of Oceanography, the University of Washington IGERT Program on Ocean Change, and the National Science Foundation.

Table of Contents

List of Tables

List of Figures

Chapter 1: Introduction

1.1 Background and motivation

Trace metals such as Mn, Fe, Zn, Ni, Co, Cu, and Cd are all required micronutrients for phytoplankton, utilized in various metalloenzymes involved in photosynthesis, respiration, and nitrogen fixation [*Morel et al.*, 2003]. Hence, the distribution of bioavailable trace metals in the marine environment exerts important controls on ocean productivity and carbon sequestration. Most notably, the availability of Fe in the euphotic zone has been shown to limit phytoplankton growth and ocean carbon uptake in vast high nutrient, low chlorophyll regions of the world ocean [*Boyd et al.*, 2007]. At sufficiently high concentrations, trace metal toxicity can also suppress phytoplankton productivity as in the case of Cu and Cd [*Brand et al*., 1986; *Tortell and Price,* 1996; *Paytan et al.*, 2009].

The distribution and bioavailability of trace metals is strongly controlled by partitioning between the dissolved phase and suspended and sinking biotic and abiotic particles [e.g., *Quay et al*., 2015]. The supply of trace metals to the open ocean is often dominated by the particulate phase and the dynamic cycling of trace metals in the ocean interior is largely mediated by rates of biological uptake, passive scavenging, and particle aggregation/disaggregation, degradation and sinking rates. Although observations of trace elements and their isotopes in the global ocean have greatly increased in the last decade with improvements in analytical techniques and the launch of dedicated global sampling programs (i.e., CLIVAR, GEOTRACES), the availability of particulate trace element datasets is still relatively sparse. Increased observations of the distribution and trace element composition of marine particulate matter is needed to better understand the biogeochemical cycling of key trace metals that modulate primary productivity and improve parameterizations for global models of ocean carbon cycling and past and future climate.

1.2 Role of particulate matter in marine trace metal cycling

Major input pathways for biologically-important trace metals to the remote open ocean such as atmospheric deposition of aerosols [*Duce et al.*, 1991] and transport from benthic and shelf sediments [*Lam and Bishop*, 2008] are primarily associated with the particulate phase. Particulate trace metals also originate from active biological uptake, passive scavenging processes, and authigenic mineral formation in the marine environment. Particulate trace metals cycle through the dissolved and colloidal pools, typically thought to be the most bioavailable phases, through dissolution, disaggregation, and desorption processes, although studies have also suggested that the particulate fraction may also be directly available to phytoplankton [*Hurst and Bruland*, 2007]. The source and composition of biotic and

abiotic particles (e.g., $CaCO_3$, biogenic silica, lithogenic minerals, organic carbon) is also an important control on the cycling of trace metals. The affinity of individual elements for a specific particle composition will determine the relative scavenging pressures on particle-reactive trace metals [*Chase et al*., 2002]. For example, significant particulate Al signals in the surface ocean have been shown to arise from the preferential scavenging of dissolved Al by siliceous diatom frustules [*Moran and Moore*, 1988; *Barrett et al*., 2012; *Twining et al*., 2015]. The removal of particle-associated trace elements from the ocean is also expected to vary as a function of the ballasting efficiency and sinking rates of the various major particle phases.

The factors that determine patterns of inputs, cycling and removal of trace metals in the oceans are all subject to anthropogenic impacts and changing climate. For example, supply of aerosol trace metals on the surface ocean is sensitive to wind strength and changing precipitation patterns in both continental aerosol source regions and over the open ocean [*Jickells et al*., 2005]. The distribution of particulate biogenic $CaCO_3$ and silica will depend on phytoplankton productivity and community composition in a future warmer, CO_2-rich ocean with a modified temperature structure, nutrient supply, and carbonate saturation state. In turn, changes in the supply and distribution of trace metals feed back on global climate by modulating ocean productivity and carbon uptake.

The North Atlantic Ocean encompasses diverse geochemical provinces with varying levels of primary production and both natural lithogenic and anthropogenic particulate trace metal inputs, making the North Atlantic an effective study area for investigating the role of particulate matter in the cycling of trace elements. The annual spring phytoplankton bloom in the sub-polar and temperate North Atlantic is responsible for approximately 20% of the global ocean uptake of CO_2 [*Mahadevan et al*., 2012]. Here, high levels of primary productivity produce high densities of rapidly-sinking biogenic particles [*Honjo and Manganini*, 1993] and result in significant uptake of biologically-important trace metals, including iron, which is likely drawn down to levels that may be seasonally iron-limiting. The high particle density also exerts strong scavenging pressures on particle-reactive trace metals in the mixed layer and the formation of biological aggregates likely facilitates efficient vertical transport of particulate trace elements. Additionally, significant loads of lithogenic particles are delivered to surface waters in the North Atlantic via atmospheric deposition of aerosol dust, representing up to 50% of the total dust flux to the global ocean [*Mahowald et al.*, 1999; *Jickells et al*., 2005]. Previous studies have shown that distributions of Fe and Al in the upper water column in the tropical and subtropical North Atlantic are largely controlled by patterns of atmospheric deposition of mineral dust on the surface ocean [*Measures*

et al., 2008; *Barrett et al*., 2012; *Ohnemus and Lam,* 2015]. The North Atlantic also receives significant particulate trace metal inputs from anthropogenic sources. In mid- and high-latitude waters, trace metal distributions are affected by aerosol pollution deriving from fossil fuel combustion in industrialized Europe and North America [*Buck et al*., 2010; *Barrett et al*., 2012] while anthropogenic inputs at low latitudes are expected to be primarily impacted by biomass burning on the African continent [*Luo et al*., 2008; *Chin et al*., 2013].

This work uses new particulate trace element data from the CLIVAR CO_2/Repeat Hydrography transect A16N between ~60°N and the equator in the eastern North Atlantic during two occupations in 2003 and 2013 to address the following questions: What are the distributions of lithogenic (Fe and Al) and biogenic ($CaCO_3$) particulate trace elements in the North Atlantic and how may these be changing on decadal timescales in response to changing climate? What is the isotopic composition of particulate Cu ($\delta^{65}Cu$) and how does the isotopic fractionation between dissolved and particulate Cu affect the isotopic mass balance of Cu in the global ocean? The high-resolution datasets of particulate trace metal distributions and particulate Cu isotopic data generated represent significant expansions of particulate trace metal observations in the literature.

1.3 Research overview

Chapter 2 describes the development of a thin-film energy-dispersive x-ray fluorescence method adapted from prior approaches [*Feely et al*., 1991] for analysis of the trace element composition of marine suspended particulate matter at the sub-nanomolar concentrations typical of open-ocean surface waters. Also presented are results from comparison of ED-XRF results to analysis of samples by high-resolution inductively coupled plasma-mass spectrometry (HR-ICPMS) for a suite of trace elements of oceanographic interest (Al, P, Ca, Ti, V, Mn, Fe, Ni, Cu, Zn, Sr, and Pb).

Chapter 3 examines the trace metal composition of suspended particulate matter from high-resolution sampling in the upper 1000 m along the CLIVAR meridional transect A16N in the eastern North Atlantic Ocean from repeat occupations in 2003 and 2013. This work examines large-scale features in the particulate Fe and dissolved and particulate Al distributions arising from mineral aerosol deposition on surface waters in the equatorial and sub-tropical regions [*Measures et al.*, 2008; *Barrett et al.,* 2012]. Increases in the particulate trace metal concentrations in these dust-driven features between the two occupations of A16N suggest that dust deposition likely increased by ~20% over the last decade. These observations of increased inventories of particulate Fe and Al in the upper water column support recent work linking declining aerosol optical depth over the North Atlantic during this time period to

shifts in precipitation patterns [*Chin et al.*, 2013], suggesting increased aerosol delivery to the surface ocean is occurring mainly due to wet deposition processes and highlighting the importance of accurate representation of dust deposition processes for modelling Fe biogeochemistry. Chapter 3 has been published in *Marine Chemistry* with co-authors Joseph Resing, Nathan Buck, William Landing, Peter Morton, and Rachel Shelley [*Barrett et al*., in press].

Chapter 4 presents the distribution of biogenic $CaCO_3$ from high-resolution particulate matter sampling along A16N and reports estimates for shallow-water carbonate dissolution in the North Atlantic. High dissolution rates in the eastern (sub)tropical North Atlantic (0.8–0.9 mmol $CaCO_3$ m^{-2} d^{-1}) indicate a hotspot for carbonate dissolution in intermediate water masses undersaturated with respect to aragonite. These dissolution rates are comparable to estimates determined from total alkalinity distributions and suggest that biologically-mediated processes may contribute to shallow-water carbonate dissolution. Analysis of particulate trace element distributions from the repeat occupation of A16N in 2013 reveals that overall levels of biological production and $CaCO_3$ inventories were significantly higher than those observed in 2003, although within the range of expected interannual variation. Rates of carbonate dissolution are similar to those estimated a decade earlier in the corrosive intermediate waters of the (sub)tropical ocean. The majority of the work presented in this chapter has been published in *Global Biogeochemical Cycles* with co-authors Joseph Resing, Nathan Buck, Richard Feely, John Bullister, Clifton Buck, and William Landing [*Barrett et al*., 2014].

Chapter 5 reports the stable isotope composition ($\delta^{65}Cu$) of particulate Cu in the North Atlantic to address previous studies that have reached contradictory conclusions about the effects of both active biological uptake and passive particle adsorption of Cu on seawater $\delta^{65}Cu$ values. In this work, we find that both active uptake by phytoplankton and adsorptive processes likely fractionate seawater Cu, resulting in an isotopically heavy particulate Cu pool. We also find isotopic variation in particulate Cu values in near-surface samples suggesting influence of anthropogenic Cu sources on seawater $\delta^{65}Cu$. Finally, an updated isotopic mass balance integrates new particulate Cu isotopic data to constrain the atmospheric flux of Cu to the global ocean.

1.4 References

Barrett, P.M., Resing, J.A., Buck, N.J., Buck, C.S, Landing, W.M., Measures, C.I., 2012. The trace element composition of suspended particulate matter in the upper 1000 m of the eastern North Atlantic Ocean: A16N. Mar. Chem. 142–144, 41–53.

Barrett, P.M., Resing, J.A., Buck, N.J., Feely, R.A., Bullister, J., Buck, C.S., Landing, W.M., Measures, C.I., 2014. Calcium carbonate dissolution in the upper 1000 m of the eastern North Atlantic. Global Biogeochem. Cycles 28, 386–397.

Barrett, P.M., Resing, J.A., Buck, N.J., Landing, W.M., Morton, P.L., Shelley, R.U., 2015. Changes in the distribution of Al and Fe along A16N in the eastern North Atlantic Ocean between 2003 and 2013: Implications for changes in dust deposition. Mar. Chem. in press, doi:10.1016/j.marchem.2015.02.009.

Boyd, P.W., Jickells, T., Law, C.S., Blain, S., Boyle, E.A., Buesseler, et al., 2007. Mesoscale Iron Enrichment Experiments 1993-2005: Synthesis and Future Directions. Science 315, 612-617.

Brand, L.E., Sunda, W.G., Guillard, R.R.L., 1986. Reduction of marine phytoplankton reproduction rates by copper and cadmium. J. Exp. Mar. Biol. Ecol. 96, 225–250.

Buck, C.S., Landing, W.M., Resing, J.A., Measures, C.I., 2010. The solubility and deposition of aerosol Fe and other trace elements in the North Atlantic Ocean: observations from the A16N CLIVAR/CO_2 repeat hydrography section. Mar Chem. 120, 57–70.

Chase, Z., Anderson, R.F., Fleisher, M.Q., Kubik, P.W., 2002. The influence of particle composition and particle flux on scavenging of Th, Pa and Be in the ocean. Earth Planet. Sci. Lett. 204, 215–229.

Chin, M., T. Diehl, Q. Tan, J.M. Prospero, R.A. Kahn, L.A. Remer, H. Yu, A.M. Sayer, H. Bian, I.V. Geogdzhayev, B.N. Holben, S.G. Howell, B.J. Huebert, N.C. Hsu, D. Kim, D.L. Kucsera, R.C. Levy, M.I. Mishchenko, X. Pan, P.K. Quinn, G.L. Schuster, D.G. Streets, S.A. Strode, O. Torres, and X.-P. Zhao, 2013: Multi-decadal variations of atmospheric aerosols from 1980 to 2009: sources and regional trends. Atmos. Chem. Phys. Discuss. 13, 19751–19835.

Conway, T.M., John, S.G., 2014. Quantification of dissolved iron sources to the North Atlantic Ocean. Nature 511, 212–215.

Duce, R.A., Liss, P.S., Merrill, J.T., Atlas, E.L., Buat-Menard, P., Hicks, B.B., et al., 1991. The atmospheric input of trace species to the world ocean. Global Biogeochem. Cycles 5, 193–259.

Feely, R.A., Massoth, G.J., Lebon, G.T., 1991. Sampling of marine particulate matter and analysis by x-ray fluorescence spectrometry. In: Hurd, D.C. and Spencer, D.W. (eds.), Marine Particles: Analysis and Characterization, AGU Geophysical Monograph Series, p. 251-257.

Honjo, S., Manganini, S.J., 1993. Annula biogenic particle fluxes to the interior of the North Atlantic Ocean; studied at 34N 21W and 48N 21W. Deep Sea Res. II 40, 587 –607.

Hurst, M.P., Bruland, K.W., 2007. An investigation into the exchange of iron and zinc between soluble,

colloidal, and particulate size-fractions in shelf waters using low-abundance isotopes as tracers in shipboard incubation experiments. Mar. Chem. 103, 211–226.

Jickells, T.D., An, Z.S., Andersen, K.K., Baker, A.R., Bergametti, G., Brooks, N., Cao, J.J., Boyd, P.W., Duce, R.A., Hunter, K.A., Kawahata, H., Kubilay, N., laRoche, J., Liss, P.S., Mahowald, N., Prospero, J.M., Ridgwell, A.J., Tegen, I., Torres, R., 2005. Global iron connections between desert dust, ocean biogeochemistry, and climate. Science 308, 67–71.

Lam, P.J., Bishop, J.K.B., 2008. The continental margin is a key source of iron to the HNLC North Pacific Ocean. Geophys. Res. Lett. 35, L07608.

Luo, C., Mahowald, N., Bond, T., Chuang, P.Y., Artaxo, P., Seifert, R., Chen, Y., Schauer, J., 2008. Combustion iron distribution and deposition. Global Biogeochem. Cycles 22, GB1012.

Mahadevan, A., D'Asaro, E., Lee, C., Perry, M.J., 2012. Eddy-Driven Stratification Initiates North Atlantic Spring Phytoplankton Blooms. Science 337, 54–58.

Measures, C.I., Landing, W.M., Brown, M.T., Buck, C.S., 2008. High-resolution Al and Fe data from the Atlantic Ocean CLIVAR-CO2 Repeat Hydrography A16N transect: Extensive linkages between atmospheric dust and upper ocean geochemistry. Global Biogeochem. Cycles 22, GB1005.

Moran, S.B., Moore, R.M., 1988. Temporal variations in dissolved and particulate aluminum during a spring bloom. Estuar. Coast. Shelf Sci. 27, 205–215.

Morel, F.M.M., Milligan, A.J., Saito, M.A., 2003. Marine Bioinorganic Chemistry: The Role of Trace Metals in the Oceanic Cycles of Major Nutrients. In: Turekian, K.K. and Holland, H.D., Eds., Treatise on Geochemistry, Elsevier Science Ltd., Cambridge, United Kingdom.

Ohnemus, D.C., Lam, P.J., 2015. Cycling of lithogenic marine particles in the US GEOTRACES North Atlantic transect. Deep-Sea Res. II 116, 283–302.

Paytan, A., K.R.M. Mackey, Y. Chen, I.D. Lima, S.C. Doney, N. Mahowald, R. Labiosa, A.F. Post, 2009. Toxicity of atmospheric aerosols on marine phytoplankton. Proc. Nat. Acad. Sci. 106, 4601–4605.

Ryan-Keough, T.J., Thomas, J., Macey, A.I., Nielsdottir, M.C., Lucas, M.I., Steigenberger, S.S., Stinchcombe, M.C., Achterberg, E.P., Bibby, T.S., Moore, C.M., 2013. Spatial and temporal development of phytoplankton iron stress in relation to bloom dynamics in the high-latitude North Atlantic. Limnol. Oceanogr. 58, 533–545.

Tortell, P.D., Price, N.M., 1996. Cadmium toxicity and zinc limitation in centric diatoms of the genus Thalassiosira. Mar. Ecol. Prog. Ser. 138, 245–254.

Twining, B.S., Rauschenberg, S., Morton, P.L., Vogt, S., 2015. Metal contents of phytoplankton. Prog. Oceanogr. 137, 261–283.

Quay, P., Cullen, J., Landing, W., Morton, P., 2015. Processes controlling the distributions of Cd and PO_4 in the ocean. Global Biogeochem. Cycles 29, 830–841.

Chapter 2: ED-XRF analysis of marine suspended particulate matter for trace element composition: Method development and intercomparison with HR ICP-MS

2.1 Introduction

The distribution of particulate trace metals in the oceans reflects patterns of atmospheric, fluvial, and hydrothermal inputs, biological uptake, particle scavenging, and vertical transport through the water column. For many biologically-important trace elements, such as Fe, the particulate phase dominates total trace metal concentrations and adsorptive/desorptive interactions of trace metals with particles in the water column can control the distribution of the dissolved phase, which is typically considered to be the bioavailable pool. Observations of the chemical composition and distribution of marine suspended particulate matter are crucial to improved understanding of the biogeochemical cycling of trace elements in the oceans. The launch of dedicated trace metal sampling programs such as GEOTRACES (http://www.geotraces.org/) has focused attention on the present scarcity of marine particulate trace metal datasets. Further investigation of marine particulate trace element distributions are necessary to advance understanding of the biogeochemical cycles of trace elements and their interactions with changing climate.

Energy-dispersive X-ray fluorescence (ED-XRF) methods have previously been developed for analysis of marine particulate matter [*Feely et al.*, 1991]. Samples are collected as a thin film onto a filter and then exposed to X-rays; the characteristic fluorescence spectra of individual trace elements in the sample is then detected and quantified. Another common technique for trace element analysis of marine particulate matter is High-resolution Inductively Coupled Plasma-Mass Spectrometry (HR ICP-MS) [*Cullen et al*., 2001; *Krachler*, 2007; *Bowie et al.,* 2010; *Planquette and Sherrell*, 2012; *Lam et al.*, 2015]. HR ICP-MS methods typically have low detection limits for a wide range of elements of oceanographic interest. However, particulate matter samples must undergo a digestion procedure prior to analysis which may have incomplete recovery efficiencies or introduce processing blanks [*Cook et al*., 1997; *Bowie et al*., 2010]. A major advantage of analysis of marine particulate matter by ED-XRF is the minimal amount of sample preparation and processing that is required and the non-destructive character of the technique. By eliminating the need for a digestion step, the risk of contamination is minimized and uncertainties associated with the recovery efficiency of digestion techniques are eliminated. Although ED-XRF methods typically have detection limits higher than those attainable with HR ICP-MS methods, trace element analysis by ED-XRF has previously been successfully applied to analysis of marine particulate samples from coastal and hydrothermal vent environments [*Feely et al*., 1991].

This work describes the adaptation of ED-XRF methodologies for analysis of marine suspended particulate matter from open-ocean environments with low trace element concentrations. To accomplish this, it was necessary to develop low-level ED-XRF calibration standards to improve detection limits for particulate Fe. Then, results of ED-XRF analysis of open-ocean particulate matter from the upper water column in the Atlantic and Pacific basins for Al, P, Ca, V, Mn, Fe, Ni, Cu, Zn, and Pb concentrations are presented and compared to HR ICP-MS analysis of the same sample set. This work represents an effort to compare ED-XRF to another common analytical technique to allow comparison of particulate trace metal datasets being produced by different investigators from global-scale trace metal sampling programs such as CLIVAR and GEOTRACES.

2.2 Methods

2.2.1 Sample collection

Suspended particulate matter (SPM) samples used in this study (n = 14) include upper water column samples from open-ocean sites in both the North Atlantic and North Pacific and the Lau basin hydrothermal vent field in the South Pacific (**Fig. 2.1**). Open-ocean SPM samples were collected in the upper 1000 m of the water column along the U.S. CLIVAR/CO_2 Repeat Hydrography program Atlantic meridional transect A16N between Reykjavik, Iceland and Natal, Brazil (June–August 2003) and Pacific zonal transect P2 between Yokohama, Japan and San Diego, CA (June–August 2004). Suspended particulate matter samples from hydrothermal vent field sites were collected over the West Mata volcano and in the Tonga Trench at depths of 1100 to 2000 m during the NE Lau basin cruise KM1008 in May 2010 (**Table 2.1**).

The seawater sampling system used to collected open-ocean SPM samples along both CLIVAR transects is described in detail by *Measures et al.* [2008]. Briefly, seawater was collected using 12 L GO-FLO bottles mounted on a trace metal-clean rosette from the surface to 750–1000 m and processed in a clean laboratory van equipped with a HEPA filtered air system. Suspended particulate matter was collected by pressure-filtering (<55 kPa, filtered compressed air) seawater through acid-washed, 0.4 µm track-etched, polycarbonate filters and backing filters of mixed cellulose ester to facilitate even sample loading in polypropylene filter holders. Filters were rinsed with deionized water adjusted to pH 8 with ammonium hydroxide with a low vacuum applied to remove residual seasalt while avoiding loss or redistribution of particles. The average sample filtration volume was 8 L. Sampling procedures for vent

samples were similar to those described above with the exception of the use of a laboratory van; after collection, filter samples were rinsed and processed in a dedicated trace-element flow hood.

2.2.2 ED-XRF method

The composition of total suspended matter filters samples was analyzed by energy-dispersive X-ray fluorescence (ED-XRF) at the Pacific Marine Environmental Laboratory in Seattle, WA. ED-XRF analysis was conducted under a vacuum atmosphere using thin film principles on a Thermo Fisher Quant'X equipped with a Rhodium Target X-Ray tube and an electronically-cooled, lithium-drifted solid state detector. X-rays for primary sample excitation were passed through graphite filters for optimum control of peak-to-background ratios (**Table 2.2**).

The minimum determination limit (MDL) for individual elements is defined as 3 times the square root of the background intensity measured from a standard of known concentration:

$$MDL = (3 * \sqrt{I_b})/(I_p/c) \qquad (2.1)$$

where I_b is the background intensity, I_p is the peak intensity, and c is the concentration of the standard.

Four separate ED-XRF QA/QC procedures are conducted on a daily, weekly and monthly basis. First, a daily energy adjustment is performed for an energy channel alignment of the Quant'X. Second, ongoing weekly calibration verification is also run using a series of multi-element samples to monitor machine drift. Reference material NIST SRM 2783, air particulate on filter media, is analyzed on a monthly basis to monitor recovery of individual elements. Lastly, a monthly analysis of 10 acid washed blank filters is run for accurate background determination and monitoring.

2.2.3 ED-XRF calibration

Calibration of the ED-XRF was performed using commercial thin film standards (MicroMatter) and a series of standards prepared using a modification of the method reported by *Holynska and Bisiniek* [1976] that employs diethyldithiocarbamate (DDTC) to quantitatively precipitate trace metals from a solution of known concentration. MicroMatter standards were used to create individual calibration curves for all elements; calibration of Fe also included NaDDTC standards.

In order to accurately measure the low particulate Fe concentrations typically present in open-ocean surface seawater samples (< 5 nmol L^{-1}) on small-volume filter samples (<10 L), the minimum determination limit of the ED-XRF method described above was improved with the addition of low-

concentration calibration standards for Fe (< 1000 ng cm^{-2}). Standards prepared from thin-film deposits of certified geochemical reference materials have been successfully used for ED-XRF calibration in previous reports [*Feely et al.*, 1999]. In this approach, a known quantity of reference material is suspended in a pH-adjusted solution and then loaded onto the specific filter type used for sample acquisition. However, at small masses, heterogeneity in the reference material may reduce the precision of replicate analyses [*Korotev*, 1987]. There is also concern that selective dissolution of individual elements when the sample is suspended for filtration onto the reference filter may introduce significant uncertainty at small mass loadings. To avoid these potential complications, the methods of *Holynska and Bisiniek* [1976] were adapted to create low-concentration ED-XRF calibration standards by the precipitation of trace elements from solution with the chelating ligand diethyldithiocarbamate (DDTC).

Polycarbonate track-etched (PCTE) filters (37 mm diameter, 0.4 µm pore size) were used for preparation of low-concentration ED-XRF standards. Filters were cleaned by soaking in 4 N HNO_3 for 1 day, rinsing with de-ionized water, soaking in 1 N HCl for 3–7 days, and finally rinsing with de-ionized water before drying under vacuum and weighing before use. Commercially available dissolved Fe standard solutions were diluted to Fe concentrations ranging from 0.055 to 2.5 µmol L^{-1} and adjusted to a pH of 4 with sub-boiling distilled HCl. For each standard, 2 mL of a 1% solution of sodium diethyldithiocarbamate (NaDDTC) was added to a 20 mL sample of the Fe solution. After gently shaking the solution for 5 minutes, the precipitate was filtered over a pre-washed PCTE filter then dried under vacuum. Procedural blanks were prepared by adding 2 mL of the 1% NaDDTC solution to a 20 mL sample of DI water acidified to pH 4 with sub-boiling distilled HCl and filtering over an acid-cleaned filter.

The preparation of DDTC-precipitated calibration standards was optimized for DDTC ligand concentration and shaking time for maximum recovery of Fe. To examine the effect of excess ligand on trace metal recovery from solution, increasing amounts of a 1% NaDDTC solution were added to a 5.5 µmol L^{-1} Fe solution while maintaining a constant solution volume of 22 mL and pH of 4. **Figure 2.2** shows the relationship between solution DDTC:Fe ratio and XRF response; a DDTC:Fe molar ratio of 4 was chosen to optimize Fe recovery. To determine the effects of increased sample shaking time after DDTC addition, 12 replicate solutions were prepared by adding 2 mL of the 1% ligand solution to 20 mL aliquots of a 5.5 µmol L^{-1} Fe solution at pH 4. Duplicate samples were filtered after gentle shaking for time intervals of 5 min to 23 hr. The ED-XRF response versus sample shaking time is shown in **Figure 2.3**. Increased shaking time resulted in decreased Fe recovery (up to 38% after 23 hours) and a short shaking time before filtration (5 min) was chosen for preparation of calibration standards.

To confirm complete precipitation of Fe from solution and accuracy of calibration standard Fe filter concentration, filter samples were prepared according to the optimized procedure described above and subjected to a total acid digestion protocol (see section ***2.2.3***). The digest solutions were analyzed for Fe by graphite furnace atomic absorption spectrometry (GFAAS). As shown in **Figure 2.4**, Fe is quantitatively precipitated from the sample solution by coordination with DDTC and deposited on the filter for Fe concentrations up to 500 ng cm^{-2} (2.5 µmol L^{-1} Fe solution concentration).

Standard filters were also qualitatively surveyed by scanning electron microscopy (SEM) with energy dispersive X-ray microanalysis to examine structure and size of Fe-DDTC precipitates (**Fig. 2.5**). The precipitate appears evenly distributed across the filter relative to the diameter of the ED-XRF sampling beam (~12 mm). The size of individual particles (several microns) is generally on the scale of Fe-rich particles that would be expected in upper ocean SPM samples (e.g., small phytoplankton, lithogenic aerosols [*Buck et al.*, 2010], or detrital material).

2.2.4 Sample digest protocol

SPM sample filters were subjected to HNO_3/HF microwave digestion conducted under a laminar flow hood using de-ionized water, sub-boiling distilled 16 N HNO_3, and trace-element clean HF (Fisher Optima). Filters were placed in high-pressure Teflon digestion bombs with 4 mL HNO_3 and 0.25 mL HF and heated in a standard 1200-Watt microwave for 1 minute at maximum power followed by an additional 60 minutes at 10% power. After being allowed to cool overnight, the solutions were transferred to Teflon evaporation vessels and placed on a hot plate over low heat until the solutions were reduced to a droplet. Finally, samples were brought up in 10% HNO_3 and stored in acid-cleaned, low-density polyethylene vials until HR ICP-MS analysis. Sample solutions were further diluted up to 20-fold with 10% SBD HNO_3 for HR ICP-MS analysis. Procedural blanks (digestion protocol with acid reagents only) and filter blanks (digestion protocol with acid-cleaned, blank filters) were digested with each batch of 10 sample filters to monitor potential contamination during sample processing. Efficacy of the digest method was assessed by digestion and HR ICP-MS analysis of NIST SRM 2783 (air particulate on filter media).

2.2.5 HR ICP-MS method

An HR-ICPMS method was developed at the Marine Analytical Laboratory University of California, Santa Cruz to analyze 10 elements of interest for comparison with ED-XRF data and Rh, Bi, and Ga were monitored for instrumental drift (**Table 2.3**). Although Si concentrations in SPM samples

are also routinely analyzed by ED-XRF, Si was not analyzed by HR ICP-MS as Si is unstable when trace amounts of HF are present from the digestion procedure.

The sample digest solutions were analyzed on a Thermo Element XR HR ICP-MS (magnetic sector). The samples were pumped into an ESI-PC3 Peltier cooling spray chamber at 4°C by a peristaltic pump at a rate of 120 µl min^{-1}. The HR ICP-MS was tuned prior to each instrument session by adjusting the torch position, the sample gas (Ar) flow rate (~0.75 L min^{-1}), and an additional Ar gas inlet flow rate (~0.19 L min^{-1}). Elements were analyzed in the optimal resolution for minimizing interferences (**Table 2.3**). Each mode consisted of 3 runs and 5 scans with the detector set to triple mode (able to transition between counting, analog, and Faraday). Each scan in low resolution mode required 1.271 seconds, scans in medium resolution mode required 4.310 seconds, and scans in high resolution mode required 2.362 seconds. The total analysis time per sample, including washout, was approximately 3.5 minutes, consuming a sample volume of approximately 0.36 mL. Analytical accuracy of the HR ICP-MS method was assessed by analysis of NIST certified reference material 1640a (trace elements in natural water).

Data was processed offline. First, the internal standards (Rh, Bi, Ga) were used to correct for variance in detector sensitivity between samples. Next, instrumental drift over the course of the run was corrected using the change in slope of the standard curve for each element. Lastly, samples were corrected for a combined instrumental and procedural blank determined from analysis of acid-cleaned blank filters digested according to the procedure described above (n = 5). Minimum detection limits for the HR ICP-MS method are reported as three times the standard deviation of the instrumental blank, which was determined by analysis of 1.5 M (10%) quartz-distilled HNO_3 between sample runs.

2.2.6 Statistical comparison of paired data

Trace element concentrations determined from ED-XRF and HR ICP-MS analyses are compared by a line fit calculated using the functional relationship estimation by maximum likelihood (FREML) method [*Ripley and Thompson*, 1987] on paired data points for all samples that exceed the minimum detection limit of both methods. This statistical method was chosen to account for the differences in precision between the two methods. The functional relationship estimation is solved by an iterative numerical method and provides standard errors for lack of fit statistics.

2.3 Results and Discussion

2.3.1 ED-XRF accuracy, detection limits, and blanks

Minimum determination limits for the ED-XRF method calculated using equation 2.1 and MicroMatter standards are shown in **Table 2.4** along with filter blank values for individual elements. For most elements, filter blank values are below the detection limit of the ED-XRF method. Filter blanks for Al, Fe, and Cu are somewhat higher than the lowest blanks that have previously been reported for polycarbonate filters, although they are generally comparable or lower than reported blanks for other filter types used for SPM sample collection (e.g., Whatman QMA quartz fiber filter, MF-Millipore cellulose filter, Supor polysulfone filter) [*Planquette and Sherrell*, 2012].

Because a certified reference material for marine suspended particulate matter is not currently available, NIST certified reference material 2783 (air particulate on filter media) was used to determine analytical accuracy of the ED-XRF method. Recoveries for individual elements for NIST 2783 by ED-XRF are shown in **Table 2.5.** Average ED-XRF values for SRM 2783 are generally within +/- 10% of the reported certified value. Recovery of Zn falls slightly outside of this range at 85%. However, this measured value is consistent with previous studies that report measured values of approximately 80% of certified values for Zn [*Saitoh and Sera*, 2005], indicating that the NIST value may be suspect.

2.3.2 HR ICP-MS accuracy, detection limits, and blanks

Detection limits for the ICPMS method calculated from the instrumental blank are shown in **Table 2.6** along with filter blank values for individual elements. Instrumental blank values for Al, Cu, Zn, and Pb were below the detection limit of the HR ICP-MS method. Instrumental blanks for other elements were 0.1–4.0% of average measured sample concentrations. Filter blanks were $\leq$5% of average sample values for Al, P, Ca, Mn, Al, and Pb. For Ni, Cu, and Zn, filter blank values were slightly higher at 8–19% of average measured sample concentrations. Precision of the HR ICP-MS analysis was typically 2%, ranging from 0.7% to 3.6% for individual elements.

NIST certified reference material 1640a (trace elements in natural water) was used to determine analytical accuracy of the HR ICP-MS method. Recoveries for individual elements for NIST 1640a from HR ICP-MS analysis are shown in **Table 2.7.** Measured values are generally within +/- 10% of the reported certified value. However, both Ca and Pb fall outside of this range with 57% and 81% recoveries, respectively.

Efficacy of the digest method was assessed by digestion and HR ICP-MS analysis of NIST SRM 2783 (air particulate on filter media); recoveries for individual elements are shown in **Table 2.8**.

Recoveries of Al, Fe, and Mn were within ± 10% of certified values. Recoveries of V, Ni, Cu, Zn, and Pb were more variable, within ± 25% of certified values. Good recovery (± 10%) of more refractory elements associated with lithogenic material (i.e, Al, Fe) suggest that the protocol achieved near-complete digestion of SPM samples. Results were generally comparable to previous results from HF-assisted microwave acid digestion of standard reference materials as shown in **Table 2.8** [*Morton et al.*, 2013]. Recovery of Ca was unexpectedly low (55%), although HR ICP-MS analysis of NIST 1640a (measured value for Ca is 57% of certified value) indicates this may be due to methodological problems with detection of Ca by HR ICP-MS. Similarly, the apparent low recovery of Pb from the digest procedure (77%) may be due in large part to systematic underestimation of Pb concentrations by the HR ICP-MS method (measured value for NIST 1640a is 81% of certified value).

2.3.3 Comparison of ED-XRF and HR ICP-MS paired data

Results from ED-XRF and HR ICP-MS analyses of SPM samples were compared by a line fit calculated using the FREML method on paired data points for all samples that exceeded the minimum determination limit for both methods. The slope and error for the FREML fit for individual elements is shown in **Table 2.9**, with slopes reported as HR ICP-MS versus ED-XRF measurements. Several samples had Mn, Ni, or Zn concentrations that were below the minimum detection limit of the ED-XRF method and were omitted from FREML analyses. For comparison of P, Mn, and Fe measured values, one or both SPM filters from cruise KM1008 sampled near vent environments were excluded from FREML analysis; concentrations of P, Mn, or Fe in these samples were 1–3 orders of magnitude higher than all other samples (see **Table 2.9**). Comparison of V and Pb was restricted by the detection limit of the ED-XRF method for these elements; in only 2–4 samples were concentrations above the ED-XRF detection limit and FREML analyses were not performed on these datasets. Comparison plots of ED-XRF versus HR ICP-MS measurements for Al, P, Ca, V, Mn, Fe, Ni, Cu, Zn, and Pb are shown in **Figure 2.6**.

There was generally good agreement between the two analytical methods for Al, Mn, and Fe. Vertical profiles for particulate Fe and Al from the top 1000 m along the CLIVAR P2 section at station 14 (30°N, 135°N) analyzed by ED-XRF and HR ICP-MS analysis are shown in **Fig. 2.7**. Comparison of V and Pb data suggest reasonable agreement between the two methods, but more ED-XRF data is needed for a rigorous statistical comparison. Relatively good agreement was also seen for Ni measurements, although relative errors in the statistical comparison of Ni concentrations are large (~40%) due to precision limits of the ED-XRF method and the low concentrations of samples analyzed. In samples with the lowest Cu concentrations, values measured by ED-XRF are slightly higher than those measured by HR ICP-MS. For P

and Zn, HR ICP-MS measurements are significantly higher than values obtained by ED-XRF. This could be due to potential contamination during the digest procedure, although systematic contamination issues of comparable magnitude were not apparent from analysis of blank filters or reference material NIST SRM2783. The HR ICP-MS analysis appears to underestimate Ca concentrations compared to ED-XRF, although this is the result of a known methodological problem, as discussed above in section 2.3.2. Additional samples have been analyzed by Dr. Peter Morton at Florida State University and initial results also show good agreement between ED-XRF and HR ICP-MS methods (**Appendix, Fig. A.1**).

2.4 Conclusions

Data presented here show that ED-XRF and HR ICP-MS methods produce comparable data for many trace elements of oceanographic interest when analyzing samples at the sub-nanomolar concentrations typical of much of the remote open ocean. ED-XRF analysis may be advantageous for some elements predominantly found in refractory lithogenic material (i.e, Al, Fe) to avoid the hazardous HF-assisted digestion necessary for analysis by ICP-MS. Likewise, the minimal sample processing required by ED-XRF analyses minimizes sample blanks and uncertainties from contamination risks for easily-contaminated elements that tend to have relatively high digest filter blank values (e.g., Zn). Currently, ED-XRF methods are limited by detection limits for trace elements found in extremely low levels in the particulate phase due to a combination of low overall concentrations in the marine environment and high solubility in seawater (e.g., Pb).

2.5 Appendix

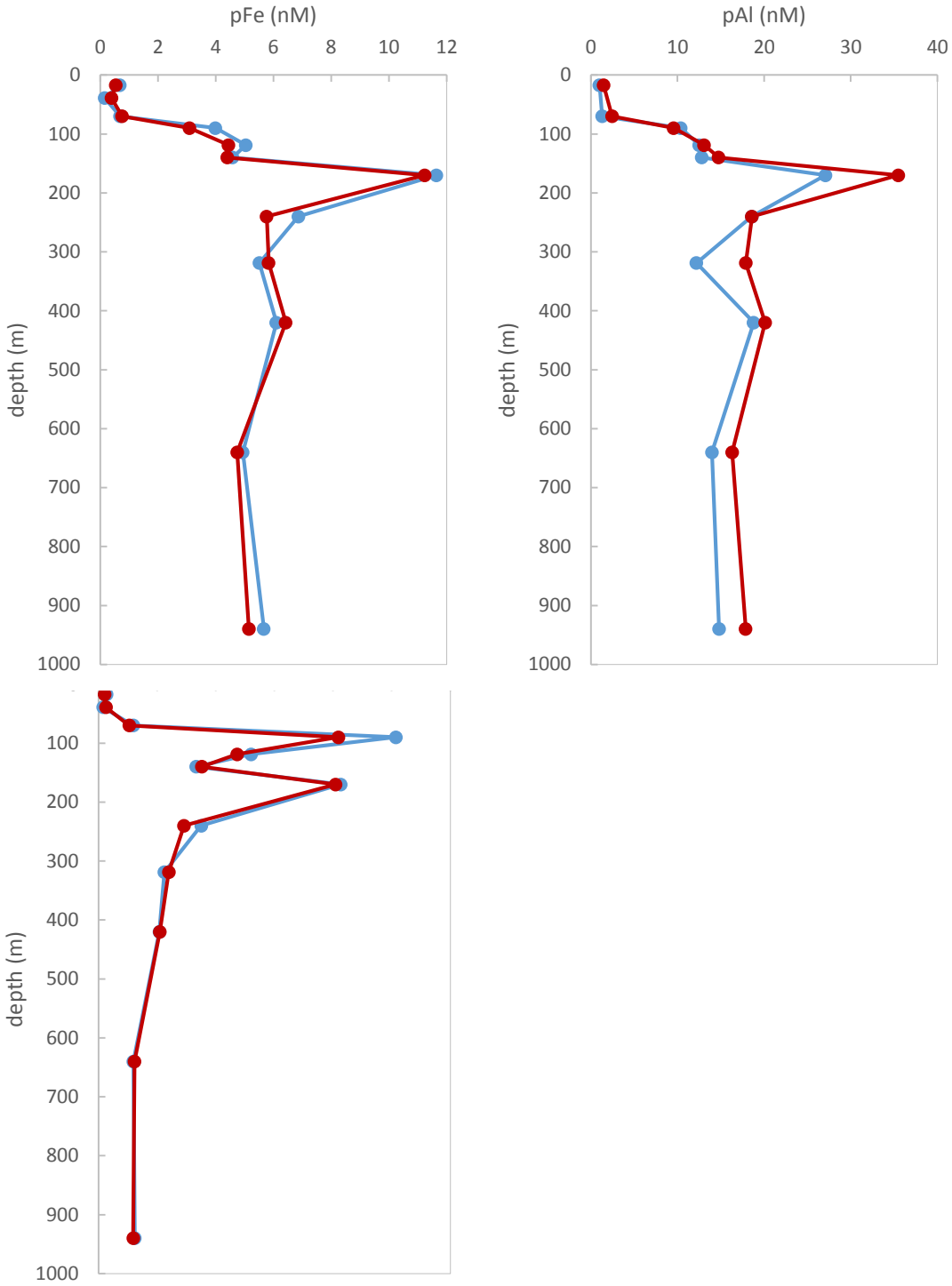

Figure A.1. Vertical profiles of particulate Fe, Al, and Mn in the top 1000 m at station 199 (18°N, 90°E) on the CLIVAR I9N transect in the Indian ocean measured by ED-XRF (blue) and HR ICP-MS (red) [*P. Morton, personal communication*].

2.6 References

Bowie, A.R., Townsend, A.T., Lannuzel, D., Remenyi, T. A, van der Merwe, P., 2010. Modern sampling and analytical methods for the determination of trace elements in marine particulate material using magnetic sector inductively coupled plasma-mass spectrometry. Anal. Chim. Acta 676, 15-27.

Buck, C.S., Landing, W.M., Resing, J.A., Measures, C.I., 2010. Particle size and aerosol iron solubility: a high-resolution analysis of Atlantic aerosols. Mar. Chem. 120, 14–24.

Cook, J.M., Gardner, M.J., Griffiths, A.H., Jesseps, M.A., Ravenscroft, J.E., Yates, R., 1997. The comparability of sample digestion techniques for the determination of metals in sediments. Mar. Pollut. Bull. 34, 637-644.

Cullen, J.T., Field, M.P., Sherrell, R.M., 2001. Determination of trace elements in filtered suspended marine particulate material by sector field HR ICP-MS. J. Anal. At. Spectrom. 16, 1307-1312.

Feely, R.A., Massoth, G.J., Lebon, G.T., 1991. Sampling of marine particulate matter and analysis by x-ray fluorescence spectrometry. In: Hurd, D.C. and Spencer, D.W. (eds.), Marine Particles: Analysis and Characterization, AGU Geophysical Monograph Series, p. 251-257.

Holynska, B., Bisiniek, K., 1976. Determination of trace amounts of metals in saline water by energy dispersive XRF using the NaDDTC preconcentration. J. Radioanal. Nucl. Chem. 31, 159–166.

Korotev, R.L., 1987. Chemical homogeneity of National Bureau of Standards coal flyash (SRM 1633a). J. Radioanal. Nucl. Chem. 110, 179-189.

Krachler, M., 2007. Environmental applications of single collector high resolution ICP-MS. J. Environ. Monit. 9, 790-804.

Lam, P.J., Twining, B.S., Jeandel, C., Roychoudhury, A., Resing, J.A., Santschi, P.H., Anderson, R.F., 2015. Methods for analyzing the concentration and speciation of major and trace elements in marine particles. Prog. Oceanogr. doi:10.1016/j.pocean.2015.01.005.

Measures, C.I., Landing, W.M., Brown, M.T., Buck, C.S., 2008. A commercially available rosette system for trace metal-clean sampling. Limnol. Oceanogr. Methods 6, 384-394.

Morton, P.L., Landing, W.M., Hsu, S.-C., Milne, A., Aguilar-Islas, A.M., Baker, A.R., Bowie, A.R., Buck, C.S., Gao, Y., Gichucki, S., Hastings, M.G., Hatta, M., Johansen, A.M., Losno, R., Mead, C., Patey, M.D., Swarr, G., Vandermark, A., Zamora, L.M., 2013. Methods for the sampling and analysis of marine aerosols: results from the 2008 GEOTRACES aerosol intercalibration experiment. Limnol. Oceanogr. Methods 11, 62–78.

Planquette, H., Sherrell, R.M., 2012. Sampling for particulate trace element determination using water sampling bottles: methodology and comparison to in situ pumps. Limnol. Oceanogr. Methods 10, 367-388.

Ripley, B. D., and M. Thompson, 1987, Regression techniques for analytical bias, Analyst, 112, 377-383.

Saitoh, K., Sera, K., 2005. Examination of quantitative accuracy of PIXE analysis for atmospheric aerosol particle samples: PIXE analysis of NIST air particulate on filter media. Int. J.PIXE 15, 59-63.

Schlitzer, R., 2010. Ocean Data View. http://odv.awi.de.

Table 2.1. Marine suspended particulate matter samples analyzed in comparison study.

sample #	cruise	station location	depth (m)
1	CLIVAR A16N (2003)	48°N, 20°W	30
2	CLIVAR A16N (2003)	48°N, 20°W	110
3	CLIVAR A16N (2003)	48°N, 20°W	550
4	CLIVAR A16N (2003)	48°N, 20°W	750
5	CLIVAR A16N (2003)	15°N, 29°W	20
6	CLIVAR A16N (2003)	15°N, 29°W	325
7	CLIVAR A16N (2003)	15°N, 29°W	950
8	CLIVAR P2 (2004)	30°N, 134°E	50
9	CLIVAR P2 (2004)	30°N, 134°E	70
10	CLIVAR P2 (2004)	30°N, 134°E	440
11	CLIVAR P2 (2004)	30°N, 134°E	900
12	CLIVAR P2 (2004)	30°N, 138°W	270
13	KM1008 (2010)	15°S, 174°W	1146
14	KM1008 (2010)	15°S, 174°W	1954

Table 2.2. ED-XRF excitation conditions for trace elements of interest.

condition	filter	voltage (kV)	current (mA)	analytes
low Za	graphite thin	10	1.98	Al, P
low Zb	graphite thick	12	1.98	Ca
mid Za	Pd thin	30	1.66	V, Mn, Fe, Ni, Cu, Zn
mid Zb	Pd thick	50	1.0	Pb

Table 2.3. HR ICP-MS analytical conditions for trace elements of interest.

mode	analyte	runs	number of scans	scan length (s)
low	**^{103}Rh,** ^{208}Pb, **^{209}Bi**	3	5	1.271
medium	^{27}Al, ^{31}P, ^{43}Ca, ^{51}V, ^{55}Mn, ^{56}Fe, ^{60}Ni, ^{63}Cu, ^{66}Zn, **^{69}Ga, ^{103}Rh**	3	5	4.310

note: analytes in bold denote elements monitored for interferences or as internal standards

Table 2.4. Minimum determination limits (MDL) and average filter blank values for ED-XRF analysis reported as both filter concentration (ng cm^{-2}) and equivalent seawater concentration (nmol L^{-1}) for the average sample filtration volume (8 L).

analyte	MDL		filter blank (n=11)	
	(ng cm^{-2})	(nmol L^{-1})	(ng cm^{-2})	(nmol L^{-1})
Al	9.4	0.54	11.04	0.63
P	2.01	0.10	BDL	---
Ca	3.99	0.15	7.22	0.28
V	2.41	0.07	BDL	---
Mn	1.27	0.04	BDL	---
Fe	0.95	0.03	2.11	0.06
Ni	0.77	0.02	BDL	---
Cu	1.25	0.03	1.31	0.03
Zn	1.28	0.03	BDL	---
Pb	1.58	0.01	BDL	---

BDL = below instrumental detection limit

Table 2.5. Results from monthly ED-XRF analysis of reference material NIST SRM 2783 (air particulate on filter media) compared to certified values for individual elements (in ng cm^{-2}).

analyte	certified value (ng cm^{-2})	+/- 1 SD	measured value (ng cm^{-2})	+/- 1 SD	recovery (%)
Al	2330.32	53	2149.65	82.27	92
P	n/a	---	---	---	---
Ca	1325.3	170	1338.7	64.0	101
V	4.86	0.6	BDL	---	---
Mn	32.13	0.12	33.51	0.81	104
Fe	2660	160	2864	69.2	108
Ni	6.82	1.2	6.41	0.45	94
Cu	40.5	0.42	43.67	2	108
Zn	179.72	13	153.36	4.19	85
Pb	31.8	5.4	32.9	3.4	103

n/a = certified or reference value not available
BDL = below instrumental detection limit

Table 2.6. Minimum determination limits (MDL), average instrument blank values, and average filter blank values for HR ICP-MS analysis reported as both sample concentrations (ppb) and equivalent seawater concentration (pmol L^{-1}) for the average sample filtration volume (8 L).

	MDL		instrument blank (n=6)		filter blank (n=5)	
analyte	(ppb)	(pmol L^{-1})	(ppb)	(pmol L^{-1})	(ppb)	(pmol L^{-1})
Al	3.0	56.5	BDL	---	8.5	158
P	0.40	6.5	0.85	13.8	3.9	63.7
Ca	0.73	9.1	1.8	22.9	31.0	387
V	0.001	0.01	0.01	0.06	0.05	0.46
Mn	0.01	0.05	0.01	0.06	0.13	1.2
Fe	0.58	5.2	2.7	24.2	11.4	102
Ni	0.05	0.39	0.05	0.43	0.55	4.7
Cu	0.03	0.25	BDL	---	0.51	4.0
Zn	0.23	1.8	BDL	---	2.4	18.5
Pb	0.02	0.04	BDL	---	0.07	0.18

BDL = below instrumental detection limit

Table 2.7. Analysis of certified reference material NIST 1640a (trace elements in natural water) by HR ICP-MS compared to certified values for individual elements (in ppb).

analyte	certified value (ppb)	+/- 1 SD	measured value (ppb)	+/- 1 SD	recovery (%)
Al	52.6	1.8	57.2	4.1	109
P	n/a	---	---	---	---
Ca	5570[a]	16	3458	44	57
V	14.93	0.21	14.40	0.20	96
Mn	40.07	0.35	39.76	0.54	99
Fe	36.5	1.7	37.0	5.6	101
Ni	25.12	0.12	25.41	0.50	101
Cu	85.07	0.48	91.78	1.78	108
Zn	55.2	0.32	58.2	2.7	105
Pb	12.10	0.05	9.77	0.28	81

n/a = certified or reference value not available

[a]reference value only

Table 2.8. Results from acid digestion and HR ICP-MS analysis of reference material NIST SRM 2783 (air particulate on filter media) reported in ng cm^{-2} compared to certified values for individual elements.

analyte	certified value (ng cm^{-2})	SD	measured value (n=2)	SD	% recovery	*Morton et al.* [2013][a]
Al	2330.32	53	2126	40	91	62–107%
P	n/a	---	---	---	---	---
Ca	1325.3	170	725	15	55	---
V	4.86	0.60	4.22	0.04	87	---
Mn	32.13	0.12	29.4	0.6	91	---
Fe	2660	160	2463	38	93	73–100%
Ni	6.82	1.2	8.5	1.1	125	---
Cu	40.5	0.42	48.8	2.1	121	---
Zn	179.72	13	143.2	3.3	80	78–105%
Pb	31.8	5.4	24.5	0.9	77	87–109%

[a]recovery of selected elements from standard reference materials as analyzed by ICP-MS after HF-assisted microwave digestion.
n/a = certified or reference value not available

Table 2.9. Slope of ED-XRF versus HR ICP-MS relationship for paired data points determined by functional relationship estimation by maximum likelihood (FREML) method.

Analyte	slope	+/- 1 SD	notes
Al	1.30	0.03	
P	1.31	0.01	*sample 13 omitted from analysis*
Ca	0.69	0.01	
V	n/a	---	
Mn	1.16	0.06	*3 samples below ED-XRF detection limit; sample 14 omitted from analysis*
Fe	1.16	0.01	*samples 13 and 14 omitted from analysis*
Ni	3.30	1.30	*1 sample below ED-XRF detection limit*
Cu	1.45	0.07	
Zn	2.72	0.14	*3 samples below ED-XRF detection limit*
Pb	n/a	---	

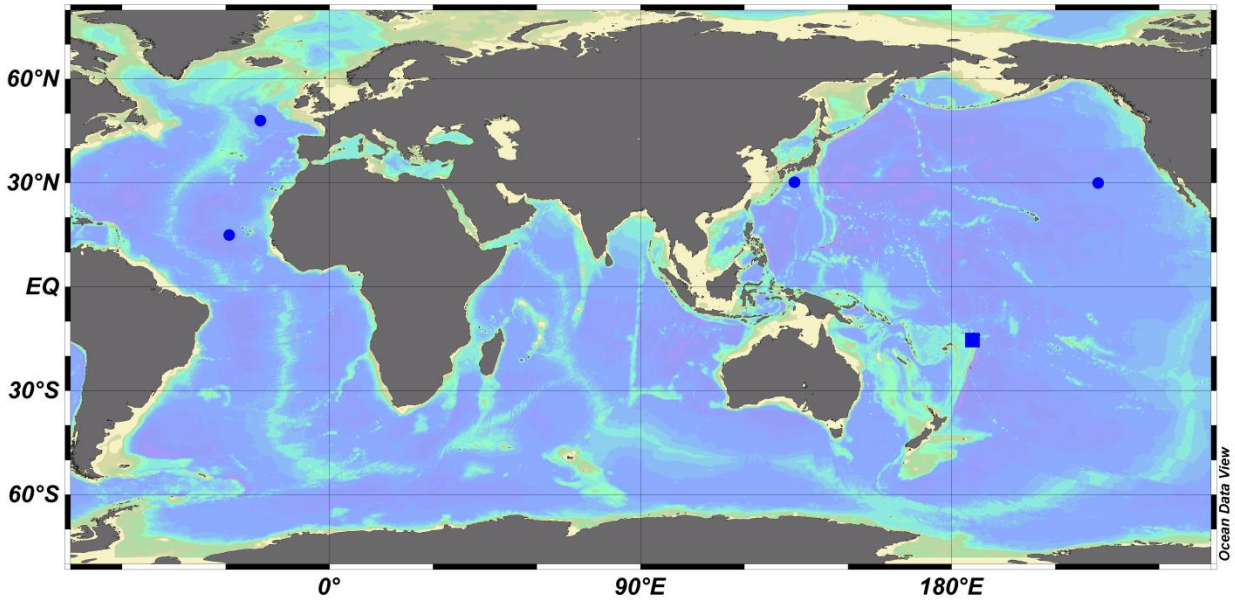

Figure 2.1. Locations of marine particulate matter samples used in this study. Samples collected in the top 1000 m at open-ocean stations along CLIVAR sections A16N (2003) and P2 (2004) are indicated by circles. The square symbol contains the locations of hydrothermal vent field samples at NE Lau basin sites at depths of 1100–2000 m collected during KM1008 (2010). Plotted using Ocean Data View [*Schlitzer*, 2010].

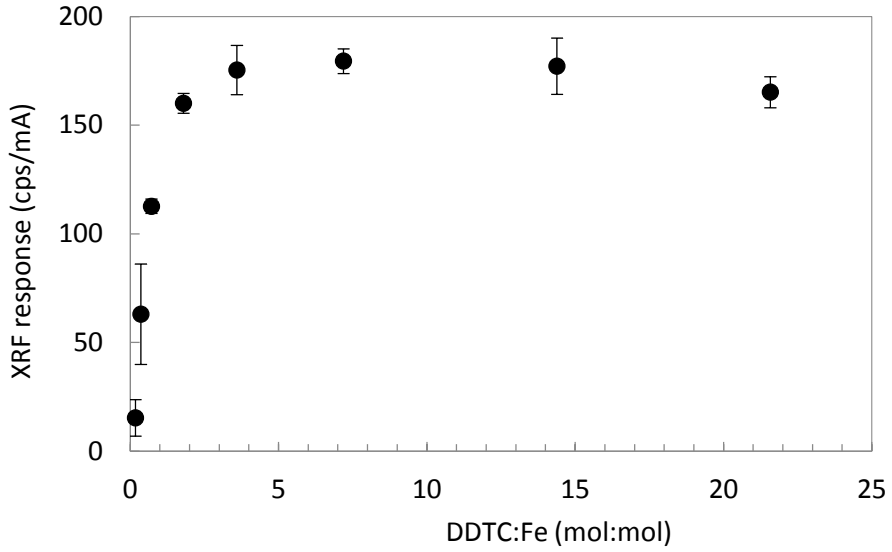

Figure 2.2. Effect of increased DDTC:Fe ratio on XRF count intensity. Error bars represent the standard deviation of duplicate samples; where no error bar is shown, the error is contained within the symbol.

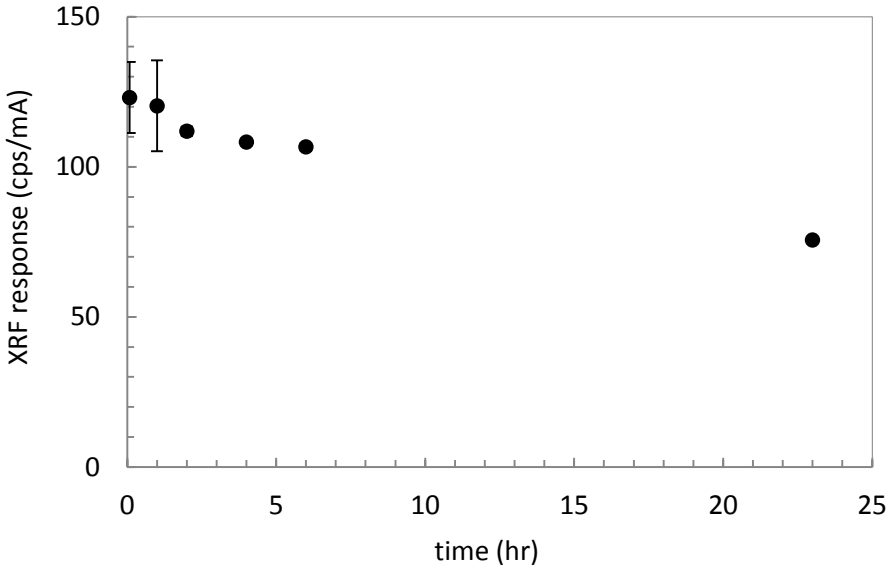

Figure 2.3. Effect of increased shaking time on XRF count intensity. Error bars represent the standard deviation of duplicate samples; where no error bar is shown, the error is contained within the symbol.

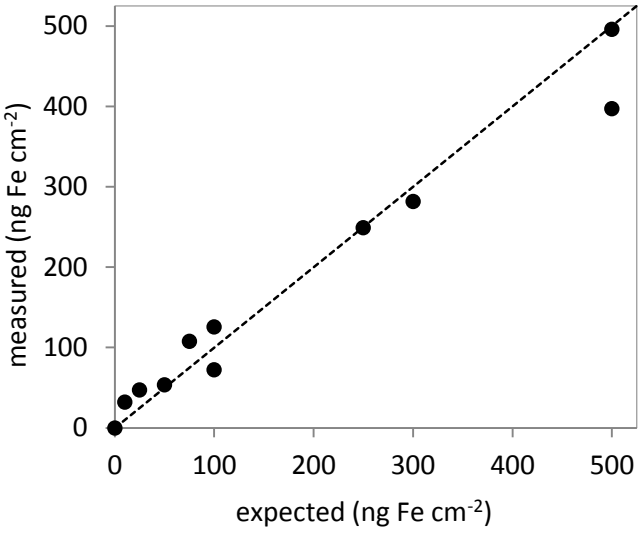

Figure 2.4. Fe concentrations of DDTC ED-XRF calibration filters digested and analyzed by GFAAS plotted against expected filter Fe concentrations (in ng Fe cm^{-2}). Dashed line indicates 1:1 line.

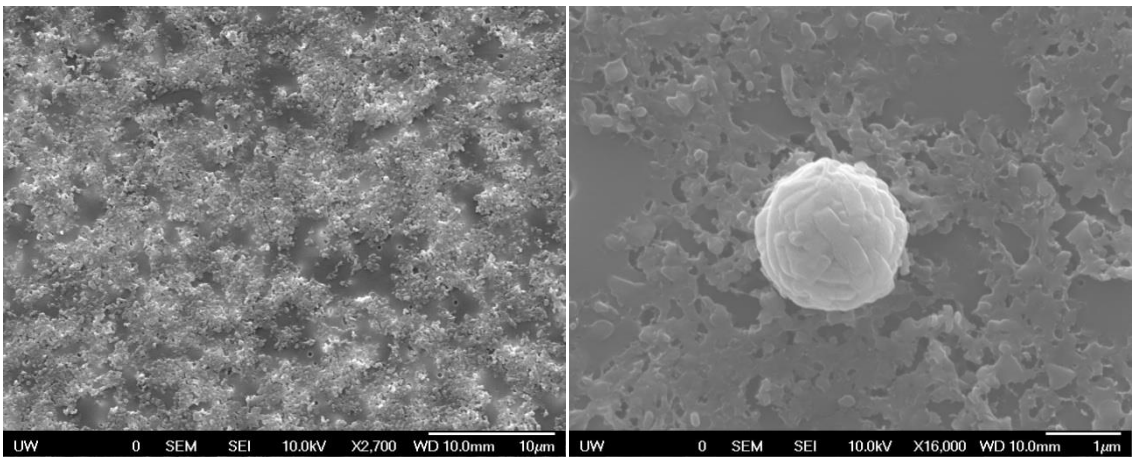

Figure 2.5. Scanning electron microscope images of Fe-rich particles on ED-XRF calibration filters prepared by DDTC procedure shown with 10 µm (left) and 1 µm (right) scale bars.

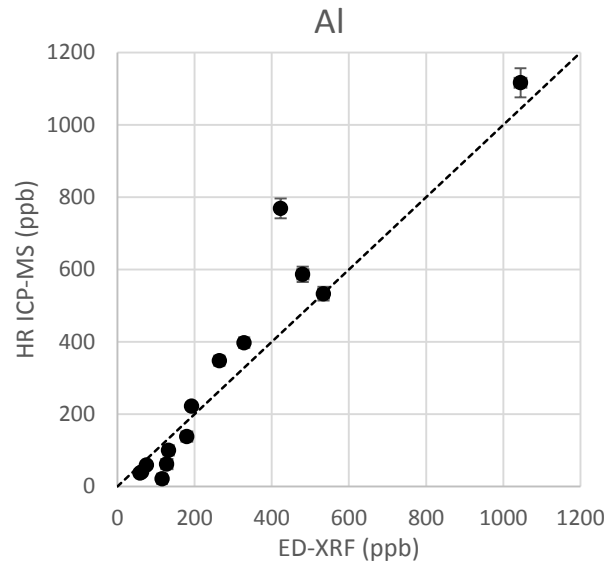
Al
HR ICP-MS (ppb)
ED-XRF (ppb)
0
200
400
600
800
1000
1200

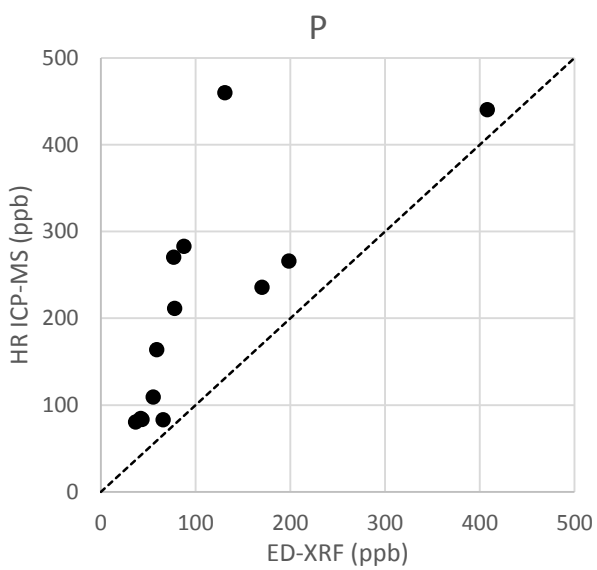
P
HR ICP-MS (ppb)
ED-XRF (ppb)
0
100
200
300
400
500

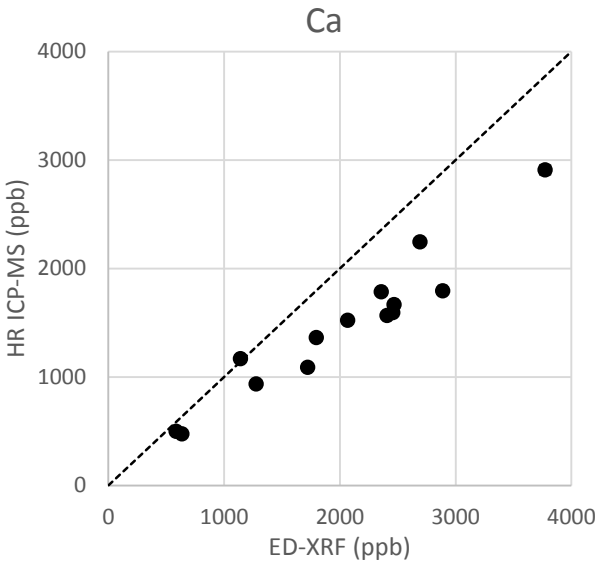
Ca
HR ICP-MS (ppb)
ED-XRF (ppb)
0
1000
2000
3000
4000

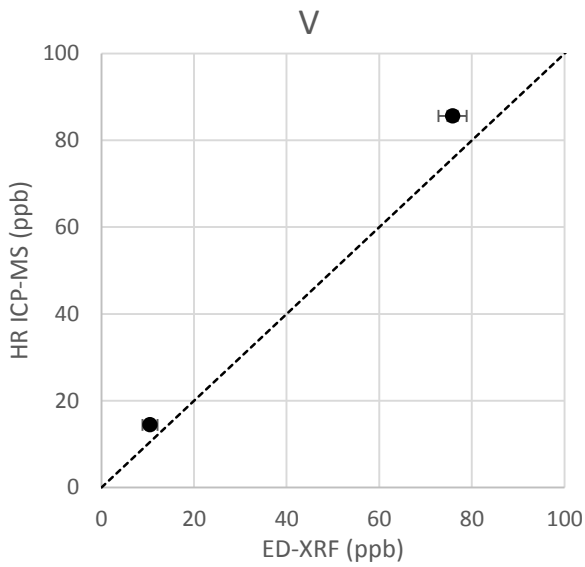
V
HR ICP-MS (ppb)
ED-XRF (ppb)
0
20
40
60
80
100

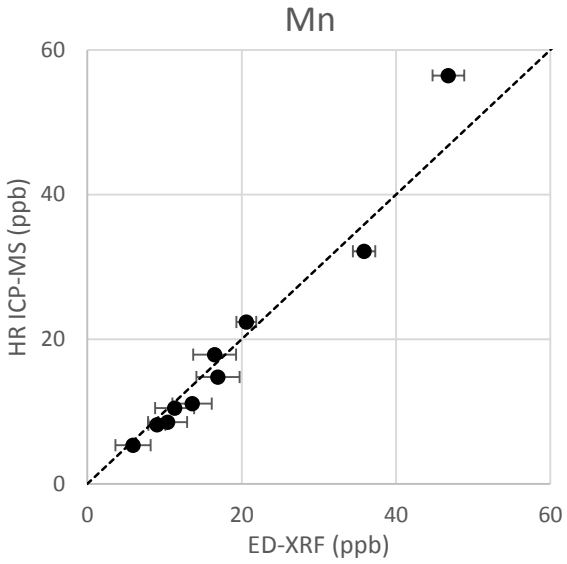
Mn
HR ICP-MS (ppb)
ED-XRF (ppb)
0
20
40
60

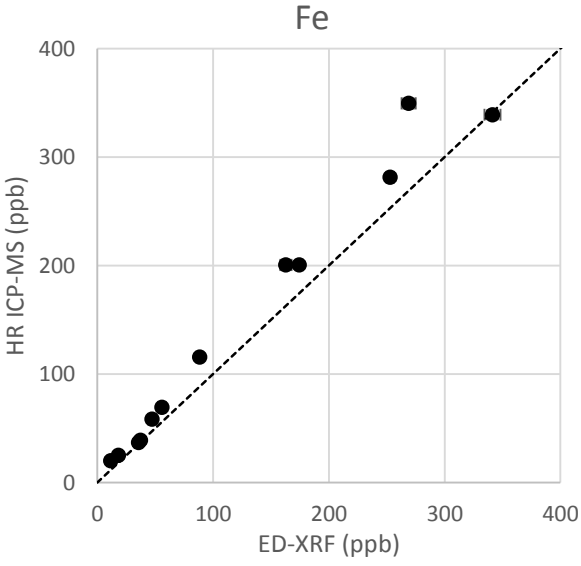
Fe
HR ICP-MS (ppb)
ED-XRF (ppb)
0
100
200
300
400

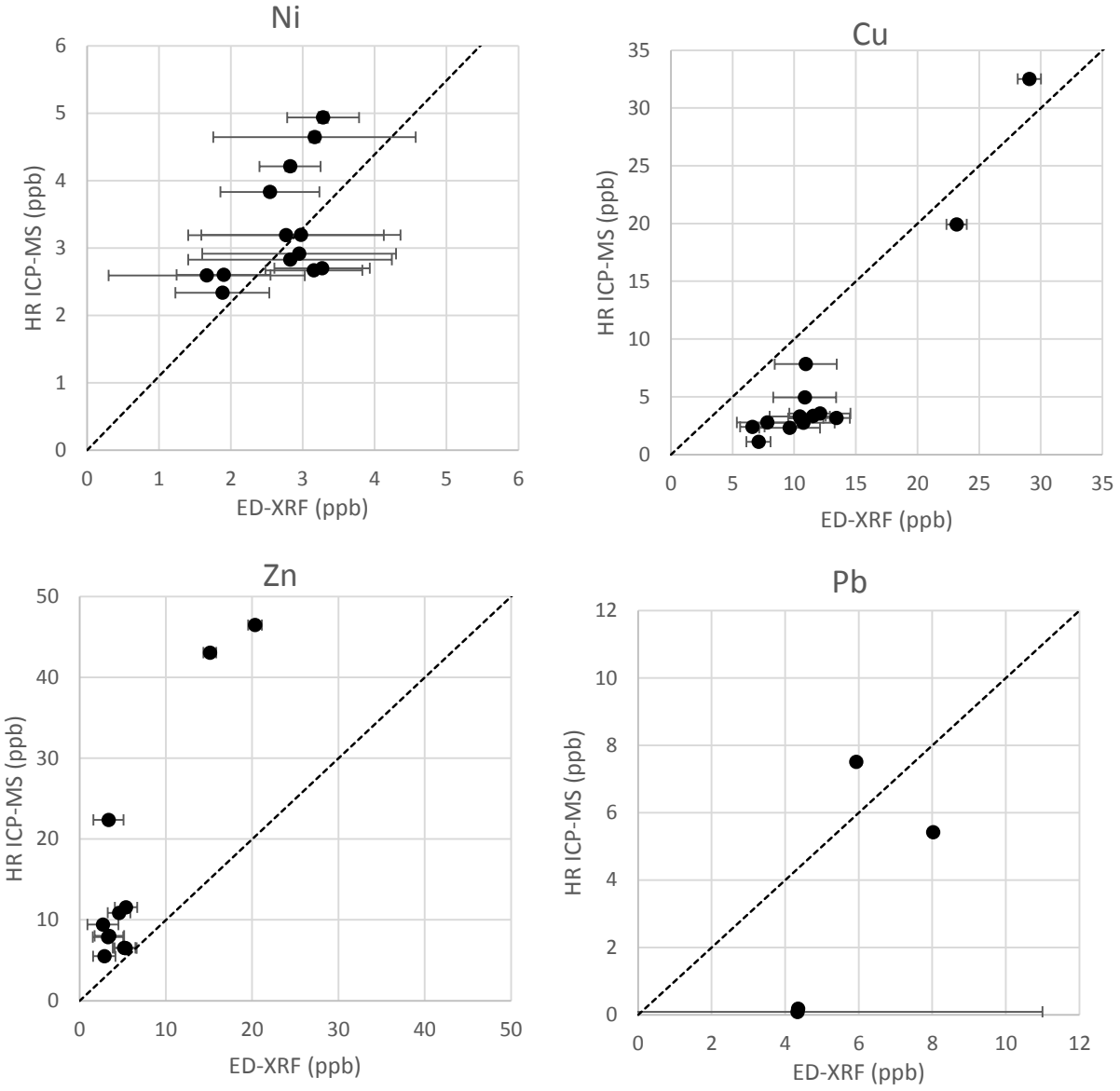

Figure 2.6. HR ICP-MS values plotted against ED-XRF measurements (in ppb) of Al, P, Ca, V, Mn, Fe, Ni, Cu, Zn, and Pb in SPM samples shown with a 1:1 line. Vertical and horizontal error bars indicate +/- 1 standard deviation in HR ICP-MS and ED-XRF measurements, respectively; where no error bars are shown, the error is contained within the symbol.

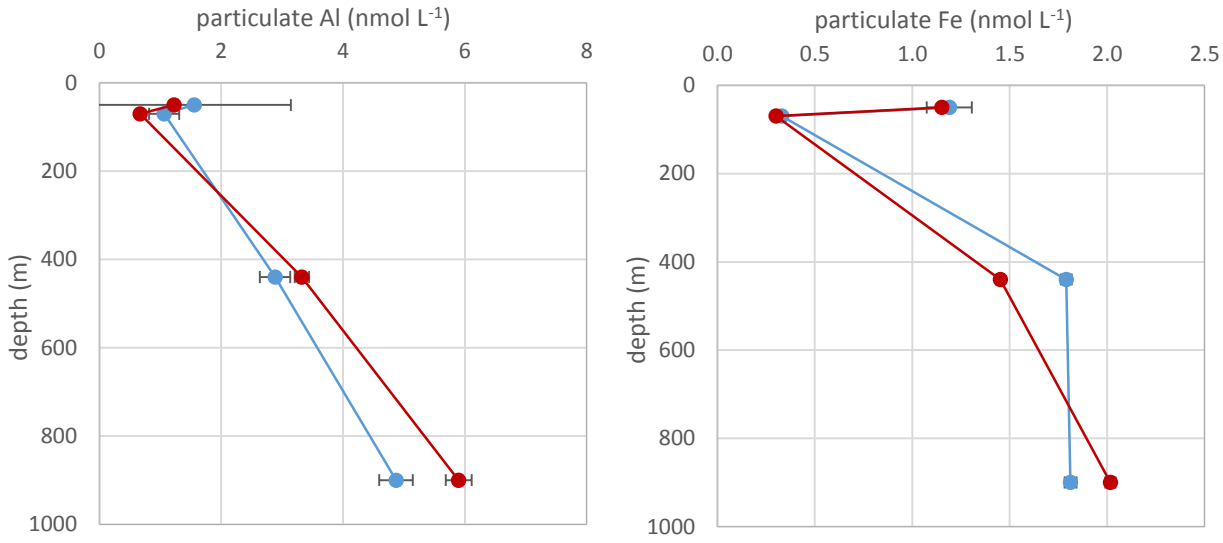

Figure 2.7. Vertical profiles of particulate Al and particulate Fe in the top 1000 m at station 14 on the CLIVAR P2 transect (30°N, 135°E) measured by ED-XRF (blue) and HR ICP-MS (red). Error bars represent +/- 1 standard deviation; where no error bars are shown, the error is contained within the symbol.

Chapter 3: Changes in the distribution of Al and particulate Fe along A16N in the eastern North Atlantic Ocean between 2003 and 2013: Implications for changes in dust deposition

3.1 Introduction

Constraining the supply of iron (Fe) to the ocean euphotic zone is of critical importance due to the role of Fe as an essential trace nutrient for ocean primary productivity. Changes in the supply of Fe to the surface ocean modify ocean uptake of CO_2, impacting global climate through modulation of atmospheric CO_2 levels. Inputs of new Fe can be supplied to the ocean by advection from continental margin sediments, riverine inputs, and hydrothermal fluxes [*Boyd and Ellwood*, 2010 and references therein], although in many remote ocean regions, the primary input of new Fe to the euphotic zone is deposition of atmospheric aerosols [*Duce and Tindale*, 1991; *Jickells et al*., 2005; *Krishnamurthy et al*., 2010]. This exchange between the atmosphere and the ocean must be better constrained in order to accurately model the biogeochemical cycling of biologically-important trace metals in the ocean and its feedbacks on global climate.

Estimates of dust deposition and associated Fe flux to the open oceans made from measurements of dust flux at coastal and island-based sampling sites have greatly informed our knowledge of ocean dust deposition rates and have constrained atmospheric sources of trace metals to the upper ocean [*Duce and Tindale*, 1991; *Duce et al*., 1991]. However, direct measurement of dust flux on spatial and temporal scales necessary to fully characterize aerosol dust inputs to the open ocean and their sensitivity to changing global climate is logistically infeasible. To address this challenge, upper-ocean distributions of various trace metal species have been employed as chemical tracers of integrated atmospheric dust deposition on the ocean over timescales of weeks to years, including dissolved Al [*Measures and Brown* 1996; *Measures and Vink*, 2000], dissolved Ti [*Dammshäuser et al.*, 2011], and particulate Al, Fe, and Ti [*Bory and Newton*, 2000; *Barrett et al*., 2012; *Dammshäuser et al*., 2013].

In the North Atlantic, mineral dust aerosols are the dominant source of Fe to the euphotic zone in open-ocean regions, supplied by atmospheric deposition of dust from the Saharan and Sahel deserts transported across the Atlantic basin by prevailing easterly winds [*Jickells et al*., 2005; *Ussher et al*., 2013; *Conway and John*, 2014]. In 2003, a coupled ocean-atmosphere trace-metal sampling program was carried out as part of the CLIVAR/CO_2 Repeat Hydrography Program occupation of section A16N in the eastern North Atlantic [*Measures et al*., 2008a; *Buck et al*., 2010a,b; *Barrett et al.*, 2012, 2014]. Sampling along A16N was repeated in 2013, which to our knowledge represents the completion of the first repeat high-resolution, basin-scale trace metal section, providing the opportunity to examine how

ocean trace metal inventories have responded to both short-term variability and decadal-scale trends in dust deposition. Here, we compare the measured concentrations of dissolved Al and particulate Al and Fe along A16N in 2003 and 2013 to determine how features in oceanic trace-metal distributions have changed between the two occupations of the section; because of the distinct biogeochemical cycling of dissolved Fe in the upper ocean, discussion of dissolved Fe concentrations are beyond the scope of this paper and will be the subject of a separate, future manuscript. We examine changes in aerosol dust loading over the North Atlantic reported from satellite observations and model output to determine how changes in ocean trace metal inventories are related to trends in the atmospheric dust cycle and to better understand the relative importance of dust generation, atmospheric transport patterns, and deposition processes in controlling the delivery of trace metals to the North Atlantic. Repeat observations of upper-ocean trace metal distributions have important implications for the use of dust transport models to predict future trends in Fe deposition on the oceans and for validation of model representations of dust transport and deposition processes under changing dust conditions.

3.2 Methods

3.2.1 Sample collection

The trace metal data used in this analysis were collected during two sampling efforts along CLIVAR/CO_2 Repeat Hydrography section A16N from Reykjavik, Iceland to Natal, Brazil (**Fig. 3.1**) that took place from 20 June to August 7 2003 and from 3 August to 3 October 2013. Trace metal sampling was done at 60 and 63 stations in 2003 and 2013, respectively, with typical spacing of ~60 nm, or ~1 degree of latitude between stations (**Fig. 3.2**). Seawater was collected from the surface to depths of approximately 1000 m using 12 L GO-FLO bottles on a trace metal-clean rosette. GO-FLO bottles were sub-sampled in a clean laboratory van equipped with a HEPA filtered air system (see *Measures et al*. [2008b] for details). Sub-sampling protocols and dissolved and particulate trace metal analyses have been described previously for the 2003 dataset [*Measures et al*., 2008a; *Barrett et al*., 2012] and were repeated in 2013. Briefly, subsamples for dissolved trace metal analysis were collected by pressure-filtering seawater (<55 kPa filtered, compressed air) through acid-washed, 0.4 µm polycarbonate track-etched filters in polypropylene filter holders. Suspended particulate-matter samples collected on the filters were rinsed with deionized water (adjusted to pH 8 with ammonium hydroxide) while on the filter holder with a low vacuum applied. Mixed cellulose ester backing filters were used to ensure even sample loading. Filtration was started ~30 to 60 minutes after sample collection and was generally completed within 1 hour. The average sample filtration volume was 8.0 $\pm$ 2.2 and 8.9 $\pm$ 2.1 L in 2003 and

2013, respectively. Although the sampling protocol should minimize any effects of particle settling by virtue of the shallow cast depths and short times between sample collection and filtration, losses from particle settling are not quantified and both the 2003 and 2013 datasets could underestimate actual particulate trace metal concentrations. In 2003, sampling depths were limited to the upper 750 m between 62 and 27°N due to problems with the load-handling ability of the winch.

One change to sample collection in 2013 was the addition of a piece of acid-cleaned Teflon tubing to the interior of the GO-FLOs that attached to the stopcock and curved down to fit against the opposite side of the bottle with a beveled edge, as described by *Cutter and Bruland* [2012] and *Planquette and Sherrell* [2012]. The modification was made to facilitate draining of the entire bottle during particle sampling, including the small volume below the level of the stopcock. However, we must consider potential sampling artifacts introduced by addition of the tubing. If particle settling in the bottle was significant, the Telfon tubing could have allowed collection of particles at the bottom of the GO-FLO that would not have been captured during sampling in 2003. However, previous studies have concluded that this GO-FLO modification does not significantly counteract effects of particle settling [*Planquette and Sherrell*, 2012]. Additionally, we would expect particle settling effects to be greatest in mid- and high-latitude surface waters where high seasonal biological production would lead to large, rapidly-sinking aggregates. As will be discussed below, no significant increases in particulate trace metal concentrations were observed in these regions in 2013 compared to 2003. Instead, the largest changes were observed at low latitudes where particle disaggregation and degradation processes dominate and likely result in a pool of small suspended particles [*Barrett et al*., 2012; 2014]. Thus, it is improbable that the differences in particulate trace metal distributions between 2003 and 2013 could be the result of a sampling artifact introduced by modification of the GO-FLO bottles.

3.2.2 Analytical methods

Subsamples of filtered seawater (<0.4 μm) were collected into acid-washed 100 mL LDPE bottles, acidified to 0.024M HCl, and analyzed for dissolved Al concentrations using the flow injection method of *Resing and Measures* [1994]. The method had a detection limit of 0.5 nM with a precision of 3.0% in 2003 and a detection limit of 0.3 nM with a precision of 3.0% in 2013. Three SAFe and two GEOTRACES reference standards were run regularly and compared to consensus values for quality assurance and control in 2013 (**Table 3.1**).

The trace metal composition of suspended particulate matter samples was determined by energy-dispersive X-ray fluorescence (ED-XRF) at NOAA/PMEL on a Thermo Fisher Quant'X equipped

with a Rhodium Target X-Ray tube and an electronically cooled, lithium-drifted solid state detector using thin-film principles under a vacuum atmosphere. The ED-XRF protocol adapts the methods of *Feely et al*. [1991] and has been described previously by *Barrett et al*. [2012]. Analytical accuracy of the ED-XRF analysis is confirmed by analysis of certified reference material NIST SRM 2783, air particulate on filter media, which shows good agreement (+/- 8%) between certified and measured values for Al and Fe [*Barrett et al*., 2012]. Minimum detection limits for *in situ* seawater concentrations of particulate Al and Fe are 0.54 nM and 0.03 nM, respectively, given an average sample filtration volume of 8 L. Minimum detection limits are determined from a standard of known concentration and are defined as:

$$MDL = (3 \cdot \sqrt{I_b}) / (I_p / c) \qquad (3.1)$$

where I_b is the background intensity, I_p is the peak intensity, and c is the concentration of the standard. Method-blank values of 11.0 and 2.1 ng/cm^2 for Al and Fe, respectively, were determined from analysis of acid-cleaned filter blanks and subtracted from measured sample values. Precision of the XRF analyses was typically 3–11% for particulate Al and 4–8% for particulate Fe.

To account for differences in both station and depth spacing in the sampling plans for the two occupations of A16N, concentrations of particulate Fe, particulate Al and dissolved Al were subjected to a linear interpolation onto an evenly-spaced grid to compare the trace metal distributions between the 2003 and 2013. Difference plots were restricted to regions of sampling overlap between the two cruises at latitudes 2°S to 62°N. To determine average trace metal concentrations in features of interest along the transect, a Monte-Carlo type simulation (n=1000) was performed by randomly varying the sample data within the bounds of individual measurement uncertainties and calculating an average concentration for the region of interest in each interpolated concentration field. The non-parametric Kolmogorov-Smirov test [*Massey,* 1951] was applied to determine the significance of differences between the distribution of means calculated for each region by the Monte-Carlo approach for 2003 and 2013.

3.3 Results and discussion

3.3.1 Changes in particulate Al and Fe concentrations along A16N

3.3.1.1 Distributions of particulate Al and Fe in 2003 and 2013

The distributions of particulate Al (pAl) and particulate Fe (pFe) in the upper 1000 m along CLIVAR A16N in 2003 and 2013 are shown in **Fig. 3.2**. The major features of both the pAl and pFe

distributions that were reported in 2003 [*Barrett et al*., 2012] were also observed along the section in 2013, and are briefly described below.

At high-latitude stations, high pAl concentrations in surface waters result from mixing with river outflow from southern Iceland that carry high sediment loads. Re-suspension of sediments from shallow bottom depths over the Icelandic shelf can be seen in the deep pAl maxima in vertical profiles at these stations. Surface pAl concentrations are also elevated by scavenging of dissolved Al onto biogenic particles in productive coastal waters and, in 2003, in mid-latitude surface waters (~40–55°N) following the spring bloom in the North Atlantic. Concentrations of pAl are relatively low throughout the subtropical gyre, reflecting low rates of dust deposition on surface waters. In the tropical North Atlantic between ~10 and 20°N, pAl concentrations in surface waters are high (6–11 nM) due to intense seasonal aerosol dust deposition. Shipboard daily-integrated aerosol samples collected in 2003 [*Buck et al*., 2010a] and 2013 [*R. Shelley*, unpublished data] show peak concentrations of aerosol Al over a similar latitudinal range. Spatial patterns in the transport of aerosol dust across the tropical North Atlantic are largely controlled by the migration of the Intertropical Convergence Zone (ITCZ) and the distribution of peak surface-ocean pAl and aerosol Al flux observed in both A16N occupations is consistent with the northerly shift in aerosol transport expected in Northern hemisphere summer [*Husar and Prospero*, 1997]. The most prominent feature in the pAl distribution is a large subsurface region of elevated pAl concentrations (up to 20 nM in 2003 and 31 nM in 2013) that extends from 200 m down to maximum sampling depths (1000 m) between the equator and 20°N. This subsurface pAl maximum develops as aerosol dust particles deposited on surface waters settle through the upper water column and lithogenic particulate Al is released at depth during disaggregation and degradation of large sinking particles and biological aggregates. The spatial extent of this feature spans the full annual latitudinal range of peak dust transport from the African continent to the North Atlantic [*Husar and Prospero*, 1997]. There is no evidence of sedimentary influence on trace metal concentrations at this distance from the African continent. Tracers of sedimentary inputs such as dissolved Mn and ^{228}Ra are confined to regions within ~500 km of the coast [*Hatta et al*., 2015] and mineralogical assessment of particles has demonstrated that dust is the principal source of lithogenic material to the upper water column at these latitudes [*Ohnemus and Lam*, 2015].

Generally, concentrations of pFe along A16N (**Fig. 3.2d,e**) have a distribution similar to pAl as both trace metal species are supplied largely from the same lithogenic sources (primarily aerosol dust) and are subject to similar removal processes (aggregation and sinking) in the upper water column of the

North Atlantic. High concentrations of pFe introduced to surface waters from fluvial sources and at depth from shelf and bottom sediments can be seen in high-latitude pFe profiles. Maximum surface-ocean pFe concentrations at low latitudes (~10–20°N) result from intense seasonal deposition of Saharan dust and are consistent with shipboard estimates of the location of maximum aerosol Fe concentrations during A16N in both 2003 and 2013 [*Buck et al*., 2010a; *R. Shelley*, unpublished data]. The pFe distribution also indicates the presence of a large subsurface particulate plume at low latitudes that develops, in part, from export of dust deposited on overlying surface waters. However, unlike Al, Fe also undergoes strong biological cycling in the upper water column with uptake of dissolved Fe in the surface ocean and remineralization below the euphotic zone. At low latitudes (0–20°N) along A16N, dissolved Fe released by remineralization of sinking organic matter accumulates at depth in poorly-ventilated, low-oxygen waters below the euphotic zone. These waters are depleted in dissolved Fe relative to nitrate and remineralized carbon as inferred from AOU, suggesting relatively strong removal of dissolved Fe by scavenging onto particles [*Measures et al*., 2008a; *Hatta et al*., 2015]. Hence, in addition to the vertical transport of dust particles, scavenging of the dissolved Fe pool likely also contributes to the high concentrations observed at depth in pFe profiles under the Saharan dust plume.

3.3.1.2 Differences between 2003 and 2013 particulate Al distributions

Differences in the distributions of pAl in the upper water column between 2003 and 2013 are primarily due to changing lithogenic inputs to the open ocean, largely aerosol dust fluxes, and variability in processes that control particle dynamics in the ocean interior. We focus on two regions where differences in measured pAl concentrations between the 2003 and 2013 occupation of A16N are greatest: surface waters in the productive mid-latitudes and in the equatorial region under the atmospheric outflow of Saharan dust.

First, as shown in **Fig. 3.2c,** pAl concentrations in mid-latitude surface waters (~40–50°N) were lower (typically by > 5nM) than measured in 2003. While most pronounced in the surface ocean, pAl concentrations were also lower throughout the upper 1000 m in this region. In 2003, sampling occurred shortly after the onset of the North Atlantic spring bloom at these latitudes [*Henson et al*., 2009], where high concentrations of biogenic particles, primarily diatoms, are known to scavenge the surface-ocean dissolved Al pool accumulated from dust deposition over winter months [*Kremling and Hydes*, 1988; *Moran and Moore*, 1988]. This seasonal scavenging of dissolved Al is the probable source of the high pAl concentrations (up to 12.2 nmol L^{-1}) observed in surface waters in 2003 [*Barrett et al*., 2012], as well as elevated pAl at depth as biogenic particles are exported out of the surface ocean (**Fig. 3.2a**). The

absence of this pAl feature in 2013 (**Fig. 3.2b**) is most likely due to the difference in the timing of sampling (~6 weeks later in the year) compared to the 2003 occupation of A16N. Rapid sinking rates for POC (100–160 m d^{-1}) [*Lochte et al*., 1993] and diatom aggregates (~75 m d^{-1}) [*Briggs et al*., 2011] have been observed following the spring bloom in the subpolar North Atlantic during the 1989 JGOFS North Atlantic Bloom Experiment (NABE) and North Atlantic Bloom 2008 experiment (NAB08), respectively. By the time sampling commenced along A16N in 2013 (early August), high seasonal, bloom-induced pAl concentrations had likely already dissipated due to bloom decay and particle export. As shown in Fig. 3 for a repeat station at 45°N, an intense surface-ocean particulate Si maximum (>350 nM) in 2003 coincides with elevated pAl concentrations in the surface ocean (up to 8 nM) and at depth (>4 nM). Differences in the behavior of particulate Si and Al with depth reflects their differential remineralization [e.g., *Measures et al*., 2014]. In contrast, low surface ocean particulate Si concentrations (<50 nM) in 2013 suggests absence of bloom activity and low pAl concentrations are observed throughout the water column (<2 nM).

The largest differences in pAl between 2003 and 2013 were observed in the subtropical and equatorial North Atlantic (**Fig. 3.2c)**. Here, upper water column pAl distributions primarily reflect deposition of aerosol dust from the deserts of northern Africa [*Buck et a*l., 2010a]. In 2013, increased pAl concentrations were observed within the broad subsurface (>200 m) particulate plume at low latitudes that results from vertical transport of aerosol dust particles through the upper water column. At depths >200 m between 0 and 20°N, the average pAl concentration increased by 1.6 nM (14%) from a calculated mean of 11.5 $\pm$ 0.2 nM in 2003 to 13.1 $\pm$ 0.6 nM in 2013 (two-sample Kolmogorov-Smirov test, α<0.01).

A residence time of 1–4 years for this subsurface particulate feature can be calculated using average ocean pAl concentrations [*Barrett et al*., 2012 and this work], concentrations of total aerosol Al measured along A16N [*Buck et al*. 2010a; *R. Shelley*, unpublished data], an aerosol Al solubility of 10% for Saharan aerosols [*Buck et al*., 2010a], and an average aerosol deposition velocity of 1.2 cm s^{-1}, which is close to the estimate of *Duce et al*. [1991]. Estimates for aerosol deposition velocities are not well constrained and this value adds uncertainty to our estimate of pAl residence time. For example, a recent study by *Niedermeier et al*. [2014] measured mean aerosol deposition velocities of 0.2 cm s^{-1} for 1–10 µm mineral dust particles in the tropical northeast Atlantic, similar to the distribution of particle size in the A16N Saharan aerosol samples [*Buck et al*., 2010b]. Using the aerosol deposition velocity measured by *Niedermeier et al*. would increase residence times by up to a factor of 6 and thus our calculations are likely a conservative estimate.

Climatological estimates of dust flux to the surface ocean at these latitudes (2–20 g dust m^{-2} yr^{-1}) [*Zender et al*., 2003; *Jickells et al*., 2005; *Mahowald et al*., 2005] combined with an aerosol Al content of 8.0% [*Wedepohl*, 2005] generate similar estimates of residence time (<1 to 3 years). Multi-year residence times for pAl in the upper 1000 m is likely an effect of small particle size. This region is a zone of intense remineralization as evidenced by a high AOU, nitrate, and dissolved Fe [*Measures et al*., 2008; *Hatta et al*. 2015]. Small lithogenic particles delivered by aerosol deposition, typically are likely released at depth to the suspended matter pool as aggregates are subjected to remineralization and degradation processes. A decrease in the mean lithogenic particle size over the decade interval could increase the residence time of suspended particulate matter and result in the observed increase in ocean pAl concentrations. However, studies of the properties of Saharan aerosols over our study period show no indication that the mean particle size of lithogenic inputs to this region has decreased [*Ryder et al*., 2013[. Thus, observed pAl concentrations in the subsurface maximum at low latitudes represent a multi-year average signal of annual dust deposition and the increase in average pAl concentrations in this large-scale feature suggests an increase in dust deposition to surface waters in this region between 2003 and 2013.

Concentrations of pAl reach maximum concentrations in equatorial surface waters (10.9 nM in 2003 and 11.2 nM in 2013) at latitudes under the Saharan dust outflow (~0–20°N). If aerosol deposition to surface waters in this region increased between the two occupations of A16N as suggested from changes observed in the large particulate plume deeper in the water column, it may be expected that surface-ocean pAl concentrations would also be higher in 2013. However, the differences in average pAl concentrations between 2003 and 2013 in the mixed layer are less robust (typically <0.5nM), which is likely a result of the variability in dust deposition and the very short residence times expected for particles in the surface layer. A residence time for surface-ocean particulates in the equatorial North Atlantic can be calculated from surface inventories (<50 m) of pAl in both 2003 and 2013 and the measured and climatological aerosol input parameters described above. Resulting residence times are generally 1–5 weeks, although estimates range up to a maximum of 43 weeks due to the high degree of variability in aerosol deposition events. At the lower end, our estimate is comparable to previous work reporting residence times of 3–22 days for pAl in the equatorial North Atlantic from upper water column pAl concentrations and climatological dust fluxes [*Dammshäuser et al*., 2013] and a lithogenic particle residence time of 10–40 days in the subtropical North Atlantic using sediment trap data [*Bory and Newton*, 2000]. This short residence time implies that surface-ocean particulate trace metal

concentrations will be strongly influenced by the highly episodic nature of dust transport over the North Atlantic.

3.3.1.3 Differences between 2003 and 2013 particulate Fe distributions

Similar to the changes in pAl distributions along A16N between the two occupations, the largest differences in the pFe distribution between 2003 and 2013 were also observed in the subsurface particulate maximum in the equatorial North Atlantic (**Fig. 3.2f)**. Between the equator and 20^{o}N at depths below 200 m, average pFe concentrations increased by 0.9 nM (27%) from a calculated mean of 3.4 $\pm$ 0.02 nM in 2003 to 4.3 $\pm$ 0.02 nM in 2013 (two-sample Kolmogorov-Smirov test, α <0.01).

Inputs of pFe and pAl are expected to be closely coupled in this region given the strong atmospheric source common to both metals. Considering pAl as a proxy for lithogenic dust inputs, the increase in pFe (+27%) relative to pAl (+14%) between 2003 and 2013 suggests that vertical transport of dust particles would account for approximately half of the observed increase in pFe concentrations. The excess pFe at depth observed in 2013 could be due to increased scavenging of the high concentrations of subsurface dissolved Fe in this region (up to 2 nM in 2003) [*Measures et al*., 2008a]. We observe a significant increase in Fe:Al molar ratio of particles in the subsurface plume (0.29 $\pm$ 0.01 in 2003 and 0.32 $\pm$ 0.3 in 2013; p<0.01), implying changes in the internal cycling of Fe in the equatorial North Atlantic. For example, scavenging is known to be important in controlling the partitioning of remineralized Fe between dissolved and particulate phases in subsurface waters this region [*Measures et al*., 2008; *Hatta et al*., 2015] and could contribute to the changes in pFe observed been 2003 and 2013. Increased scavenging pressures could result from higher lithogenic particle loads in 2013. Likewise, average particulate P concentrations in this region more than doubled in 2013 compared to 2003 (**Appendix, Figure B.1**), indicating a higher concentration of biogenic particles, which are also efficient at scavenging dissolved Fe [*Balistrieri et al*., 1981]. While we cannot yet compare dFe distributions along A16N between 2003 and 2013, maximum dFe concentrations observed in the top 1000 m in 2003 [*Measures et al*., 2008] are typically higher (1.26–2.02 nM, 13 stations) than those observed in 2008 (0.98–1.47 nM, 6 stations; *R/V Oceanus* OC 449-2) by *Fitzsimmons et al*. [2013] in regions of sampling overlap, (6–18°N, 25–31°W), which would be consistent with an increase in scavenging rates.

It is unlikely that a change in the composition of aerosol sources between 2003 and 2013 could explain the increase in the Fe:Al ratios of ocean particulate matter. Analysis of aerosol samples collected daily along A16N suggests that the Fe:Al ratio of aerosol dust inputs to this region may have declined between the two occupations (0.32 $\pm$ 0.05 in 2003 and 0.27 $\pm$ 0.2 in 2013, p<0.01) [*Buck et al*., 2010; *R.*

Shelley, unpublished data]. Given the highly episodic nature of aerosol transport and the short collection time for these samples, this difference may or may not accurately reflect long-term trends in aerosol composition, but these samples provide no evidence for an increase in the Fe:Al ratio of source aerosols that would explain the changes observed in the chemistry of ocean particulate samples.

In efforts to compare our A16N timepoints to other datasets , we also consider particulate Al and Fe data collected during the 2010/2011 GEOTRACES North Atlantic Zonal Transect, between our two occupations of A16N [*Ohnemus and Lam*, 2015; *Twining et al.,* 2015]. The intersection between these two transects in the region of interest in the equatorial North Atlantic occurs at approximately 19°N and 29°W, a location with high spatial gradients in dust transport and deposition, and at the interface between two distinct water masses at intermediate depths; these factors may introduce additional variability to particulate trace metal measurements (**Appendix, Figure B.2**). Additionally, methodological differences in sample collection further complicate data comparison. Particulate sampling by *Ohnemus and Lam* [2015] employed a 0.8 µm minimum filter size as compared to the 0.4 µm filter used during both A16N occupations. We note the significant differences between particulate Al concentrations at depth (>200 m) at open-ocean stations in the eastern North Atlantic from 0.8 µm filter samples and 0.45 µm filter samples collected during the GEOTRACES section [*Twining et al*., 2015] (**Appendix, Figure B.3**). Hence, we conclude that methodological differences preclude meaningful comparison of these two datasets.

3.3.2 Changes in dissolved Al concentrations along A16N

3.3.2.1 Distributions of dissolved Al in 2003 and 2013

The distribution of dissolved Al (dAl) in the upper 1000 m of the water column along A16N in 2013 is broadly similar to that observed a decade earlier (**Fig. 3.4**) [*Measures et al*., 2008; *Barrett et al*., 2012]; these general features are briefly described below.

Surface-ocean dAl concentrations reflect input of Al from the deposition and partial dissolution of atmospheric aerosols and removal by particle scavenging processes. The dAl surface maxima observed at low latitudes (~0–10°N) result from intense seasonal deposition of aerosol dust on the surface ocean in the equatorial North Atlantic. Outside of the equatorial region, surface concentrations of dAl are much lower, reflecting reduced dust inputs. At mid-latitude stations, scavenging of dAl onto biogenic particles following the spring bloom in the North Atlantic (see discussion in section 3.3.1.2) leads to strong removal of dAl from surface waters as Al is transferred to the particulate phase; thus dAl profiles exhibit minimum values at the surface. There are two subsurface features in the dAl distribution

that result from subduction of Al-rich surface waters. The first is the local maximum in dAl concentrations (>23 nM in 2003 and >25 in 2013) centered at depths of ~300 m in subtropical waters (20–35°N). This signal originates from the subduction of dust-imprinted waters in the western basin that form the Atlantic subtropical mode waters. Similarly, deposition of Saharan dust on the Mediterranean basin leads to Al-rich surface waters that are subducted and transported through the Strait of Gibraltar as Mediterranean outflow water (MOW). The CLIVAR A16N section transects the MOW at 35–41°N where elevated dAl concentrations were observed at depths below ~700 m during both occupations, as indicated by the local salinity maximum [*Measures et al*., 2008a]. At more northerly stations along A16N (>40°N), minimum dAl values at the surface and increasing dAl with depth reflect the strong removal of dAl from the surface mixed layer by seasonal scavenging pressures from high concentrations of biogenic particles as described in section 3.3.1.2.

3.3.2.2 Differences between 2003 and 2013 dissolved Al distributions

Similar to the changes observed in pAl and pFe, increased concentrations of dAl were observed in 2013 in regions heavily impacted by delivery of aerosol dust from low-latitude continental sources in surface waters in the tropical North Atlantic (0–20°N) and where A16N intersects subtropical mode waters (**Fig. 3.4c**).

The largest differences in the dAl distribution between the two occupations of A16N are found in North Atlantic equatorial surface waters (0–20°N) where high rates of dust deposition and the partial dissolution of aerosol Al lead to local maxima in surface-ocean dAl concentrations [*Measures et al*., 2008a]. Maximum dAl concentrations observed in this region increased from 36 $\pm$ 1.1 nM in 2003 to 42 $\pm$ 1.3 nM in 2013 and average dAl concentrations in the upper 50 m increased by 3.1 nM (16%) from 19.5 $\pm$ 0.02 nM in 2003 to 22.6 $\pm$ 0.2 nM in 2013. Atmospheric dust transport across the equatorial North Atlantic is controlled spatially by the seasonal shift in the ITCZ, which is centered approximately between the equator and 10°N during boreal winter and farther north between 10 and 20°N during summer [*Husar and Prospero*, 1997]. The residence time of surface-ocean dAl in the eastern tropical North Atlantic has been estimated to be on the order of several months from both seasonal observations and modeling work [*Helmers and van der Loeff*, 1993; *Dammshäuser et al*., 2011; *van Hulten et al*., 2013]. Due to its relatively short residence time, dAl accumulates in surface waters from 0 to 10°N in the winter then slowly decays in this region over the summer as the location of maximum dust deposition shifts north, as can be seen in the seasonal observations of *Helmers and van der Loeff* [1993]. Comparison of dAl profiles at 19°–21°N with dAl data of *Measures et al*. [2014] collected at

similar latitudes during winter months on the 2011 GEOTRACES NAZT also illustrates the response of surface-ocean dAl concentrations to the seasonality of dust inputs to this region (**Appendix, Figure B.4**); subsurface features in these dAl profiles reflect local boundaries between intermediate-depth water masses (**Appendix, Figure B.5**).

Because of the lag of ~6 weeks between the timing of sampling in 2003 and 2013, dAl surface concentrations between 10–20°N in 2013 could be higher due to extended exposure to summertime aerosol deposition. However, if aerosol inputs were constant between 2003 and 2013, dAl concentrations over 0–10°N would be expected to be lower in 2013 due to a longer time for particle scavenging to remove dAl from surface waters after local inputs ceased. Instead, comparison of the 2003 and 2013 dAl distributions shows an increase in average surface concentrations over 0–10°N as well (3 nM). It is unlikely that reduced scavenging pressures could explain the persistence of the dAl signal given the increased particulate trace metal loading discussed above. Hence, the increase in average dAl concentrations observed in 2013 compared to 2003 in surface waters (>50 m) between the equator and 20°N is most likely the result of increased atmospheric dust deposition in 2013 compared to 2003. Due to the relatively short residence time of surface-ocean dAl in this region, concentration differences can be attributed solely to inter-annual variability in dust deposition [*Prospero and Lamb*, 2003]. However, the sign and magnitude of the observed change is consistent with the long-term trend of increasing dust deposition across the equatorial North Atlantic suggested by the particulate Al and Fe.

Increased dAl concentrations between 2003 and 2013 are also observed along potential density surfaces σ_θ = 26.5 to 26.9 (approximately 200–400 m) in the core of the subtropical mode water along A16N between 25 and 35^{o}N (**Fig. 3.5**). Increased dAl concentrations in these mode waters suggest that dust deposition to surface waters may have been higher in the western North Atlantic during mode water formation. Long-range transport of Saharan dust across the North Atlantic is a major contributor to atmospheric aerosol loading over the western North Atlantic [*Li et al*., 1996; *Prospero and Lamb*, 2003; *Prospero and Mayol-Bracero*, 2013] and Saharan dust deposition is a major source of trace metals, notably Al, to subtropical surface waters in the western Atlantic basin [*Jickells*, 1999]. The average increase in dAl in the subtropical mode water signal (1.0 nM, 5%) is smaller than the relative increases in particulate (+14%) and dissolved (+16%) Al observed in the equatorial region along the A16N transect, which result from local dust deposition in the eastern basin rather than transit of dAl-imprinted water masses. This variation could be due to real differences between the dust transport pathways or deposition processes in the eastern and western Atlantic. Although the residence time of subtropical mode waters in the North Atlantic is relatively short (~4 years) [*Trossman et al*., 2012], the transit time

of subducted mode waters from their origin in the western basin could contribute to differences between dAl inventories of local and advected water masses. Additionally, the residence time of surface-ocean dAl in the region of mode water formation in the western basin is likely at least twice as long as the residence time of either the dAl or pAl signal in the eastern basin; thus subtropical mode water dAl may also reflect changes in dust deposition over the longer integration period in mode water source regions. In regions of the western Atlantic where formation of North Atlantic subtropical mode water occurs [*Hanawa and Talley*, 2001; *Kelly and Dong*, 2013], model output estimates the residence time of surface-ocean dAl to be 4–20 years [*Gehlen et al*., 2003; *Han et al*., 2008]. After subduction in the western basin, dAl in this water mass is subject to greatly reduced particle scavenging pressures, leading to semi-conservative behavior of dAl in subsurface waters [*Orians and Bruland*, 1986; *Measures and Edmond*, 1990].

Elevated dAl concentrations are also observed in the high-salinity Mediterranean outflow water (MOW) at ~700–1100 m between 35 and 41°N along A16N during both occupations. Due to restrictions on sampling depth at these stations, the 2003 occupation sampled the upper portion of this water mass but missed the core of the signal, making potential changes in the dAl concentrations in this water mass difficult to discern. In 2013, dAl concentrations in the core of the MOW (800–1000 m) reached a maximum of 29.5 nM. Concentrations of dAl in the MOW during the 2013 occupation of A16N are comparable to previous observations of dAl maxima in the MOW in the eastern subtropical North Atlantic (**Fig. 3.6**). The variability in dAl concentrations between the A16N data and previous studies likely primarily reflects spatial differences in sampling sites and the dilution of MOW with low-Al North Atlantic Central Water as it moves along northern and westward flow branches through the eastern North Atlantic [*Lozier et al*., 1995]. Satellite observations of aerosol distributions and aerosol sampling at ground-based sites throughout the Mediterranean basin indicate that Saharan dust inputs vary temporally and spatially on relatively short timescales, largely controlled by changes in atmospheric circulation patterns with robust correlation with the summer North Atlantic Oscillation index [*Moulin et al*., 1998; *Dayan et al*., 2008]. Previous studies have reported that dust transport to the Mediterranean decreased between the mid-1980s to the late 1990s, increased from the late 1990s to the mid-2000s, and shows a negative trend from the mid-2000s to 2011 [*Ridame et al*., 1999; *Antoine and Nobileau*, 2006; *Pey et al*., 2013]. However, these trend reversals in dust deposition to the Mediterranean have occurred on much shorter periods than the timescale of deep water circulation in the Mediterranean basin, which is on the order of several decades [*Chou and Wollast*, 1997] and controls dAl concentrations in the MOW. Hence, the long residence time of Al-enriched water in the Mediterranean

basin would, to a large extent, likely integrate any variability in aerosol Al input to Mediterranean surface waters.

3.3.3 Trends in atmospheric dust transport over the equatorial North Atlantic Ocean

In **Fig. 3.7**, the trace metal data from the subsurface particulate plume at low latitudes (pAl and pFe), surface waters in the tropical North Atlantic (dAl), and North Atlantic subtropical mode waters (dAl) are plotted for both 2003 and 2013, showing the increase in both mean and maximum trace metal concentrations observed for each region. **Table 3.2** summarizes estimated residence times for pAl, pFe, and dAl features in equatorial and subtropical North Atlantic heavily impacted by the deposition of atmospheric dust from the deserts of northern Africa and the average change in trace metal concentrations observed for each feature between 2003 and 2013. Increased inventories of these trace metal species suggest that dust deposition to the eastern tropical North Atlantic increased between 2003 and 2013. These differences reflect a combination of inter-annual variability and the decadal trend in dust deposition that will vary with the residence time of the trace metal signal considered.

Because of the importance of atmospheric aerosols and their feedbacks in the climate system, observational efforts have greatly expanded over the last several decades and have resulted in availability of records of global aerosol distributions from various satellite products (e.g., MODIS, AVHRR, SeaWiFS, EOS, TOMS, MISR) and ground-based aerosol sampling networks (e.g., AERONET, IMPROVE) [*Chin et al*., 2013]. The changes in the average global aerosol loading over the last several decades detected from satellite products are small relative to the total aerosol loading and recent analyses have disagreed on the size and direction of change in average global aerosol transport [*Mishchenko et al*., 2007; *Zhang and Reid*, 2010; *Hsu et al*., 2012]. However, many analyses have found robust regional trends in aerosol optical depth (AOD) due to changing local natural and anthropogenic sources. There is significant agreement among studies employing various satellite, ground-based sampling, and modelling products that dust transport across the tropical North Atlantic Ocean has decreased between the 1980s and late 2000s [*Mishchenko and Geogdzhayev*, 2007; *Foltz and McPhaden*, 2008; *Wong et al*., 2008; *Zhao et al*., 2008; *Evan and Mukhopadhyay*, 2010; *Zhang and Reid*, 2010; *Hsu et al*., 2012; *Chin et al*., 2013]. These studies report negative AOD trends in regions over the tropical North Atlantic affected by African dust transport of -0.01 to -0.1/decade for the last 2 decades, although most estimates fall within -0.03 to -0.05/decade [*Foltz and McPhaden*, 2008; *Zhao et al*., 2008; *Zhang and Reid*, 2010; *Hsu et al*., 2012]. Average annual AOD in our study region is estimated to be 0.3–

0.5 [*Foltz and McPhaden*, 2008; *Zhang and Reid*, 2010; *Chin et al*., 2013], making the estimated decadal rate of AOD decline between 2 and 30%.

MODIS satellite images showing AOD over the North Atlantic integrated over the 2003 and 2013 cruise dates as well as for the preceding 12 months are shown in **Fig. 3.8**. Although aerosol transport is expected to be highly variable both seasonally and interannually, the decline in AOD over the tropical North Atlantic during the 2013 occupation of A16N compared to a decade earlier is consistent with the general trend of decreasing regional aerosol loads over the last several decades reported by the above studies. The trend of decreasing AOD over the tropical North Atlantic has been linked to reduced dust production, perhaps due to increased precipitation over regions of dust generation [*Prospero and Lam*, 2003; *Foltz and McPhaden*, 2008], greening of African deserts [*Cowie et al*., 2013], or changes in atmospheric circulation patterns [*Wong et al*., 2008; *Hsu et al*., 2012]. Recent work has also found that decreased AOD over the tropical North Atlantic is closely associated with increased precipitation over the tropical North Atlantic Ocean [*Chin et al*., 2013]. Hence, both dust generation in continental source regions and removal efficiency (precipitation) over the ocean are important controls on trends in dust AOD over the tropical North Atlantic.

The increased inventories of pAl, pFe, and dAl in the upper 1000 m along A16N between 2003 and 2013 we observe in this study suggests that aerosol dust deposition on surface waters increased over this timeframe as average AOD over the tropical North Atlantic has declined. Wet deposition of atmospheric aerosols is the primary mechanism for the delivery of trace metals to the open ocean in the tropical North Atlantic [*Hand et al*., 2004]. Our repeat observations of trace metal distributions along A16N are consistent with the findings of *Chin et al*. [2013] that removal of aerosol dust by precipitation over the open ocean is contributing to declining AOD trends over the tropical North Atlantic Ocean over the last several decades. Indeed, despite evidence that dust generation in desert source regions may be declining, our repeat of the A16N line indicates that ocean trace metal inventories in the eastern North Atlantic have not declined as a result, but rather have increased by 5–15%. This is consistent with observations that aerosol deposition processes have intensified as the magnitude or spatial patterns of precipitation shift, likely driven by increasing sea-surface temperatures as suggested by a number of previous studies [*Wong et al*. 2008; *Foltz and McPhaden*, 2008; *Wang et al*., 2012; *Chin et al*., 2013].

3.4 Conclusions

Repeat trace metal observations along CLIVAR A16N have allowed us to examine changes in large-scale trace metal features in the equatorial and sub-tropical North Atlantic impacted by dust

deposition on timescales of weeks to months (surface dAl) and over multiple years (subtropical mode water dAl and subsurface pAl and pFe), which suggest that dust deposition on surface waters likely increased by up to 15% between 2003 and 2013. This increase in trace metal concentrations in the upper water column support recent observational work linking declining aerosol optical depth over the North Atlantic to increased removal via precipitation over the ocean, especially in the eastern North Atlantic. Discussion of future changes in the atmospheric delivery of biologically-important trace metals to the oceans, most notably Fe [e.g., *Mahowald et al*., 2009], have primarily made use of modeling studies examining predicted changes in the global dust transport stemming from changes in the spatial extent and emission strength of desert source areas [*Mahowald and Luo*, 2003; *Tegen et al*., 2004; *Woodward et al*., 2005; *Mahowald*, 2007]. This work emphasizes the need to robustly link trends in atmospheric dust loading to deposition rates over the ocean by more accurately representing deposition mechanisms such as wet deposition in models, a need that has been previously highlighted by other researchers [*Prospero et al*., 2010; *Schultz et al*., 2012].

3.5 Appendix

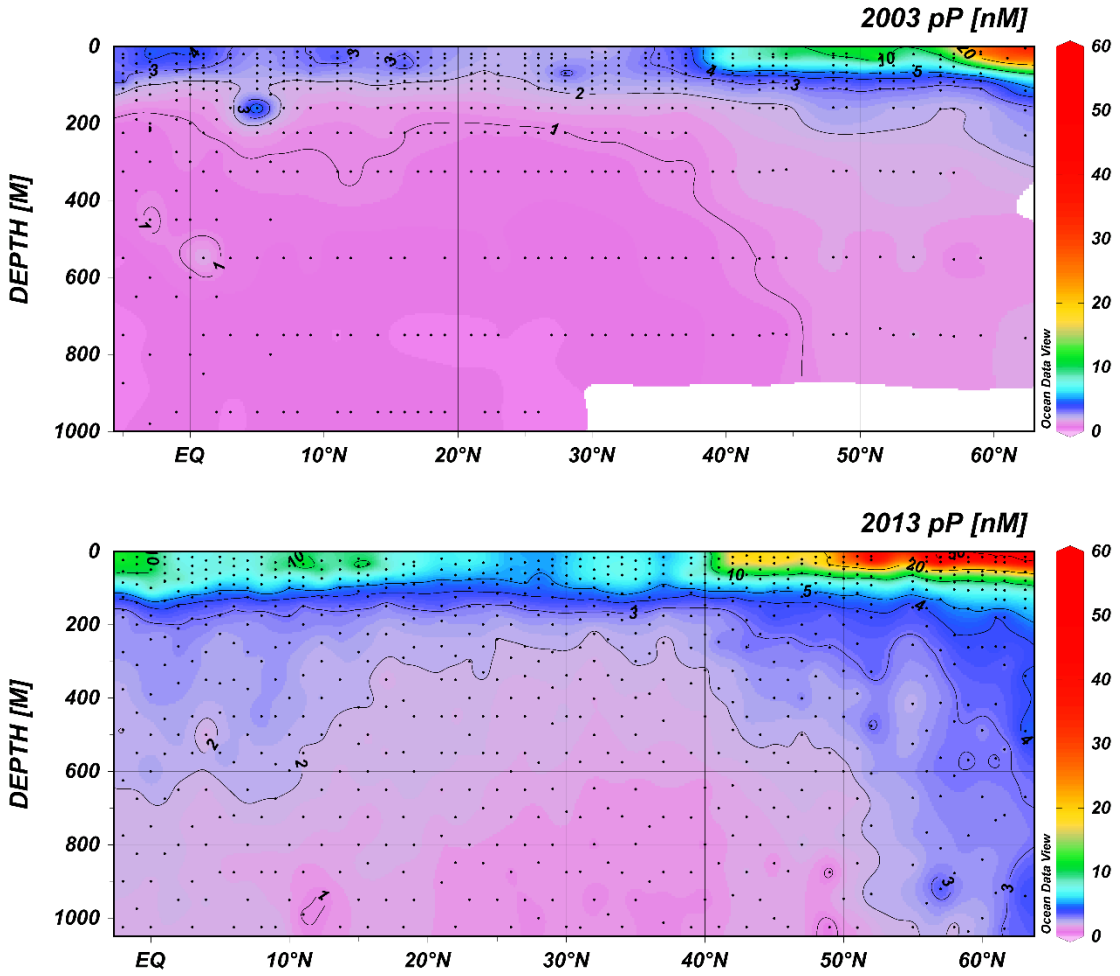

Figure B.1. Distributions of particulate P in nmol L^{-1} along CLIVAR A16N in 2003 (top panel) and 2013 (bottom panel); black dots represent individual sample measurements. Note that color scale has been modified to more clearly show concentrations <10 n nmol L^{-1}.

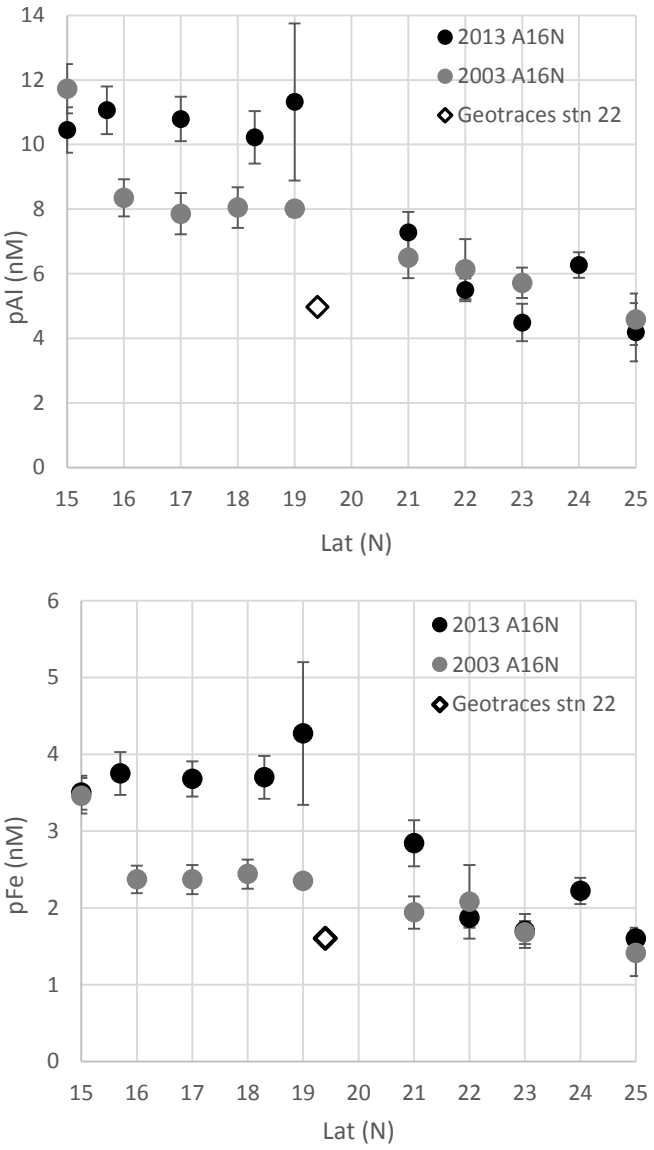

Figure B.2. Average concentrations of particulate Al in nmol L^{-1} over the depth range 200–1000 m at stations 15–25°N along 2013 and 2003 CLIVAR A16N (circles) plotted with average pAl concentration at 200–1000 m at 2011 GEOTRACES NAZT station 11-22 (diamond) [*Ohnemus and Lam*, 2015]. Data from *Ohnemus and Lam* is the sum of particulate Al concentrations from two size fractions (0.8–51 µm and >51 µm). CLIVAR A16N particulate Al concentrations are from 0.4 µm filter samples. Bottom panel is same but for particulate Fe.

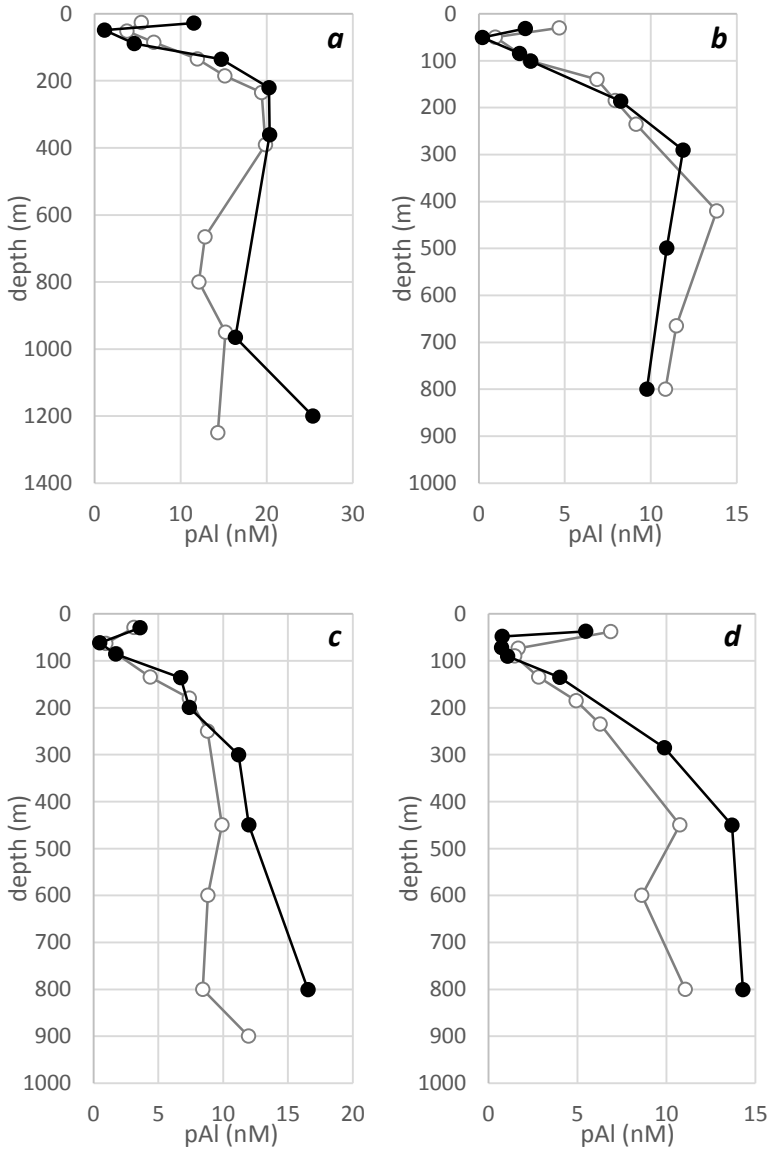

Figure B.3. Depth profiles of particulate Al at GEOTRACES NAZT stations 10-9 (a; 17.4°N, 24.5°W), 10-10 (b; 17.4°N, 22.8°W), 10-11 (c; 17.4°N, 20.8°W), and 10-12 (d; 17.4°N, 18.3°W) as determined by in situ pumps with minimum 0.8 µm filter size (open symbols) [*Ohnemus and Lam*, 2015] and discrete bottle sampling with 0.45 µm filter size (closed symbols) [*Twining et al*., 2015]. Station locations move progressively off-shore from the African margin (station 10-9) to open-ocean waters (station 10-12). In situ pump data is the sum of particulate Al concentrations from two size fractions (0.8–51 µm and >51 µm). Bottle data is either the sum of particulate Al concentrations from labile and refractory fractions, or from a total digest as described in *Twining et al*. [2015].

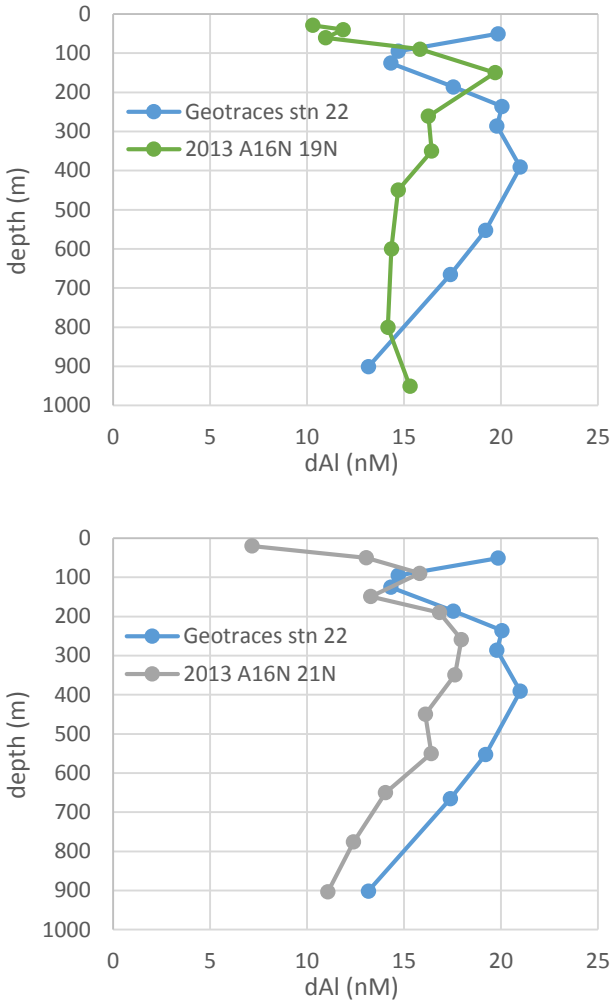

Figure B.4. Left panel: Concentration of dissolved Al in nmol L^{-1} at 2003/2013 CLIVAR A16N station 94 (19.0°N, 29.0°W) [*Measures et al*., 2008; this work] and 2011 GEOTRACES NAZT station 11-22 (19.4°N, 29.4°W) [*Measures et al*., 2014]. Right panel: Concentration of dissolved Al in nmol L^{-1} at 2003/2013 CLIVAR A16N station 90 (21.0°N, 28.4°W) [*Measures et al*., 2008; this work] and 2011 GEOTRACES NAZT station 11-22 (19.4°N, 29.4°W) [*Measures et al*., 2014].

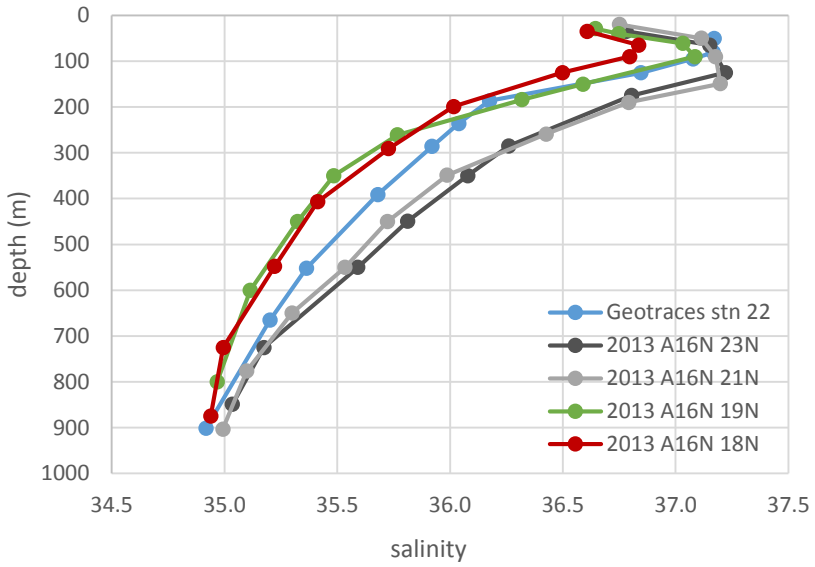

Figure B.5. Salinity profiles at 2011 GEOTRACES NAZT station 11-22 (19.4°N, 29.4°W) and at 2013 CLIVAR A16N stations between 18°N and 22°N.

3.6 References

Antoine, D., Nobileau, D., 2006. Recent increase of Saharan dust transport over the Mediterranean Sea, as revealed from ocean color satellite (SeaWiFS) observations. J. Geophys. Res. 111, D12214.

Balistrieri, L., Brewer, P.G., Murray, J.W., 1981. Scavenging residence times of trace metals and surface chemistry of sinking particles in the deep ocean. Deep Sea Res. 28, 101–121.

Barrett, P.M., Resing, J.A., Buck, N.J., Buck, C.,S, Landing, W.M., Measures, C.I., 2012. The trace element composition of suspended particulate matter in the upper 1000 m of the eastern North Atlantic Ocean: A16N. Mar. Chem. 142–144, 41–53.

Barrett, P.M., Resing, J.A., Buck, N.J., Feely, R.A., Bullister, J.L., Buck, C.S., Landing, W.M., 2014. Calcium carbonate dissolution in the upper 1000 m of the eastern North Atlantic. Global Biogeochem. Cycles 28, 386–397.

Bory, A.J.-M., Newton, P.P., 2000. Transport of airborne lithogenic material down through the water column in two contrasting regions of the eastern subtropical North Atlantic. Global Biogeochem. Cycles 14, 297–315.

Boyd, P.W., Ellwood, M.J., 2010. The biogeochemical cycle of iron in the ocean. Nature Geosci. 3, 675–682.

Briggs, M., Perry, M.J., Ivona Cetinić, I., Lee, C., D'Asaro, E., Gray, A.M., Rehm, E., 2011. High-resolution observations of aggregate flux during a sub-polar North Atlantic spring bloom. Deep-Sea Res. I 58, 1031–1039.

Buck, C.S., Landing, W.M., Resing, J.A., Measures, C.I., 2010a. The solubility and deposition of aerosol Fe and other trace elements in the North Atlantic Ocean: observations from the A16N CLIVAR/CO2 repeat hydrography section. Mar Chem. 120, 57–70.

Buck, C.S., Landing, W.M., Resing, J.A., 2010b. Particle size and aerosol iron solubility: A high-resolution analysis of Atlantic aerosols. Mar. Chem. 120, 14–24.

Chin, M., T. Diehl, Q. Tan, J.M. Prospero, R.A. Kahn, L.A. Remer, H. Yu, A.M. Sayer, H. Bian, I.V. Geogdzhayev, B.N. Holben, S.G. Howell, B.J. Huebert, N.C. Hsu, D. Kim, D.L. Kucsera, R.C. Levy, M.I. Mishchenko, X. Pan, P.K. Quinn, G.L. Schuster, D.G. Streets, S.A. Strode, O. Torres, and X.-P. Zhao, 2013: Multi-decadal variations of atmospheric aerosols from 1980 to 2009: sources and regional trends. Atmos. Chem. Phys. Discuss. 13, 19751–19835.

Chou, L., Wollast, R., 1997. Biogeochemical behavior and mass balance of dissolved aluminum in the western Mediterranean Sea. Deep-Sea Res. II 44, 741–768.

Conway, T.M., John, S.G., 2014. Quantification of sources of dissolved iron to the North Atlantic Ocean using iron isotopes. Nature, 511, 212–215.

Cowie, S.M., Knippertz, P., Marsham, J.H., 2013. Are vegetation-related roughness changes the cause of the recent decrease in dust emission from the Sahel? Geophys. Res. Lett. 40, 1868–1872.

Cutter, G.A., Bruland, K.W., 2012. Rapid and noncontaminating sampling system for trace elements in global ocean surveys. Limnol. Oceanogr. Methods 1, 425–436.

Dammshäuser, A., Wagener, T., Croot, P.L., 2011. Surface water dissolved aluminum and titanium: tracers for specific timescales of dust deposition to the Atlantic? Geophys. Res. Lett, 38, 6–11.

Dammshäuser, A., Wagener, T., Garbe-Schönberg, D., Croot, P.L., 2013. Particulate and dissolved aluminum and titanium in the upper water column of the Atlantic Ocean. Deep-Sea Res. I 73, 127–139.

Dayan, U., Ziv, B., Shoob, T., Enzel, Y., 2008. Suspended dust over southeastern Mediterranean and its relation to atmospheric deposition. Int. J. Climatol. 28, 915–924.

de Jong, J.T.M., Boye, M., Gelado-Caballero, M.D., Timmermans, K.R., Veldhuis, M.J.W., Nolting, R.F., van den Berg, C.M.G., de Baar, H.J.W., 2007. Inputs of iron, manganese and aluminium to surface waters of the Northeast Atlantic Ocean and the European continental shelf. Mar. Chem. 107, 120–142.

Duce, R.A., Tindale, N.W., 1991. Atmospheric transport of iron and its deposition in the ocean. Limnol. Oceanogr. 36, 1715–1726.

Duce, R.A., et al., 1991. The atmospheric input of trace species to the world ocean. Global Biogeochem. Cycles 5, 193–259.

Evan, A.T., Mukhopadhyay, S., 2010. African Dust over the Northern Tropical Atlantic: 1955–2008. J. Appl. Meterorol. Climatol. 49, 2213–2229.

Feely, R.A., Massoth, G. J., Lebon, G.T., 1991. Sampling of marine particulate matter and analysis by X-ray fluorescence spectrometry. *Marine Particles: Analysis and Characterization, Geophys. Monogr.*, No. 63, Amer. Geophys. Union, 251–257.

Fitzsimmons, J.N., Zhang, R., Boyle, E.A., 2013. Dissolved iron in the tropical North Atlantic Ocean. Mar. Chem. 154, 87–99.

Foltz, G.R., McPhaden, M.J., 2008. Trends in Saharan dust and tropical Atlantic climate during 1980–2006. Geophys. Res. Lett. 35, L20706.

Gehlen, M., Heinze, C., Maier-Reimer, E., Measures, C.I., 2003. Coupled Al-Si geochemistry in an ocean general circulation model: a tool for the validation of oceanic dust-deposition fields? Global Biogeochem. Cycles 17, 1028.

Han, Q., Moore, J.K., Zender, C., Measures, C., Hydes, D., 2008. Constraining oceanic dist deposition using surface ocean dissolved Al. Global Biogeochem. Cycles 22, GB2003, doi: 10.1029/2007GB002975.

Hanawa, K., Talley, L.D., 2001. Mode waters. *Ocean Circulation and Climate: Observing and Modelling the Global Ocean*, G. Sielder, J. Church, and J. Gould, Eds., Elsevier, 373–386.

Hand, J.L., Mahowald, N.M., Chen, Y., Siefert, R.L., Luo, C., Subramaniam, A., Fung, I. 2004. Estimates of atmospheric-processed soluble iron from observations and a global mineral aerosol model: Biogeochemical implications. J. Geophys. Res. 109, D17205.

Hatta, M., Measures, C.I., Wu, J., Roshan, S., Fitzsimmons, J.N., Sedwick, P., Morton, P., 2015. An overview of dissolved Fe and Mn Distributions during the 2010–2011 U.S. GEOTRACES North Atlantic Cruises: GEOTRACES GA03. Deep-Sea Res. II 116, 117–129.

Helmers, E., van der Loeff, M.M.R., 1993. Lead and aluminum in Atlantic surface waters (50°N to 50°S) reflecting anthropogenic and natural sources in the eolian transport. J. Geophys. Res. 98, 20261–20273.

Henson, S.A., Dunne, J.P., Sarmiento, J.L., 2009. Decadal variability in North Atlantic phytoplankton blooms. J. Geophys. Res. 114, C04013.

Hsu, N.C., Gautam, R., Sayer, A.M., Bettenhausen, C., Li, C., Jeong, M.J., Tsay, S.-C., Holben, B.N., 2012. Global and regional trends of aerosol optical depth over land and ocean using SeaWiFS measurements from 1997 to 2010. Atmos. Chem. Phys. 12, 8037–8053.

Husar, R., Prospero, J., 1997. Characterization of tropospheric aerosols over the oceans with the NOAA advanced very high resolution radiometer optical thickness operational product. J. Geophys. Res. 102, 16899–16909.

Hydes, D.J., 1983. Distribution of aluminium in waters of the North East Atlantic 25°N to 35°N. Geochim. Cosmochim. Acta 47, 967–973.

Jenkins, W.J., Smethie, W.M., Boyle, E.A., Cutter, G.A., 2014. Water mass analysis for the U.S. GEOTRACES (GA03) North Atlantic sections. Deep-Sea Res. II doi:10.1016/j.dsr2.2014.11.018.

Jickells, T., 1999. Inputs of dust derived elements to the Sargasso Sea; a synthesis. *Mar. Chem.*, **68**, 5–14.

Jickells, T.D., An, Z.S., Andersen, K.K., Baker, A.R., Bergametti, G., Brooks, N., Cao, J.J., Boyd, P.W., Duce, R.A., Hunter, K.A., Kawahata, H., Kubilay, N., laRoche, J., Liss, P.S., Mahowald, N., Prospero, J.M., Ridgwell, A.J., Tegen, I., Torres, R., 2005. Global iron connections between desert dust, ocean biogeochemistry, and climate. Science 308, 67–71.

Kelly, K.A., Dong, S., 2013. The contributions of atmosphere and ocean to North Atlantic Subtropical Mode Water volume anomalies. Deep-Sea Res. II 91, 111–127.

Kramer, J., Laan, P., Sarthou, G., Timmermans, K.R., de Baar, H.J.W., 2004. Distribution of dissolved aluminium in the high atmospheric input region of the subtropical waters of the North Atlantic Ocean. Mar. Chem. 88, 85–101.

Kremling, K., Hydes, D., 1988. Summer distribution of dissolved Al, Cd, Co, Cu, Mn and Ni in surface waters around the British Isles. Cont. Shelf Res. 8, 89–105.

Krishnamurthy, A., Moore, J.K., Mahowald, N., Luo, C., Zender, C.S., 2010. Impacts of atmospheric nutrient deposition on marine biogeochemistry. J. Geophys. Res. 115, G01006.

Li, X., Marin, H., Savoie, D., Voss, K., Prospero, J.M., 1996. Dominance of mineral dust in aerosol light-scattering in the North Atlantic trade winds. Nature 380, 416–419.

Lochte, K., Ducklow, H.W., Fasham, M.J.R., Stienen, C., 1993. Plankton succession and carbon cycling 47°N 20°W during the JGOFS North Atlantic Bloom Experiment. Deep-Sea Res. II 40, 91–114.

Lozier, M.S., Brechner Owens, W., Curry, R.G., 1995. The climatology of the North Atlantic. Prog. Oceanogr. 36, 1–44.

Mahowald, N.M., 2007. Anthropocene changes in desert area: Sensitivity to climate model predictions. Geophys. Res. Lett. 34, L18817.

Mahowald, N.M., Luo, C., 2003. A less dusty future? Geophys. Res. Lett. 20, 1903.

Mahowald, N., Baker, A.R., Bergametti, G., Brooks, N., Duce, R.A., Jickells, T.D., Kubilay, N., Prospero, J.M., Tegen, I., 2005. Atmospheric global dust cycle and iron inputs to the ocean. Global Biogeochem. Cycles 19, GB4025.

Mahowald, N.M., Muhs, D.R., Levis, S., Rasch, P.J., Yoshioka, M., Zender, C.S., Luo, C., 2009. Atmospheric iron deposition: Global distribution, variability, and human perturbations. Annu. Rev. Mar. Sci. 1, 245–278.

Massey, F.J., 1951. The Kolmogorov-Smirnov Test for Goodness of Fit. J. Amer. Statist. Assoc. 46, 68–78.

Measures, C.I., 1995. The distribution of Al in the IOC stations of the eastern Atlantic between 30°S and 34°N. Mar. Chem. 49, 267–281.

Measures, C.I., and Brown, E.T., 1996. Estimating dust input to the Atlantic Ocean using surface water Al concentrations. *The Impact of Desert Dust Across the Mediterranean*, S. Guerzoni and R. Chester, Eds., Kluwer Acad., 301–311.

Measures, C.I., Edmond, J.M., 2000. Aluminium in the South Atlantic: steady state distribution of a short residence time element. J. Geophys. Res. 95, 5331–5340.

Measures, C.I., Vink, S., 2000. On the use of dissolved aluminum in surface waters to estimate dust deposition to the ocean. Global Biogeochem. Cycles 14, 317–327.

Measures, C.I., Landing, W.M., Brown, M.T., Buck, C.S., 2008a. High-resolution Al and Fe data from the Atlantic Ocean CLIVAR-CO2 Repeat Hydrography A16N transect: Extensive linkages between atmospheric dust and upper ocean geochemistry. Global Biogeochem. Cycles 22, GB1005.

Measures, C. I., Landing, W.M., Brown, M.T., Buck, C.S., 2008b. A commercially available rosette system for trace metal-clean sampling. Limnol. Oceanogr. Methods 6, 384–394.

Measures, C., Hatta, M., Fitzsimmons, J., Morton, P., 2014. Dissolved Al in the zonal N Atlantic section of the US GEOTRACES 2010/2011 cruises and the importance of Hydrothermal inputs. Deep-Sea Res. II doi: 10.1016/j.dsr2.2014.07.006.

Mishchencko, M.I., Geogdzhayev, I.V., 2007. Satellite remote sensing reveals regional tropospheric aerosol trends. Opt. Exp. 15, 7423–7438.

Mishchenko, M.I., Geogdzhayev, I.V., Rossow, W.B., Cairns, B., Carlson, B.E., Lacis, A.A., Liu, L., Travis, L.D., 2007. Long-term satellite record reveals likely recent aerosol trend. Science 315, 1543.

Moran, S.B., Moore, R.M., 1988. Temporal variations in dissolved and particulate aluminum during a spring bloom. Estuar. Coast. Shelf Sci. 27, 205–215.

Moulin, C., Lambert, C.E., Dayan, U., Masson, V., Ramonet, M., Bousquet, P., Legrand, M., Balkanski, Y.J., Guelle, W., Marticorena, B., Bergametti, G., Dulac, F., 1998. Satellite climatology of African dust transport in the Mediterranean atmosphere. J. Geophys. Res. 103, 13137–13144.

Niedermeier, N., Held, A., Müller, T., Heinold, B., Schepanski, K., Tegen, I., Kandler, K., Ebert, M., Weinbruch, S., Read, K., Lee, J., Fomba, K.W., Müller, K., Herrmann, H., Wiedensohler, A., 2014. Mass deposition fluxes of Saharan mineral dust to the tropical northeast Atlantic Ocean: an intercomparison of methods. Atmos. Chem. Phys. 14, 2245–2266.

Ohnemus, D.C., Lam, P.J., 2015. Cycling of Lithogenic Marine Particles in the US GEOTRACES North Atlantic Transect. Deep-Sea Res. II, 116, 283–302.

Orians, K.J., Bruland, K.W., 1986. The biogeochemistry of aluminum in the Pacific Ocean. Earth Planet. Sci. Lett. 78, 397–410.

Pey, J., Querol, X., Alastuey, A., Forastiere, F., Stofoggia, M., 2013. African dust outbreaks over the Mediterranean Basin during 2011–2011: PM10 concentrations, phenomenology and trends, and its relation with synoptic and mesoscale meteorology. Atmos. Chem. Phys. 13, 1395–1410.

Planquette, H., Sherrell, R.M., 2012. Sampling for particulate trace metal determination using water sampling bottles: methodology to in situ pumps. Limnol. Oceanogr. Methods 10, 367–388.

Prospero, J.M., Lamb, P.J., 2003. African droughts and dust transport to the Caribbean: Climate change implications. Science 302, 1024–1027.

Prospero, J.M., Mayol-Bracero, O.L., 2013. Understanding the transport and impact of African dust on the Caribbean basin. Bull. Amer. Meteor. Soc. 94, 1329–1337.

Prospero, J.M., Landing, W.M., Schultz, M., 2010. African dust deposition to Florida: Temporal and spatial variability and comparisons to models. J. Geophys. Res. 115, D13304.

Resing, J.A., C.I. Measures, C.I., 1994. Fluorometric determination of Al in seawater by FIA with in-line preconcentration. Anal. Chem. 66, 4105–4111.

Ridame, C., Guieu, C., Löye-Pilot, M.-D., 1999. Trend in total atmospheric deposition fluxes of aluminium, iron, and trace metals in the northwestern Mediterranean over the past decade (1985–1997). J. Geophys. Res. 104, 30127–30138.

Ryder, C.L., Highwood, E.J., Rosenberg, P.D., Trembath, J., Brooke, J.K., Dean, A., Crosier, J., Dorsey, J., Brindley, H., Banks, J., Marsham, J.H., McQuaid, J.B., Sodemann, H., Washington, R., 2013. Optical properties of Saharan dust aerosol and contribution form the coarse mode as measured during Fennec 2011 aircraft campaign. Atmos. Chem. Phys. 13, 303–325.

Schultz, M., Prospero, J.M., Baker, A.R., Dentener, F., Ickes, L., Liss, P.S., Mahowald, N.M., Nickovic, S, García-Pando, C.P., Rodríguez, S., Sarin, M., Tegen, I., Duce, R.A., 2012. Atmospheric transport and deposition of mineral dust to the ocean: Implications for research needs. Environ. Sci. Tech. 46, 10390–10404.

Tegen, I., Werner, M., Harrison, S.P., Kohfeld, K.E., 2004. Relative importance of climate and land use in determining present and future soil dust emission. Geophys. Res. Lett. 31, L05105.

Trossman, D.S., Thompson, L., Mecking, S., Warner, M.J., 2012. On the formation, ventilation, and erosion of mode waters in the North Atlantic and Southern Oceans. J. Geophys. Res. 117, C09026.

Twining, B.S., Rauschenberg, S., Morton, P.L., Ohnemus, D.C., Lam, P.J., 2015. Comparison of particulate trace element concentrations in the North Atlantic Ocean as determined with discrete bottle sampling and in situ pumping. Deep-Sea Res. II 116, 273–282.

Ussher, S.J., Achterberg, E.P., Powell, C., Baker, A.R., Jickells, T.D., Torres, R., Worsfold, P.J., 2013. Impact of atmospheric deposition on the contrasting iron biogeochemistry of the North and South Atlantic Ocean. Global Biogeochem. Cycles 27, 1096–1107.

van Hulten, M.M.P., Sterl, A., Tagliabue, A., Dutay, J.-C., Gehlen, M., de Baar, H.J.W., Middag, R., 2013. Aluminum in an ocean general circulation model compared with the West Atlantic Geotraces cruise. J. Mar. Sys. 126, 3–23.

Wedepohl, K.H., 2005. The composition of the continental crust. Geochim. Cosmochim. Acta 59, 1217–1232.

Wong, S., Dessler, A.E., Mahowald, N.M., Colarco, P.R., da Silva, A., 2008. Long-term variability in Saharan dust transport and its link to North Atlantic sea surface temperature. Geophys. Res. Lett. 35, L07812.

Woodward, S., Roberts, D.L., Betts, R.A., 2005. A simulation of the effect of climate change-induced desertification on mineral dust aerosol. Geophys. Res. Lett. 32, L18810.

Zender, C.S., Bian, H., Newman, D., 2003. Mineral Dust Entrainment and Deposition (DEAD) model: description and dust climatology. J. Geophys. Res. 104, 4416.

Zhang, J., Reid, J.S., 2010. A decadal regional and global trend analysis of the aerosol optical depth using a data assiilation grade over-water MODIS and Level 2 MISR aerosol products. Atmos. Chem. Phys. 10, 10949–10963.

Zhao, T.X.-P., Laszlo, I., Guo, W., Heidinger, A., Cao, A., Jelenak, A., Tarpley, D., Sullivan, J., 2008. Study of long-term trend in aerosol optical thickness observed from operational AVHRR satellite instrument. J. Geophys. Res. 113, D07201.

Table 3.1. Analysis (average ± 1 SD) of SAFe and GEOTRACES reference samples using the flow injection method of *Resing and Measures* [1994] for shipboard determination of dissolved Al (nmol L^{-1}) during the 2013 occupation of A16N compared to consensus values as of May 2013 (http://www.geotraces.org/science/intercalibration).

		A16N 2013	consensus
SAFe S	(n=8)	1.83 ± 0.05	1.67 ± 0.10
SAFe D1	(n=8)	1.01 ± 0.02	0.62 ± 0.03
SAFe D2	(n=8)	0.93 ± 0.04	1.03 ± 0.09
GEO GD	(n=7)	17.5 ± 0.4	17.7 ± 0.2
GEO GS	(n=4)	29.6 ± 1.3	27.5 ± 0.2

Table 3.2. Observed changes in trace metal concentrations between 2003 and 2013 reported in nmol L^{-1} and % change since 2003 and estimated residence time of the trace metal signal in regions of high aerosol dust inputs along A16N.

trace metal feature	latitude range	depth range	residence time	avg change 2003–2013 in nmol L^{-1} (%)
equatorial subsurface particulate Al	0–20°N	> 200 m	1–4 years	1.6 (+14%)
equatorial subsurface particulate Fe	0–20°N	> 200 m	1–4 years	0.9 (+27%)
equatorial surface dissolved Al	0–20°N	< 50 m	months	3.1 (+16%)
NA STMW[a] dissolved Al	25–35°N	150–450 m	4–20 years	1.0 (+5%)

[a]North Atlantic subtropical mode water

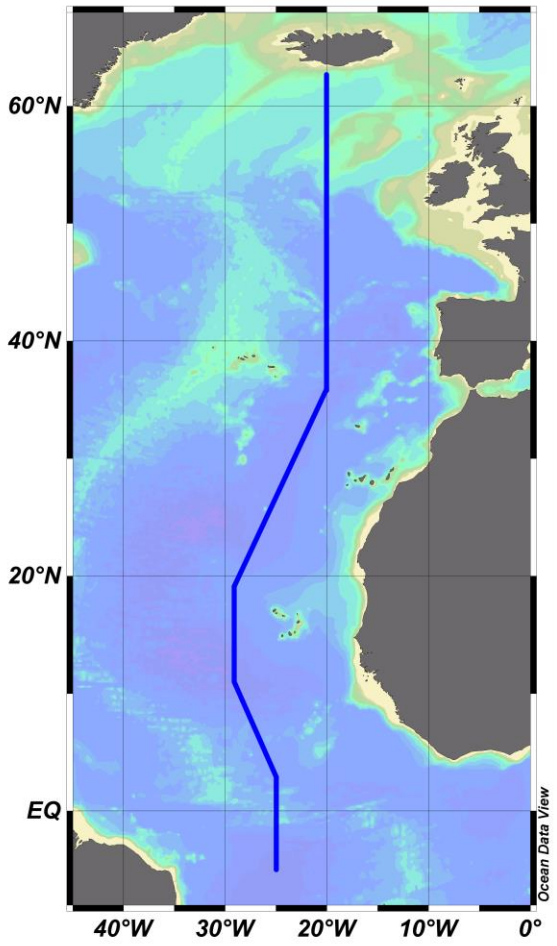

Figure 3.1. Map of the CLIVAR/CO_2 Repeat Hydrography section A16N occupied in 2003 and 2013.

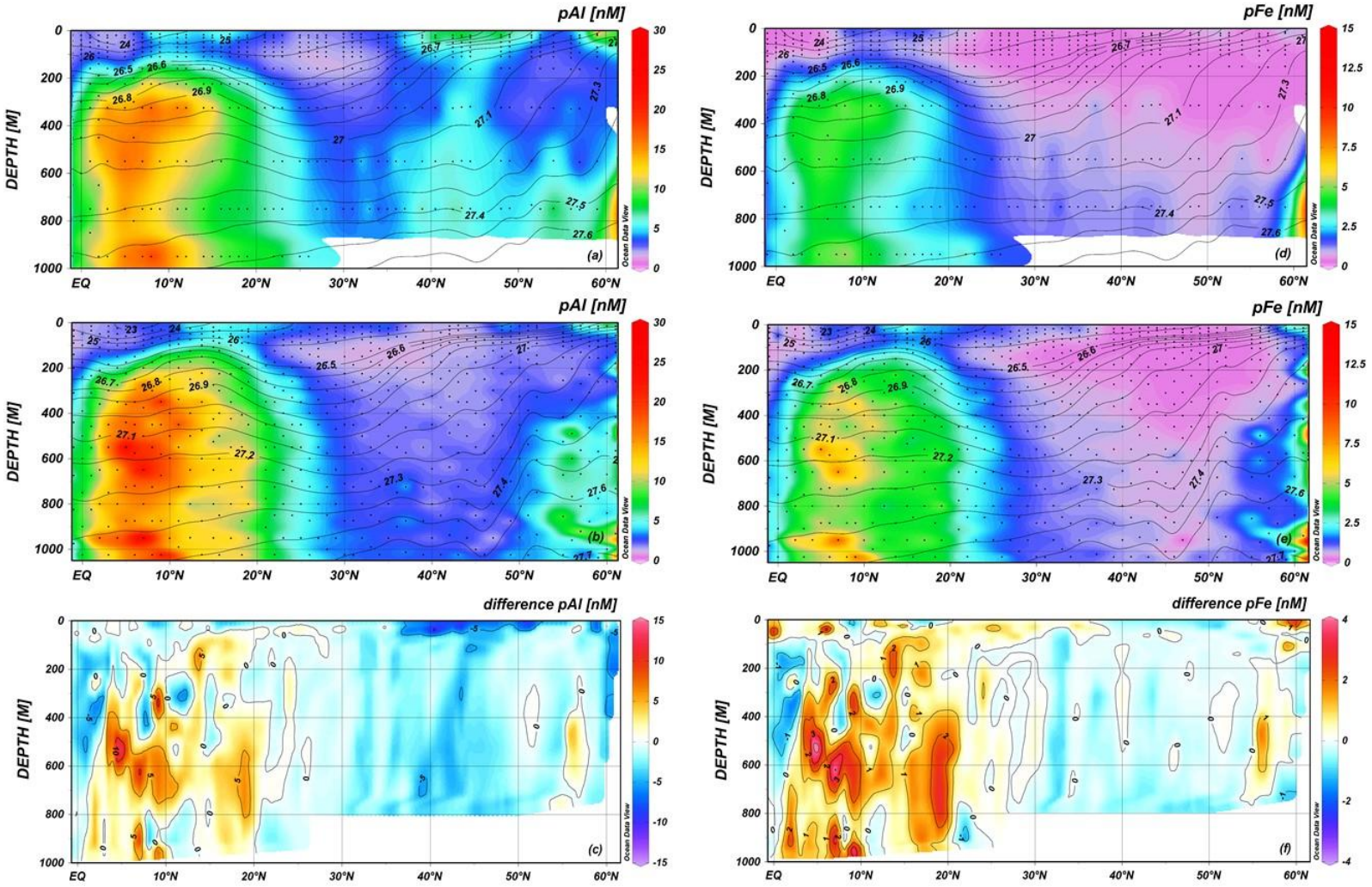

Figure 3.2. Distributions of particulate Al (a-c) and particulate Fe (d-f) in nmol L^{-1} along CLIVAR A16N in 2003 (a,d) and 2013 (b,e) with contours of potential density and the difference (2013 minus 2003) in particulate Al and Fe concentrations between the two occupations (c,f). Black dots represent individual sample measurements.

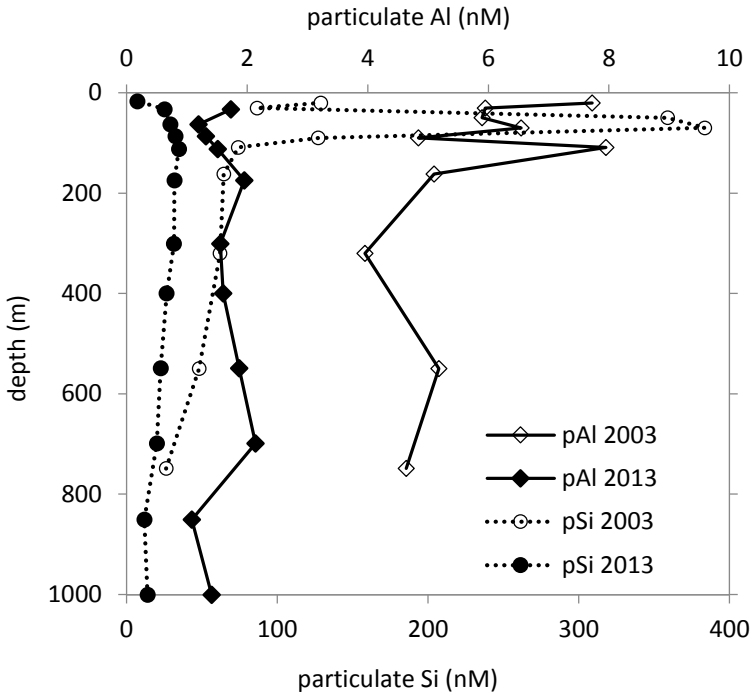

Figure 3.3. Concentrations (in nmol L^{-1}) of particulate Al (diamonds, solid line) and particulate Si (circles, dotted line) at 45°N along CLIVAR A16N in 2003 (station 42, open symbols) and 2013 (station 41, closed symbols).

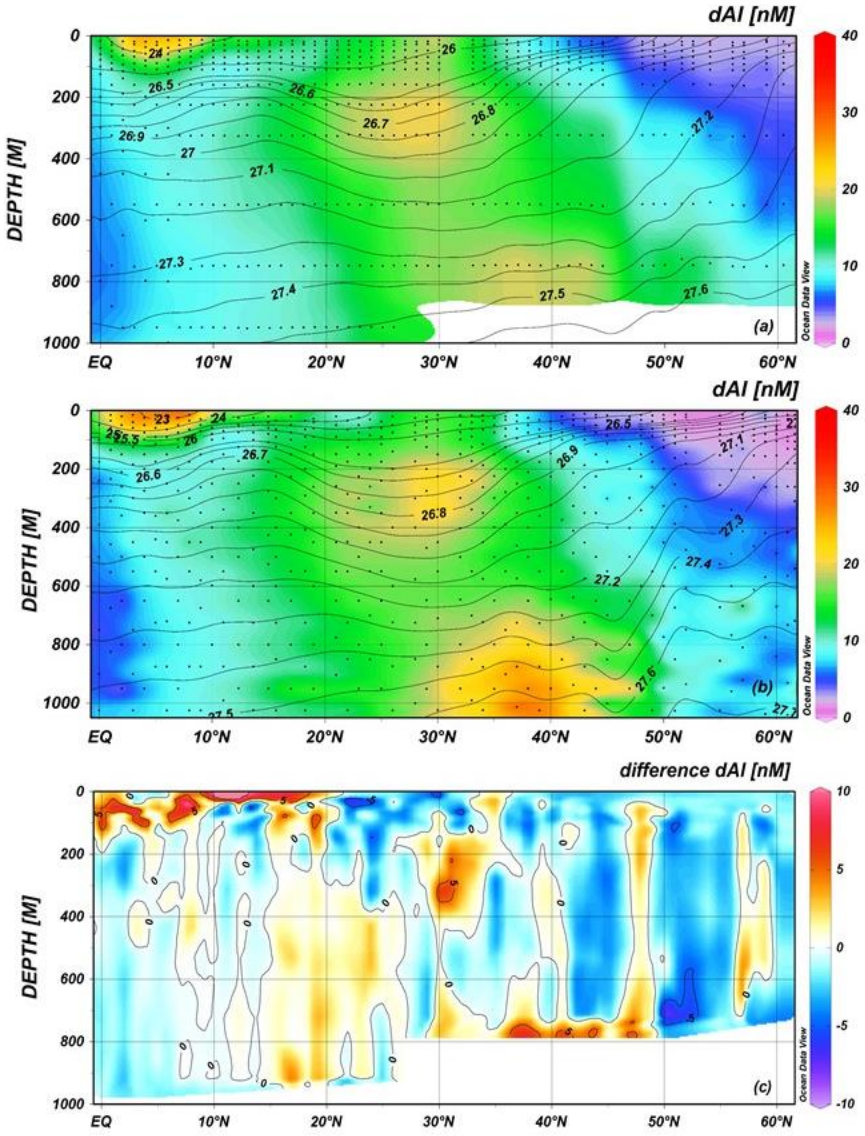

Figure 3.4. Distributions of dissolved Al in nmol L^{-1} along CLIVAR A16N in 2003 (a; *Measures et al*., 2008a) and 2013 (b; this work) with contours of potential density and the difference (2013 minus 2003) in dissolved Al concentrations between the two occupations (c). Black dots represent individual sample measurements.

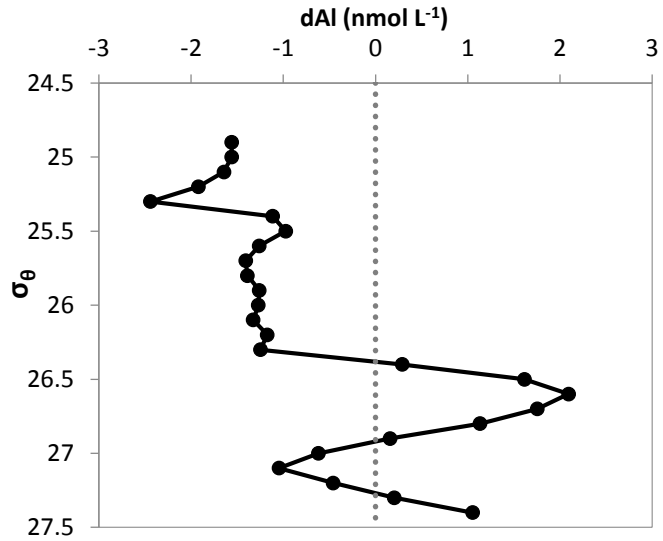

Figure 3.5. Difference (2013 minus 2003) in dissolved Al concentrations (in nmol L^{-1}) averaged over 25° to 35°N plotted as a function of potential density (σ_θ).

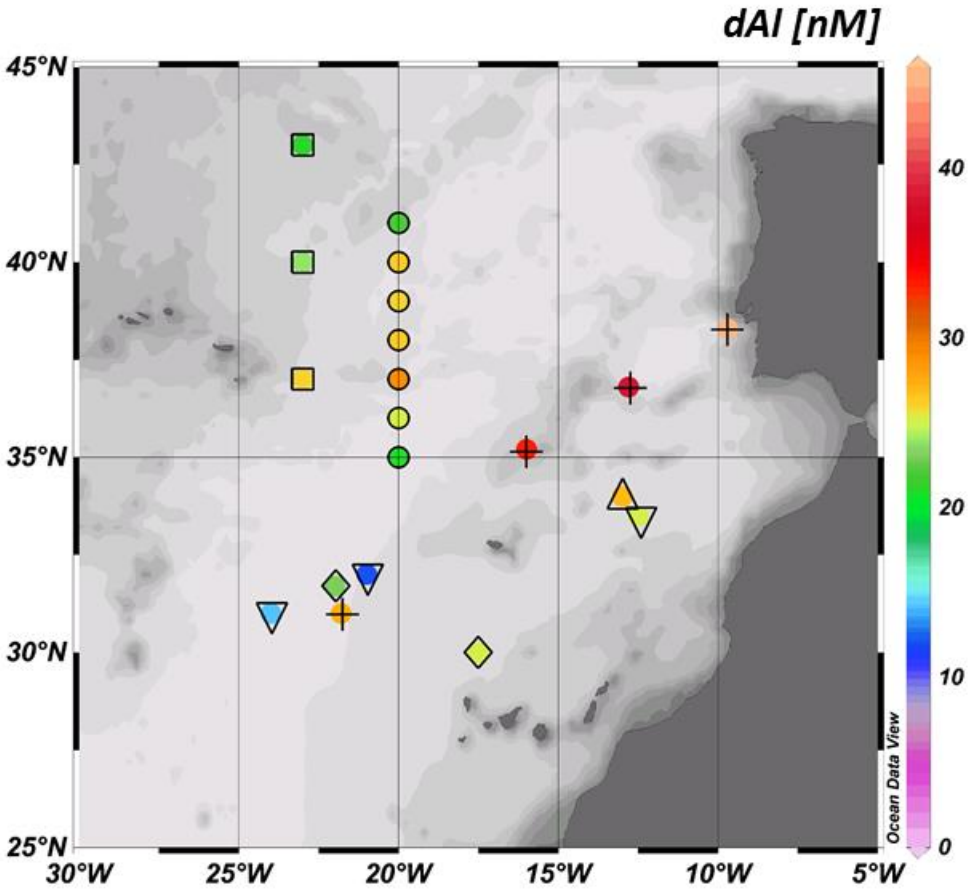

Figure 3.6. Maximum concentrations of dissolved Al (in nmol L^{-1}) in Mediterranean outflow water (MOW; 800–1300 m) from the 2013 CLIVAR A16N cruise (circles; this work), the 2010 GEOTRACES North Atlantic GA03 cruise (crosses) [*Measures et al*., 2014], the 2002 IRONAGES III cruise (diamonds) [*Kramer et al*., 2004], the 1998 MERLIM98 cruise (squares) [*de Jong et al*., 2007], the 1990 IOC Atlantic cruise (triangles) [*Measures*, 1995], and the 1982 RSS Discovery cruise 125 (inverted triangles) [*Hydes*, 1983].

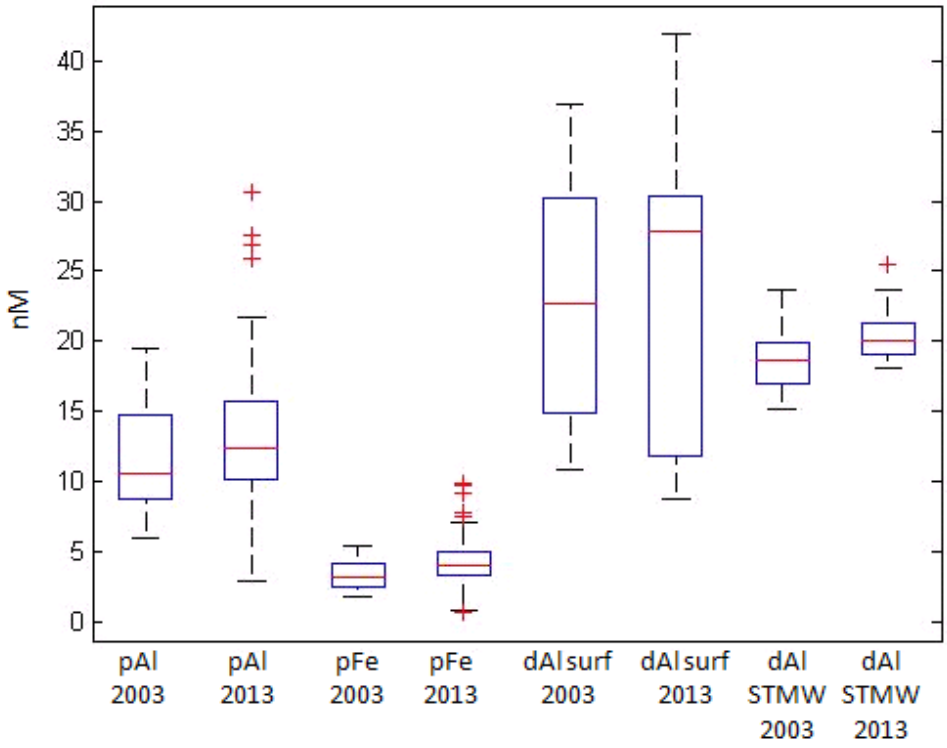

Figure 3.7. Observed concentrations (in nmol L^{-1}) of pAl and pFe in subsurface particulate plume (0-20°N, >200 m), dAl in surface waters (>50m, 0-20°N), and dAl within the core of North Atlantic subtropical mode waters (25-35°N, 150–450m). Box plots show median values (solid line), 50th percentile values (box outline), 95th percentile values (whiskers), and outlier values (crosses).

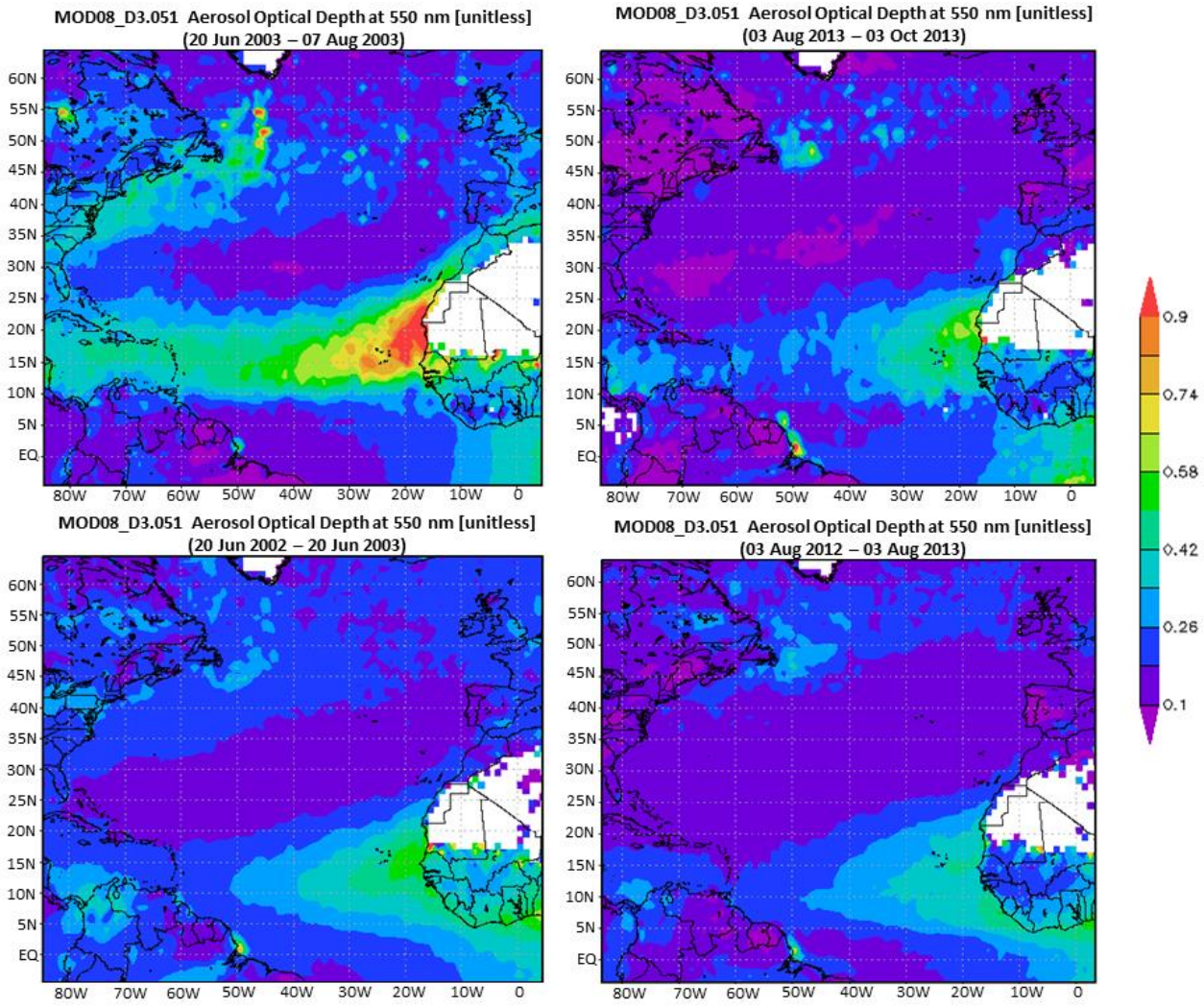

Figure 3.8. Aerosol optical depth at 550 nm from MODIS Terra Daily Level-3 Data temporally averaged over sampling dates (top) and 12 months prior to the cruise start (bottom) for the 2003 (left) and 2013 (right) occupations of A16N. Visualizations produced using the Giovanni online data system developed by NASA GES DISC (http://disc.sci.gsfc.nasa.gov/giovanni).

Chapter 4: $CaCO_3$ distributions and shallow-water dissolution estimates along A16N in 2003 and 2013

4.1 Introduction

Increasing atmospheric concentrations of anthropogenic CO_2 and subsequent uptake by the oceans has resulted in significant changes to the marine carbonate system, for example, increasing acidity in surface waters [*Caldeira and Wickett*, 2003; *Doney et al*., 2009] and shoaling of calcium carbonate ($CaCO_3$) saturation horizons [e.g., *Feely et al*., 2004]. The resulting dissolution of $CaCO_3$ can act as a buffering reaction facilitating increased oceanic uptake of anthropogenic CO_2:

$$CO_2 + CaCO_3 + H_2O \leftrightarrow 2HCO_3^- + Ca^{2+} \qquad (4.1)$$

On short timescales, further dissolution of upper-ocean $CaCO_3$ standing stocks will increase the ocean's absorption of anthropogenic CO_2 from the atmosphere. However, calcification by plankton supplies significant mineral ballast to sinking particles that facilitates the transport of organic carbon from the surface to the deep sea and ocean sediments [*Armstrong et al*., 2002 and references therein]. Increased $CaCO_3$ dissolution at shallow depths is likely to reduce the strength of the biological pump and the sequestration of CO_2 in the deep ocean [*Gehlen et al*., 2011]. Hence, changes in the rate of $CaCO_3$ dissolution in the upper ocean will be a significant feedback affecting atmospheric CO_2 concentrations and future climatic changes.

Biogenic $CaCO_3$ produced in the surface layer settles through the upper water column on relatively short timescales (days to weeks). Dissolution of $CaCO_3$ in the water column is dependent on the saturation state of water masses with respect to calcite and aragonite, the most common mineral morphotypes of $CaCO_3$. Conventionally, $CaCO_3$ would be expected to dissolve only at depth below the saturation horizon, although the assumption of the conservative nature of $CaCO_3$ in the upper water column has been increasingly challenged. Recent analyses suggest that considerable $CaCO_3$ dissolution may occur at depths of 500–1500 m [*Milliman et al*., 1999; *Schiebel*, 2002; *Berelson et al*., 2007; *Honjo et al*., 2008; *Lebrato et al*., 2010] in waters that are saturated with respect to aragonite and calcite, perhaps due to the dissolution of high-magnesium calcite [*Byrne et al.*, 1984; *Feely et al*., 1988; *Wilson et al*., 2009; *Lebrato et al*., 2010] or the formation of microenvironments conducive to $CaCO_3$ dissolution within suspended organic aggregates, fecal pellets, or zooplankton gut environments *[Bishop et al*., 1980; *Milliman et al*., 1999; *Jansen and Wolf-Gladrow*, 2001]. However, $CaCO_3$ dissolution at shallow depths is difficult to quantify. Assessments of $CaCO_3$ dissolution using shallow-water sediment trap data

are complicated by uncertainties associated with hydrodynamic and biological artifacts [*Berelson et al*., 2007; *Honjo et al*., 2008] and are limited by low spatial resolution in those studies. Examining changes in ocean alkalinity along isopycnal surfaces has also been used to estimate in situ $CaCO_3$ dissolution rates [*Feely et al*., 2002, 2004; *Sabine et al*., 2002; *Chung et al*., 2003]. However, this method may be complicated by uncertainties introduced by potential alkalinity fluxes from shelf environments [*Chen*, 2002] or vertical mixing and advective processes [*Friis et al*., 2006; 2007].

This study attempts to assess rates of in situ $CaCO_3$ dissolution at shallow depths in the North Atlantic Ocean (<1000 m) using a high-resolution dataset of suspended particulate calcium (pCa) distributions from small-volume, total suspended matter sampling carried out during the 2003 and 2013 occupations of the CLIVAR/CO_2 Repeat Hydrography A16N transect. The upper water column in the North Atlantic (<2500 m) is typically oversaturated with respect to both calcite and aragonite [*Chung et al*., 2003; *Feely et al*., 2004]. However, localized regions of aragonite undersaturation in intermediate water masses (600–1100 m) in the eastern tropical Atlantic have been described by *Chung et al*. [2004]. Furthermore, upper water column $CaCO_3$ dissolution may be facilitated by the non-thermodynamic mechanisms identified above, such as the formation of microenvironments in sinking organic aggregates. Using total suspended matter samples from the top 1000 m of the North Atlantic Ocean, the spatial extent and rate of $CaCO_3$ dissolution is inferred from the attenuation of the biogenic fraction of the suspended particulate Ca pool with depth. These $CaCO_3$ dissolution rates can then be compared to those estimated from changes in alkalinity along isopycnal surfaces, following the methods used in previous analysis of $CaCO_3$ dissolution rates in the Atlantic [*Chung et al*., 2003] and in similar studies carried out in the Pacific and Indian oceans [*Feely et al*., 2002, 2004; *Sabine et al*., 2002].

Total suspended matter sampling provides a snapshot view of particle distributions that complements sediment trap data while avoiding many of the possible biases introduced by trap collection. Although this approach may result in under-sampling of seasonal blooms of large, rapidly-sinking calcareous particles such as planktonic foraminifera tests, model results indicate that small plankton (<5 μm) dominate global $CaCO_3$ surface export [*Dunne et al*., 2012]. The relatively short residence times of calcareous particles in the upper ocean may be advantageous by reducing the effects of mixing and advective processes that potentially complicate interpretation of excess alkalinity distributions. Thus, high-resolution measurements of upper-ocean particulate calcium distributions may help constrain global budgets for water-column $CaCO_3$ dissolution.

4.2 Methods

4.2.1 Sample collection

Total suspended matter samples and carbon measurements used in this study were collected along the CLIVAR/CO_2 Repeat Hydrography A16N transect from Reykjavik, Iceland to Natal, Brazil between 20 June and 7 August 2003 and 3 August to 3 October 2013. Hydrographic and CO_2-parameter sampling was carried out at approximately 150 stations with half-degree spacing. Total suspended matter samples were collected at approximately 60 stations with approximately 1° spacing by subsampling seawater collected using 12 L GO-FLO bottles on a trace metal-clean rosette from the surface to 750–1000 m (see *Measures et al*. [2008a] for details). Suspended particulate matter samples were collected by pressure-filtering seawater through acid-cleaned, 0.4 μm Nuclepore polycarbonate filters with backing filters of mixed cellulose esters to ensure even particle loading across the sample filter. To remove residual sea salt, sample filters were rinsed with 15–20 mL pH 8 DI water (adjusted with ammonium hydroxide) while on the filter holder with a low vacuum applied to avoid loss or re-distribution of particles [*Feely et al*., 1991]. The average sample filtration volume was 8 L. Particle settling in the bottom of GO-FLO bottles can potentially underestimate trace element concentrations [*Planquette and Sherrell*, 2012]. To minimize this effect, filtration was started approximately 30–60 minutes after water sample collection and generally completed within 60 minutes and whole-bottle filtrations were done whenever possible. This potential loss term is difficult to quantify, but could lead to underestimation of $CaCO_3$ concentrations, particularly in surface waters where large particles are expected to be most abundant. In 2013, GO-FLOs were fitted with Teflon tubing attached to the interior of the stopcock. However, as discussed in section 3.2.1, there is no evidence of sampling artifacts introduced by this modification.

4.2.2 Analytical methods

The elemental composition of total suspended matter samples was determined by energy-dispersive X-ray fluorescence (ED-XRF) under a vacuum atmosphere using thin film principles as described by *Barrett et al*. [2012] following the methods of *Feely et al*. [1991]. Sample filters were analyzed on a Thermo Fisher Quant'X equipped with a Rhodium Target X-Ray tube and an electronically cooled, lithium-drifted solid state detector. X-rays for primary sample excitation were passed through graphite filters for optimum control of peak-to-background ratios.

ED-XRF calibration was performed using commercial thin film standards (MicroMatter). Signal intensity is linear with increasing concentrations and all samples fell within the range of the standard curve for elements of interest. The minimum determination limit (MDL) is defined as follows:

$$\mathrm{MDL} = 3 \cdot c \cdot \sqrt{I_b} \,/\, I_p \qquad (4.2)$$

where I_b is the background intensity, I_p is the peak intensity, and c is the concentration of the standard. MicroMatter standards were used to calculate MDLs. The MDLs for in situ seawater concentrations of particulate calcium and aluminum were 0.15 nM and 0.54 nM, respectively, for the average sample filtration volume of 8 L. Na concentrations confirm the efficacy of the rinsing procedure in removal of residual sea salt.

Analytical accuracy of the ED-XRF analysis was confirmed by analysis of NIST certified reference material SRM 2783, air particulate on filter media, which showed good agreement between certified and measured values for Ca [*Barrett et al*., 2012], with ED-XRF values within ± 1 standard deviation of the certified value.

4.2.3 Calculation methods for $CaCO_3$ saturation state and $CaCO_3$ dissolution estimates

Measurements of CO_2-parameters collected along CLIVAR A16N are described in detail in *Peltola et al*. [2005] and *Baringer and Bullister* [2014]. Total dissolved inorganic carbon (DIC) was determined by coulometry [*Johnson et al*., 1993] and total alkalinity (TA) was determined by titration [*Millero et al*., 1993]. CFC concentrations were determined based on methods described by *Bullister and Weiss* [1988].

The saturation state of seawater with respect to aragonite and calcite is calculated for the top 1000 m of the water column from 62°N to 5°S. Saturation states for aragonite (Ω_{arg}) and calcite (Ω_{cal}) are defined as follows:

$$\Omega_{arg} = [Ca^{2+}][CO_3^{2-}] / K_{sp\text{-}arg} \qquad (4.3)$$

$$\Omega_{cal} = [Ca^{2+}][CO_3^{2-}] / K_{sp\text{-}cal} \qquad (4.4)$$

where $[Ca^{2+}]$ and $[CO_3^{2-}]$ are the in situ calcium and carbonate ion concentrations, respectively, and K_{sp} is the stoichiometric solubility product. Saturation state calculations were performed using the CO_2sys program developed by *Lewis and Wallace* [1998]. The Ca^{2+} concentration is estimated from salinity;

small variations in Ca with salinity [*Millero*, 2006] have negligible effect on the saturation state calculation. Carbonate ion concentrations are calculated from measured TA and DIC. Dissociation constants for carbonic acid are taken from *Mehrbach et al*. [1973] as refitted by *Dickson and Millero* [1987], and pressure effects are accounted for using the formulations of *Millero* [1995]. Values for $K_{sp\text{-}arg}$ and $K_{sp\text{-}cal}$ are taken from *Mucci* [1983]; pressure effects on solubilities are estimated based on the work of *Ingle* [1975]. We also calculate the seawater saturation state with respect to a high-Mg calcite produced by fish, as recent work has suggested that highly soluble, fish-produced carbonates may represent a significant portion of oceanic carbonate production *[Wilson et al*., 2009]. The solubility for high-Mg calcite is taken from the experimental work of *Woolsey et al*. [2012], which found fish-produced $CaCO_3$ (48 mol % Mg) to be 1.9 times more soluble than aragonite.

Dissolution of $CaCO_3$ within water masses can be estimated by determining the residual alkalinity change after removing preformed alkalinity from total measured alkalinity concentrations and compensating for alkalinity decreases due to respiration of organic matter, an approach that has been employed in previous analyses [e.g., *Brewer et al*., 1975; *Chen*, 1978; *Chung et al*., 2003; *Feely et al*., 2004]. This excess alkalinity due to $CaCO_3$ dissolution is defined as TA*:

$$TA^* = 0.5(TA - TA^\circ) + 0.0593 \cdot AOU \qquad (4.5)$$

where TA° is the preformed alkalinity and AOU is apparent oxygen utilization. The oxidation of organic matter is accounted for using AOU and the N/O_2 ratio of *Anderson and Sarmiento* [1994] (0.0941) combined with a coefficient of 0.63, as proposed by *Kanamori and Ikegami* [1982] to include alkalinity changes resulting from the oxidation of organic nitrogen, phosphorus, and sulfur. The preformed TA° estimates alkalinity of water masses when last at the surface, which for some water masses represented along the A16N transect, may be at outcrops in the South Atlantic (see discussion in section 4.3.3). Thus, a multilinear regression to estimate TA° was derived using conservative tracers S and NO and surface alkalinity data (<100 m) from both the A16N and A16S transects [*Wanninkhof et al*., 2010] (**Appendix, Figure B.1**):

$$TA^\circ\,(\mu mol\ kg^{-1}) = 250.7 + 57.8 \cdot S + 0.12 \cdot NO \qquad (4.6)$$

where *S* is salinity and $NO = O_2 - R_{O2/N} * NO_3$ [*Broecker*, 1974], using a value of -10.625 for $R_{O2/N}$ [*Anderson and Sarmiento*, 1994]. When the standard error for TA° estimates from this regression fit (8.4 μmol kg^{-1})

is combined with reported errors of ± 0.0218 for the O_2/N ratio [*Anderson and Sarmiento*, 1994] and ± 3.6 µmol kg^{-1} for measured TA [*Peltola et al*., 2005], the error in TA* estimates is ± 4.6 µmol kg^{-1}.

Values of TA* and CFC-derived ages of the water masses [Doney and Bullister, 1992] are used to calculate rates of in situ $CaCO_3$ dissolution [*Feely et al*., 2002; *Sabine et al*., 2002; *Chung et al*., 2003]. The use of CFC-derived ages is restricted to water masses with CFC ages of less than 35 years to limit the introduction of error due to age biases from dilution and mixing in older, deeper waters**.** The average $CaCO_3$ dissolution rate along a given isopycnal surface is determined from the slope obtained by plotting TA* versus apparent CFC-12 ages.

4.3 Results and discussion

First, using the 2003 A16N data, we describe the general trends in carbonate saturation state, biogenic $CaCO_3$, and TA* distributions and compare upper-water column dissolution estimates derived from two independent approaches [*Barrett et al*., 2014]. In section 4.3.6, we examine the distribution of biogenic $CaCO_3$ observed along the same section a decade later and discuss how observed changes may be related to both variability in productivity and CO_2 chemistry in the upper water column.

4.3.1 $CaCO_3$ saturation state

The seawater saturation state (Ω) with respect to aragonite, calcite, and high-Mg calcite is shown in **Fig. 4.1**. Surface waters in the North Atlantic were oversaturated with respect to calcite by a factor of 4–6, by a factor of 2.5–4 with respect to aragonite, and by a factor of 1.4–2 with respect to high-Mg calcite. The degree of saturation generally decreases with depth due to increasing solubility of $CaCO_3$ with decreasing temperature and increasing pressure. The saturation horizon (Ω = 1) indicates the depth at which $CaCO_3$ is in thermodynamic equilibrium, while at Ω<1, net dissolution of $CaCO_3$ is expected to occur. The saturation horizon for aragonite varied along the transect, ranging from 350 m to >1000 m. In mid-latitudes (20–60°N), the entire water column above 1000 m was oversaturated with respect to aragonite. This is consistent with previous studies that have determined aragonite-saturation depths at these latitudes to be 2500–3000 m [*Chung et al*., 2003; *Feely et al*., 2004]. At low latitudes, a large region of aragonite-undersaturated water was found between 5°S and 17°N at relatively shallow depths (<400–1000 m). This is consistent with the findings of *Chung et al.* [2004], who, using data from the Atlantic compiled over 1990–1998, reported isolated layers of aragonite undersaturation in intermediate waters (centered at ~800 m) between 16°S and 14°N along 20°W in the eastern tropical Atlantic.

Trends in saturation state with respect to calcite follow similar patterns to those seen for aragonite. However, because calcite has a lower solubility than aragonite, a given saturation horizon for calcite was found deeper in the water column when compared to the same saturation horizon for aragonite. Minimum values for calcite saturation state were found below 400 m at low latitudes (0–15°N), although the degree of saturation for calcite approached (1.3) but did not reach the saturation horizon in the top 1000 m. The saturation horizon for high-Mg calcite was found between 250 and 500 m in the northern section of the transect and shoaled to 75–150 m at low latitudes.

4.3.2 Distribution of biogenic $CaCO_3$

Particulate Ca in suspended matter samples originates from both biogenic and lithogenic sources. While pCa concentrations in the upper water column primarily reflect biological production of $CaCO_3$, lithogenic inputs are potentially significant at some locations. For example, intense deposition of Saharan mineral dust on the surface ocean in the tropical North Atlantic may influence upper water column pCa concentrations. To isolate the biogenic $CaCO_3$ signal, pCa concentrations are normalized to particulate Al, which serves as a proxy for lithogenic particle inputs. The biogenic fraction, pCa_B, is calculated using measured particulate Ca and Al concentrations, pCa_M and pAl_M, respectively, and the average crustal Ca:Al molar ratio (0.33) [*Wedepohl*, 1995].

$$\mathrm{pCa_B} = \mathrm{pCa_M} - (\mathrm{Ca{:}Al})_{crustal} \cdot \mathrm{pAl_M} \qquad (4.7)$$

Based on equation 4.7, lithogenic inputs are a minor component of observed pCa distributions along A16N with maximum concentrations of 6 nM in the top 1000 m. In the upper 100 m, pCa_B accounts for an average of 96% of pCa concentrations.

Estimated error in calculated pCa_B values is small (<10%), but may arise from assumptions about the composition of lithogenic inputs or water-column pAl concentrations. Daily-integrated aerosol samples collected within the Saharan dust plume along A16N were found to have Ca:Al ratios 2–3 times higher than the average crustal ratio [*C.S. Buck*, unpublished data]. Similar aerosol Ca enrichment has been reported for mineral dust originating in the north Sahara where soils are rich in calcite [*Schütz and Sebert*, 1987; *Chiapello et al*., 1997]. While we are unable to determine the source regions for our aerosol samples, it is possible that they are not representative of long-term aerosol composition as aerosol uplift and transport are highly variable both temporally and spatially. Previous studies have found Ca:Al ratios in Saharan aerosols close to the average crustal value [*Formenti et al*., 2003]. Hence,

average crustal Ca:Al ratio was used in equation 4.7 to account for lithogenic pCa. Error in the pCa_B distribution could also result from water column scavenging of dissolved Al in the mid-latitude surface ocean following seasonal phytoplankton blooms [*Barrett et al*., 2012], which would increase pAl concentrations and underestimate pCa_B. Re-evaluating equation 4.7 with pAl concentrations 5 times lower than observed and a Ca:Al ratio 3 times the crustal ratio are used to constrain the upper and lower limits, respectively, on pCa_B concentrations (**Fig. 4.2**), which indicate that these potential errors in calculated pCa_B concentrations are small (<10%).

Biogenic pCa is assumed to be dominated by $CaCO_3$. However, previous work has suggested that a non-carbonate, "excess particulate Ca" fraction is associated with cytoplasmic organic matter, although the exact form or speciation of this pool is unknown [*Bishop et al*., 1977]. To assess potential effects of non-carbonate pCa, the organic pCa signal in our samples was estimated using measured particulate P concentrations as a proxy for particulate organic matter, a C:P organic matter ratio of 106:1, and a C:Ca for organic particulate matter of 160:1 [*Mayzaud and Martin*, 1975; *Bishop et al*., 1977]. Using this approximation, we find pCa associated with organic matter would account for an average of <3% of biogenic pCa. The effect is slightly more important in the euphotic zone where the concentration of particulate organic matter is highest, but is still <5% of biogenic pCa in the upper 100 m. Hence, we conclude the contribution from organic pCa in our samples is likely very minor with minimal impact on $CaCO_3$ dissolution rate estimates.

The distribution of pCa_B is shown in **Fig. 4.3**. High pCa_B concentrations (> 1.1 µmol L^{-1}) are found in coastal waters off southern Iceland. In the mid-latitudes (45–60°N), elevated pCa_B concentrations, largely reflecting seasonal coccolithophore blooms, range from 50 to 250 nmol L^{-1} in the surface ocean. Lower pCa_B concentrations (~10–75 nmol L^{-1}) are observed through surface waters of the oligotrophic subtropical gyre, while increased productivity stimulated by upwelling at the equator is reflected in higher pCa_B up to 150 nmol L^{-1}. Euphotic-zone pCa_B concentrations from open-ocean stations in this dataset are plotted in **Fig. 4.2** with previously reported values for surface-ocean $CaCO_3$ in the North Atlantic [*Bishop*, 1989; *Poulton et al*., 2006]. Some differences at mid- and high latitude stations may be attributable to interannual variability in the timing and magnitude of the spring bloom in the North Atlantic. In the tropical Atlantic, pCa_B concentrations are lower than previous measurements of euphotic zone particulate inorganic carbon made by *Poulton et al*. [2006] using similar sampling techniques. Interannual variability in $CaCO_3$ production may contribute to differences in surface-ocean $CaCO_3$ standing stocks in low latitude regions. Aerosol Ca deposition as estimated from equation 4.7 could account for 10–20% of the observed differences between studies. Differences in water-column

integration depths between studies may also result in some apparent variability. Low euphotic zone $CaCO_3$ concentrations in this study would lead to underestimation of the dissolution rates discussed in **section 4.4.1**.

A striking feature in the subsurface distribution of pCa_B occurs between approximately 5 and 25°N where pCa_B concentrations decrease significantly below ~400 m. In the upper ocean (<200 m) at these latitudes, pCa_B concentrations average 26 $\pm$ 13 nmol L^{-1} while at depths greater than 400 m, average values drop to 13 $\pm$ 5 nmol L^{-1}, a decrease of 50%. By contrast, at stations between 30 and 55°N, pCa_B decreases by only 13% in the top 1000 m, from an average concentration of 41 $\pm$ 31 nmol L^{-1}in the upper ocean to 36 $\pm$ 10 nmol L^{-1} below 400 m.

Attenuation of the pCa_B signal with depth is interpreted to be due largely to the dissolution of $CaCO_3$. The region of apparent deficit in pCa_B largely overlaps the region of aragonite undersaturation and low calcite saturation state discussed above, suggesting that thermodynamically-predicted water column saturation state leads to $CaCO_3$ dissolution. Additionally, the local oxygen minimum zone (200 – 800 m) in the eastern North Atlantic [*Stramma et al*., 2008] and high subsurface concentrations of dissolved Fe observed along this transect at low latitudes [*Measures et al*., 2008b] demonstrate that biogenic particles are subject to significant remineralization in intermediate waters in this region. Intense local remineralization processes would indicate potential for considerable biologically-mediated $CaCO_3$ dissolution within particles as proposed by *Milliman et al.* [1999].

However, the distribution of $CaCO_3$ is also subject to dynamic aggregation, rapid sinking, and disaggregation processes, which are considered here as potentially contributing to the apparent deficit of $CaCO_3$ at depth. The vertical structure of particulate trace metals profiles (Al, Fe) at low-latitude A16N stations [*Barrett et al*., 2012] indicates that biologically-mediated aggregation and rapid vertical transport of particles occurs in near-surface waters at the depth of the fluorescence maximum (50–100 m). Incorporation of biogenic $CaCO_3$ into dense, rapidly-sinking aggregates at depths of high biological activity likely also explains lower $CaCO_3$ concentrations above ~75 m in low-latitude waters. We must consider that such aggregation and removal of $CaCO_3$ could also lead to the decrease in $CaCO_3$ concentrations below 400 m at low latitudes, as invoked in *Sherrell et al*. [1998] to explain mid-depth minima in suspended Ca in the NE Pacific. However, particle degradation and disaggregation processes are important in sustaining intense subsurface “plumes” of high concentrations of suspended particulate trace metals at depths of 150–1000 m in low-latitudes along this transect [*Barrett et al*., 2012]. Sediment trap studies have demonstrated that biogenic and lithogenic particle fluxes are closely coupled

in this region [*Bory and Newton*, 2000], suggesting that the distribution of calcareous particles in this region would be similarly dominated by degradation and disaggregation processes.

*4.3.3. Distribution of TA**

The distribution of TA* along the 2003 A16N section is shown in **Fig. 4.4**. The TA* distribution is similar to that determined by *Chung et al*. [2003] for the upper water column in the North Atlantic using data from 1990 to 1998. The size of the TA* signal is small compared to the uncertainly in the TA* estimate (+ 4.6 μmol kg^{-1}), although this large uncertainty is primarily due to error in the intercept of the multi-linear regression used to approximate TA° (equation 4.6) rather than the relationship of TA with conservative tracers S and NO.

The general increase in TA* concentrations with depth is attributable to accumulation of alkalinity from the in situ dissolution of $CaCO_3$ [*Feely et al*., 2002; *Sabine et al*., 2002; *Chung et al*., 2003]. The highest concentrations of TA* along the transect are found in subsurface waters in the (sub)tropical North Atlantic. The deep maximum in TA* centered at the equator is associated with the northern extension of Antarctic Intermediate Water (AAIW), which can be seen in the salinity minimum in this region (**Fig. 4.5**) [*Stramma et al*., 2005; *Wanninkhof et al*., 2010]. The TA* signal in this water mass represents slow accumulation of alkalinity in the AAIW due to $CaCO_3$ dissolution during the transit from its outcrop in the South Atlantic (45°S) [*Chung et al*., 2003; *Wanninkhof et al*., 2010]. In the region of significant pCa_B attenuation centered at ~10°N, a secondary TA* maximum is observed as TA* concentrations increase with depth below ~200 m. These high TA* values coincide with the location of pCa_B deficits and carbonate undersaturation and this signal is likely largely due to dissolution of settling $CaCO_3$ from overlying high-productivity surface waters.

Alkalinity fluxes from shelf environments have also been suggested to contribute to open-ocean subsurface TA* concentrations [*Chen*, 2002], although this source was not quantified in previous studies in the Atlantic due to uncertainty about the lateral extent of shelf waters [*Chung et al*., 2003]. To estimate the contribution of shelf carbonate dissolution, we have calculated TA* based on CO_2-parameter measurements from WOCE zonal transect A06 (http://cdiac.ornl.gov/oceans/woce_a06.html) along 8°N, which intersects the core of the high-dissolution region. This analysis reveals that alkalinity fluxes originating from the shelf and slope of the eastern side of the Atlantic basin are restricted to waters within 500 km of the coast and are spatially distinct from elevated subsurface TA* within the study area (**Appendix, Figure B.2**). Hence, excess

alkalinity laterally advected from shelf environments is likely not an important mechanism for TA* accumulation in our study area.

Estimates of $CaCO_3$ dissolution rates were calculated using TA* concentrations and apparent CFC-12 ages for two regions. North of 30°N, pCa_B is relatively constant with depth and TA* concentrations in the upper 1000 m are relatively low. In contrast, between the equator and 30°N, significant attenuation of the pCa_B signal is apparent at depths below 400 m and TA* concentrations are higher due to dissolution of biogenic $CaCO_3$ as it sinks through the water column. By combining slope calculations for TA* v. CFC-age relationships along individual isopycnals (**Appendix, Figure B.3**), depth-integrated dissolution rates (200–1000 m) are calculated for these two regions and are reported in **Table 4.1**. The TA*-derived $CaCO_3$ dissolution rate is estimated to be 0.5 mmol $CaCO_3$ m^2 d^{-1} for the northern region and 0.7 mmol $CaCO_3$ m^2 d^{-1} in low latitudes. Like previously reported dissolution estimates from the upper water column in the North Atlantic [*Chung et al*., 2003], these rates rely on a TA* signal generally smaller than the magnitude of the uncertainty in the TA* estimate and hence are not significant. However, because this approach has been used to arrive at most recent estimates of upper-ocean $CaCO_3$ dissolution [*Berelson et al*., 2007], we attempt to apply the TA* approach in efforts to provide some comparison for the dissolution rates we estimate from pCa distributions along this transect.

4.3.4 $CaCO_3$ dissolution rate estimates

The attenuation of pCa_B between the surface layer (<200 m) and depth can be quantified and combined with an average turnover time for $CaCO_3$ in the euphotic zone to estimate annual $CaCO_3$ dissolution between the surface ocean and 1000 m as shown below:

$$CaCO_3 \text{ dissolution} = t^{-1} \cdot \Delta(pCa_B) \cdot d \qquad (4.8)$$

where *t* represents the average turnover time for $CaCO_3$ in the euphotic zone, *d* is the water column integration depth (800 m), and $\Delta(pCa_B)$ is the change in average pCa_B concentration between the surface layer (0–200 m) and depth (200–1000 m). Estimates for euphotic zone $CaCO_3$ turnover times range from 5–18 days globally [*Berelson et al*., 2007] and 3–10 days in the Atlantic [*Balch and Kilpatrick*, 1996; *Poulton et al*., 2006]. Using an average turnover time of 10 days is likely accurate to a factor of 2. Standing stocks of $CaCO_3$ in the (sub)tropical North Atlantic can be approximated as steady-state, given the relatively small seasonal variation in productivity. Hence, potential scaling errors introduced by using

turnover times to extrapolate $CaCO_3$ standing stocks to annual production rates should not be significant in this region. However, calculations using observed standing stocks in the northern section of the transect may lead to significant errors in annual $CaCO_3$ dissolution as euphotic zone $CaCO_3$ inventories in the mid- and northern latitudes of the North Atlantic are highly seasonally variable [*Balch*, 2005] and sampling of the A16N transect occurred shortly after the 2003 spring bloom at these latitudes [*Henson et al.*, 2009].

$CaCO_3$ dissolution estimated from both pCa_B and TA* distributions is presented in **Table 4.1** with previously reported dissolution rates for the Atlantic and other basins from *Feely et al.* [2004] as summarized in *Berelson et al*. [2007]. Dissolution rates from TA* in this study were calculated from TA* values generally smaller than the estimated error ($\pm$ 4.6 µmol kg^{-1}), but are presented for comparison purposes. Dissolution rates calculated from pCa_B distributions indicate higher $CaCO_3$ dissolution at low latitudes in the region of aragonite-undersaturated waters (0.9 mmol $CaCO_3$ m^{-2} d^{-1}) compared to the mid- and high latitudes (0.2 mmol $CaCO_3$ m^{-2} d^{-1}) along A16N. Estimates from the TA* distribution are also consistent with this trend. $CaCO_3$ dissolution rates estimated in this study for intermediate waters in the eastern tropical North Atlantic indicate this region is a 'hotspot' for upper water column $CaCO_3$ dissolution compared to the basin as a whole, with rates comparable to those observed in the Pacific or Indian oceans.

4.3.5. Possible mechanisms for observed in situ $CaCO_3$ dissolution in (sub)tropical waters

Overlap between regions of both aragonite and high-Mg calcite undersaturation, high TA* concentrations, and pCa_B deficits in intermediate waters at low latitudes suggests that $CaCO_3$ dissolution in the upper water column can be partially attributed to thermodynamically-predicted water-column saturation state. High subsurface DIC concentrations, coinciding with maxima in apparent oxygen utilization (AOU), are found in the eastern Atlantic basin at low latitudes as a result of local water-column respiration processes [*Chung et al*., 2004; *Wanninkhof et al*., 2010] and sluggish ventilation of the "shadow zone" in the eastern tropical Atlantic [*Karstensen et al.,* 2008]. The high concentrations of DIC (>2225 µmol kg^{-1}) and low pH (< 7.75) observed in this region during the 2003 A16N transect (**Fig. 4.6**) are characteristic features of this subsurface water mass [*Paulmier et al*., 2011] and result in intermediate waters that are corrosive to $CaCO_3$.

Biological processes may also facilitate carbonate dissolution between 400 and 1000 m. For example, if all of the observed decline in pCa_B concentrations below 400 m was due to aragonite (pteropod) dissolution, then that would require that aragonite represent ~50% of the $CaCO_3$ surface

standing stock in the low-latitude region. Globally, the relative contribution of aragonite to $CaCO_3$ production in the surface ocean has been estimated to be 10 to 15% [*Berner and Honjo*, 1981; *Fabry and Deuser*, 1991] with the highest pteropod biomass found in high-latitude and coastal regions [*Bednaršek et al*., 2012]. Unfortunately, spatial coverage of pteropod biomass data is poor for our low-latitude study area [*Bednaršek et al*., 2012]. Hence, we must consider the possibility that biologically-mediated dissolution of calcite is a control on pCa_B distributions in the top 1000 m in the North Atlantic.

Another biological process we consider is the presence and dissolution of fish-derived high Mg-calcite. Although the saturation horizon for high-Mg calcite (48 mol %) [*Woolsey et al*., 2012] is found at depths of ~100 m in low latitudes (**Fig. 4.1**), no robust attenuation of the pCa_B signal is apparent above ~400 m that could be attributed to the dissolution of high-Mg calcites. This could be a function of the relatively small decreases expected in pCa_B concentrations (<5 nmol L^{-1}) even for maximum high-Mg calcite production estimates (15% of global carbonate production) [*Wilson et al*., 2009]. However, it is not apparent from our dataset if the dissolution of high-Mg calcites contributes significantly to carbonate dissolution in our study area.

4.3.6 Comparison of 2003 and 2013 observations

The seawater saturation state (Ω) with respect to aragonite and calcite along A16N in 2003 and 2013 is shown in **Figure 4.7**. The depth of the aragonite saturation horizon in the low-latitude study region is sufficiently shallow to be affected by the invasion of anthropogenic CO_2 into the surface ocean [*Chung et al*., 2004; *Sabine et al*. 2004]. In general, we observe a slight expansion of corrosive waters undersaturated with respect to aragonite at intermediate depths in the (sub)tropical region. The average decrease in aragonite saturation state is 4.2%, which is similar to the rates of saturation state decline in the upper water column in the Atlantic and Pacific basins since the 1990s reported by previous studies [*Feely et al*., 2012; *Jiang et al*., 2015].

The distribution of pCa_B along the 2013 A16N transect is shown in **Figure 4.8**. Based on equation 4.7, both lithogenic and organic pCa are relatively minor components of total pCa concentrations, which are dominated by biological production of $CaCO_3$, similar to findings in 2003 (**Table 4.2**). The major features in the 2013 pCa_B distribution are similar to trends observed a decade earlier, although there are notable differences between the two distributions attributable to both seasonal and interannual variability. Measured pCa_B concentrations are highest (>1 μmol L^{-1}) in productive coastal waters south of Iceland. In 2003, relatively high concentrations were also observed in mid-latitude surface waters, resulting from high levels of productivity following the annual spring bloom in the temperate and

subpolar North Atlantic. This signal is less intense in the 2013 distribution, presumably due to the later date of sample collection and the rapid sinking rates expected for biogenic particles in this region after bloom decay (see discussion in section 3.3.1.2). However, pCa_B concentrations are consistently higher throughout the upper water column in tropical and subtropical waters in 2013 with an average increase of 20 nmol L^{-1}. Average particulate P concentrations along A16N also increased in 2013 compared to 2003 (see discussion in section 3.3.1.3; Figure A.1), indicating a generally higher level of productivity along the section. If we assume a stable phytoplankton community structure and coccolithophore calcification rate over the study period, the relative increase in particulate P concentrations is sufficient to support the presumed increase in productivity of calcifying organisms in 2013. Of course, temperature, salinity, irradiance, nutrient supply, and growth rate have all been shown to affect calcification in coccolithophores [*Beaufort et al*., 2007; *Zonderman*, 2007; *Bollman et al*., 2009; *Grelaud et al*., 2009] and we have no data to assess possible changes in community composition. However, average concentrations of PIC observed in the surface ocean in (sub) tropical waters (approximately 60 nmol L^{-1}) are comparable to those reported by *Poulton et al*. [2006] during sampling of this region in 2004 (**Fig. 4.2**), indicating that the values observed during sampling in 2013 are likely within the range of expected interannual variability in PIC production.

Dissolution rate estimates obtained using equation 4.8 and the distribution of pCa_B observed during the 2013 occupation of A16N are reported in **Table 4.1**. Dissolution rates in low-latitude (sub)tropical waters (0.8 mmol m^{-2} d^{-1}) are similar to those previously calculated from pCa_B and TA* distributions [*Barrett et al*., 2014]. This suggests that elevated PIC dissolution in corrosive intermediate waters may be a persistent feature of the carbonate cycle at low latitudes in the North Atlantic. However, in the mid- and high-latitude region, dissolution rates estimated from the 2013 particulate matter data are higher (0.6 mmol m^{-2} d^{-1}) than 2003 estimates. Such high rates of dissolution are unexpected given waters in this region are over-saturated with respect to both calcite and aragonite and low dissolution rates are estimated from excess alkalinity measurements [*Berelson et al*., 2007; *Barrett et al*., 2014]. This apparent variability in temperature and subpolar waters likely results from potentially large errors introduced by application of this approach to regions that have a strong seasonality in PIC production. In addition, the high densities of large, rapidly-sinking (75–160 m d^{-1}) phytoplankton and biological aggregates expected after the spring bloom in the North Atlantic [*Lochte et al*., 1993; *Briggs et al*., 2011] results in very different particle dynamics than are found in low latitude waters where degradation processes dominate and likely result in small particles with long residence times in the

upper 1000 m [*Barret et al*., 2015]. This repeat occupation of A16N highlights this limitation to using the distribution of PIC in suspended particulate matter to assess dissolution rates.

4.4. Conclusions

Observed attenuation of the pCa_B signal with depth reflects $CaCO_3$ dissolution as sinking particulate matter is exposed to intermediate waters that are undersaturated with respect to aragonite and high-Mg calcite in the (sub)tropical North Atlantic. The relatively high dissolution rates estimated for the top 1000 m suggest that biologically-mediated dissolution of calcite (and aragonite) may also be an active mechanism for upper water column $CaCO_3$ dissolution. Water-column carbonate dissolution rates calculated from pCa_B attenuation in this region show similar trends to those derived from TA* distributions. Thus, the use of small-volume, high-resolution suspended matter sampling may be useful to verify and constrain upper water column $CaCO_3$ dissolution estimates from carbon parameter measurements in the tropics and subtropics where seasonal productivity cycles are muted. This approach is limited in mid- and high-latitude regions with strong seasonal productivity cycles and where large, rapidly sinking biological aggregates are likely to dominate the particulate pool.

4.5 Appendix

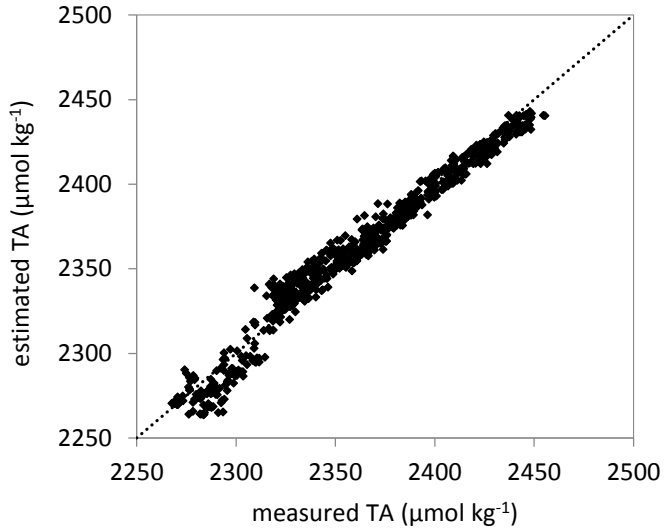

Figure B.1. Estimated total alkalinity plotted versus measured total alkalinity in µmol kg^{-1} for surface water (< 100 m) from the 2003 A16N and 2005 A16S sections plotted with the 1:1 line.

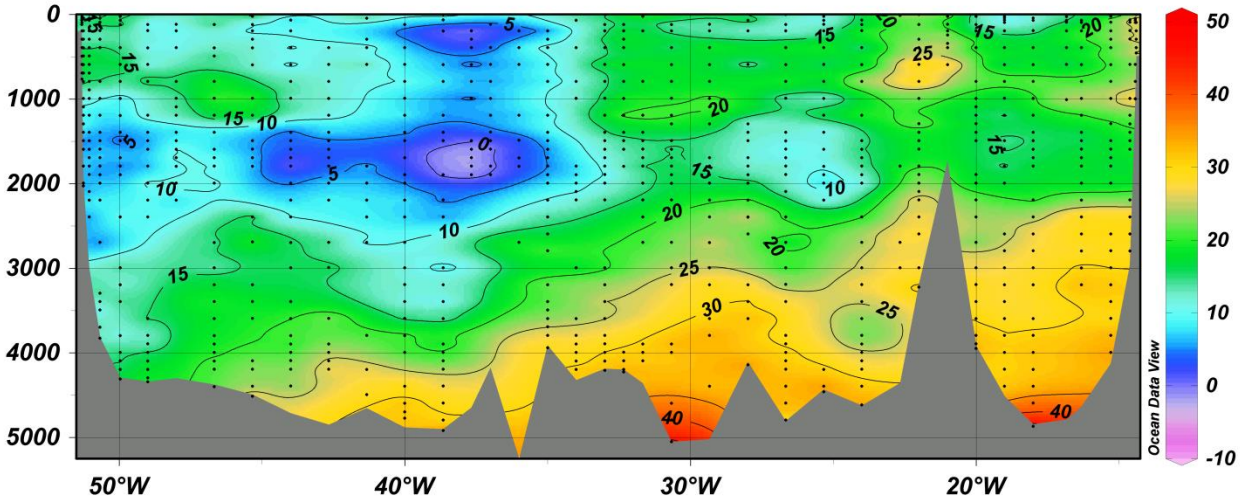

Figure B.2. TA* (µmol kg^{-1}) calculated using carbon measurements along the 1993 WOCE Atlantic zonal transect A06 along 8°N.

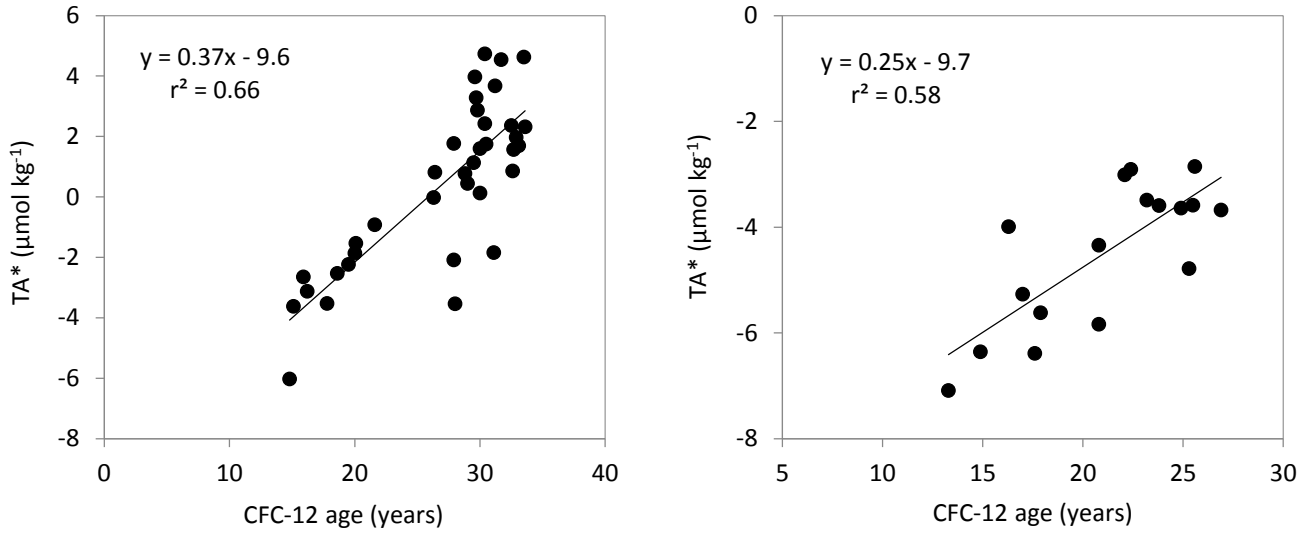

Figure B.3. Excess alkalinity (TA*) plotted versus CFC-12 age for data from A16N 2003 collected along the σ_θ=26.9 potential density surface in the low-latitude (0–30 °N) region (left) and along the σ_θ=27.3 potential density surface in the northern latitudes (30–55 °N) (right).

4.6 References

Anderson, L. A., Sarmiento, J.L., 1994. Redfield ratios of remineralization determined by nutrient data analysis. Global Biogeochem. Cycles 8, 65–80.

Armstrong, R.A., Lee, C., Hedges, J.I., Honjo, S., Wakeham, S.G., 2002. A new, mechanistic model for organic carbon fluxes in the ocean based on the quantitative association of POC with ballast materials. Deep-Sea Res. II 49, 219–236.

Balch, W.M., 2005. Calcium carbonate measurements in the surface global ocean based on Moderate-Resolution Imaging Spectroradiometer data. J. Geophys. Res. 110, C07001.

Balch, W.M., Kilpatrick, K., 1996. Calcification rates in the equatorial Pacific along 140 W. Deep-Sea Res. II 43, 971–993.

Baringer, M.O., Bullister, J.L., 2014. Cruise report: A16N. http://cchdo.ucsd.edu/data/4925/33RO20130803do.pdf

Barrett, P.M., Resing, J.A., Buck, N.J., Buck, C.S., Landing, W.M., Measures, C.I., 2012. The trace element composition of suspended particulate matter in the upper 1000 m of the eastern North Atlantic Ocean: A16N. Mar. Chem. 142–144, 42–53.

Beaufort, L., Probert, I., Buchet, N., 2007. Effects of acidification and primary production on coccolith weight: Implications for carbonate transfer from the surface to the deep ocean. Geochem. Geophys. Geosys. 8, Q08011.

Bednaršek, N., Možina, J., Vogt, M., O'Brien, C., Tarling, G.A., 2012. The global distribution of pteropods and their contribution to carbonate and carbon biomass in the modern ocean. Earth Syst. Sci. Data 4, 167–186.

Berelson, W.M., Balch, W.M., Najjar, R., Feely, R.A., Sabine, C., Lee, K., 2007. Relating estimates of $CaCO_3$ production, export, and dissolution in the water column to measurements of $CaCO_3$ rain into sediment traps and dissolution on the sea floor: A revised global carbonate budget. Global Biogeochem. Cycles 21, GB1024.

Berner, R.A., Honjo, S., 1981. Pelagic sedimentation of aragonite: Its geochemical significance. Science 211, 940–942.

Bishop, J.K.B., 1989. Regional extremes in particulate matter composition and flux: Effects on the chemistry of the ocean interior. in *Productivity of the Ocean: Present and Past*, edited by W.H. Berger, V.S. Smetacek, and G. Wefer, pp. 117–137, John Wiley & Sons Limited, New York, NY.

Bishop, J.K.B., Edmond, J.M., Ketten, D.R., Bacon, M.P., Silkers, W.B., 1977. The chemistry, biology, and vertical flux of particulate matter from the upper 400 m of the equatorial Atlantic Ocean. Deep Sea Res. 24, 511–548.

Bishop, J.K.B., Collier, R.W., Kettens, D.R., Edmond, J.M., 1980. The chemistry, biology, and vertical flux of particulate matter from the upper 1500 m of the Panama Basin. Deep Sea Res. A 27, 615–616.

Bollman, J. Herrle, J.O., Cortés, M.Y., Fielding, S.R., 2009. The effect of sea water salinity on the morphology of *Emiliania huxleyi* in plankton and sediment samples. Earth Planet. Sci. Lett. 284, 320–328.

Bory, A. J.-M., Newton, P.P., 2000. Transport of airborne lithogenic material down through the water column in two contrasting regions of the eastern subtropical North Atlantic Ocean. Global Biogeochem. Cycles 14, 297 – 315.

Brewer, P.G., Wong, G.T.F., Bacon, M.P., Spencer, D.W., 1975. An oceanic calcium problem? Earth Planet. Sci. Lett. 26, 81–87.

Broecker, W.S., 1974. "NO", a conservative water-mass tracer. Earth Planet. Sci. Lett. 23, 100–107.

Bullister, J.L., Weiss, R.F., 1988. Determination of $CC1_3F$ and $CC1_2F_2$ in seawater and air. Deep Sea Res. 25, 839-853.

Byrne, R.H., Acker, J.G., Betzer, P.R., Feely, R.A., Cates, M.H., 1984. Water column dissolution of aragonite in the Pacific Ocean. Nature 312, 321–326.

Caldeira, K., Wickett. M.E., 2003. Anthropogenic carbon and ocean pH. Nature 425, 365.

Chen, C.-T.A., 1978. Decomposition of calcium carbonate and organic carbon in the deep oceans. Science 201, 735–736.

Chen, C.-T.A., 2002. Shelf-vs. dissolution-generated alkalinity above the chemical lysocline. Deep Sea Res. II 49, 5365-5375.

Chiapello, I., Bergametti, G., Chatenet, B., Bousquet, P., Dulacand, F., Soares, E.S., 1997. Origins of African dust transported over the northeastern tropical Atlantic. J. Geophys. Res. 102*,* 13701–13709.

Chung, S.-N., Lee, K., Feely, R.A., Sabine, C.L., Millero, F.J., Wanninkhof, R., Bullister, J.L., Key, R.M., Peng T.-H., 2003. Calcium carbonate budget in the Atlantic Ocean based on water column inorganic carbon chemistry. Global Biogeochem. Cycles 17, 1093.

Chung, S.-N., Park, G.-H., Lee, K., Key, R.M., Millero, F.J., Feely, R.A., Sabine, C.L., Falkowski, P.G., 2004. Postindustrial enhancement of aragonite undersaturation in the upper tropical and subtropical Atlantic Ocean: The role of fossil fuel CO_2. Limnol. Oceanogr. 49, 315–321.

Dickson, A.G., Millero, F.J., 1987. A comparison of the equilibrium constants for the dissociation of carbonic acid in seawater media. Deep-Sea Res. 34, 1733–1743.

Doney, S.C., Bullister, J.L., 1992. A chlorofluorocarbon section in the eastern North Atlantic. Deep Sea Res. 39, 1857–1883.

Doney, S.C., Fabry, V.J., Feely, R.A., Kleypas, J.A., 2009. Ocean Acidification: The Other CO_2 Problem. Ann. Rev. Mar. Sci. 1, 169-192.

Dunne, J.P., Hales, B., Toggweiler, J.R., 2012. Global calcite cycling constrained by sediment preservation controls. Global Biogeochem. Cycles 26, GB3023.

Fabry, V.J., Deuser, W.G., 1991. Aragonite and magnesian calcite fluxes to the deep Sargasso Sea. Deep Sea Res. 38, 713–728.

Feely, R.A., Byrne, R.H., Acker, J.G., Betzer, P.R., Chen, C.-T.A., Gendron, J.F., Lamb, M.F., 1988. Winter-summer variations of calcite and aragonite in the Northeast Pacific. Mar. Chem. 25, 227–241.

Feely, R.A., Massoth, G.J., Lebon, G.T., 1991. Sampling of marine particulate matter and analysis by X-ray fluorescence spectrometry. in Marine Particles: Analysis and Characterization, AGU Geophysical Monograph Series, edited by D.C. Hurd, and D.W. Spencer, pp. 251–257, AGU, Washington, D.C.

Feely, R.A., Sabine, C.L., Lee, K., Millero, F.J., Lamb, M.F., Greeley, D., Bullister, J.L., Key, R.M., Peng, T.-H., Kozyr, A., Ono, T., Wong, C.S., 2002. In situ calcium carbonate dissolution in the Pacific Ocean. Global Biogeochem. Cycles 16, 1144.

Feely, R.A., Sabine, C.L., Lee, K., Berelson, W., Kleypas, J., Fabry, V.J., Millero, F.J., 2004. Impact of anthropogenic CO_2 on the $CaCO_3$ system in the oceans. Science 305, 362–366.

Feely, R.A., Sabine, C.L., Byrne, R.H., Millero, F.J., Dickson, A.J., Wanninkhof, R., Murata, A., Miller, L.A., Greeley, D., 2012. Decadal changes in the aragonite and calcite saturation state of the Pacific Ocean. Global Biogeochem. Cycles 26, GB3001.

Formenti, P., Elbert, W., Maenhaut, W., Haywood, J., Andreae, M.O., 2003. Chemical composition of mineral aerosol dust during the Saharan Dust Experiment (SHADE) airborne campaign in the Cape Verde region, September 2000. J. Geophys. Res. 108, 8576.

Friis, K., Najjar, R.G., Follows, M.J., Dutkiewicz, S., 2006. Possible overestimation of shallow-depth calcium carbonate dissolution in the ocean. Global Biogeochem. Cycles 20, GB4019.

Friis, K., Najjar, R.G., Follows, M.J., Dutkiewicz, S., Kortzinger, A., Johnson, K.M., 2007. Dissolution of calcium carbonate: observations and model results in the subpolar North Atlantic. Biogeosci. 4, 205–213.

Gehlen, M., Gruber, N., Gangstø, R.,Bopp, L., Oschlies, A., 2011. Biogeochemical consequences of ocean acidification and feedbacks to the earth system. in *Ocean Acidification*, edited by J.-P. Gattuso and L. Hansson, pp. 230-248, Oxford University Press, New York, NY.

Grelaud, M., Schimmelmann, A., Beaufort, L., 2009. Coccolithophore response to climate and surface hydrography in Santa Barbara Basin, California, AD 1917–2004. Biogeosci. 6, 2025–2039.

Henson, S.A., Dunne, J.P., Sarmiento, J.L., 2009. Decadal variability in North Atlantic phytoplankton blooms. J. Geophys. Res. 114, C04013.

Hofmann, M., Schellnhuber, H.-J., 2009. Oceanic acidification affects marine carbon pump. Proc. Nat. Acad. Sci. 106, 3017–3022.

Honjo, S., Manganini, S.J., Krishfield, R.A., Francois, R., 2008. Particulate organic carbon fluxes to the ocean interior and factors controlling the biological pump: A synthesis of global sediment trap programs since 1983. Prog. Oceanogr. 76, 217–285.

Ingle, S.E., 1975. Solubility of calcite in the ocean. Mar. Chem. 4, 301–319.

Jansen, H., Wolf-Gladrow. D.A., 2001. Carbonate dissolution in copepod guts: A numerical model. Mar. Ecol. Prog. Ser. 221, 199–207.

Jiang, L.-Q., Feely, R.A., Carter, B.R., Greeley, D.J., Gledhill, D.K., Arzayus, K.M., 2015. Climatological distribution of aragonite saturation state in the global oceans. Biogeochem. Cycles doi:10.1002/2015GB005198.

Johnson, K.M., Wills, K.D., Butler, D.B., Johnson, W.K., Wong, C.S., 1993. Coulometric total carbon dioxide analysis for marine studies: maximizing the performance of an automated gas extraction system and coulometric detector. Mar. Chem. 44, 167–187.

Kanamori, S., Ikegami, H., 1982. Calcium-alkalinity relationship in the North Pacific. J. Oceanogr. Soc. Japan 38, 57–62.

Karstensen, J., Stramma, J.L., Visbeck, M., 2008. Oxygen minimum zones in the eastern tropical Atlantic and Pacific oceans. Prog. Oceanogr. 77, 331–350.

Lebrato, M., Inglesias-Rodriguez, D., Feely, R.A., Greeley, D., Jones, D.O.B., Suarez-Bosche, N., Lampitt, R.S., Cartes, J.E., Green, D.R.H., Akler, B.,2010. Global contribution of echinoderms to the marine carbon cycle: $CaCO_3$ budget and benthic compartments. Ecol. Monogr. 80, 441–467.

Lewis, E., Wallace, D.W.R., 1998. Program developed for CO_2 system calculations, Rep. 105, Oak Ridge Natl. Lab., U.S. Dep. of Energy, Oak Ridge, Tenn. (Available at http://cdiac.esd.ornl.gov/oceans/ co2rprt.html).

Mayzaud, P. Martin, J.L., 1975. Some aspects of the biochemical and mineral composition of marine plankton. J. Exp. Mar. Biol. Ecol. 17, 297–310.

Measures, C.I., Landing, W.M., Brown, M.T., Buck, C.S., 2008a. A commercially available rosette system for trace metal-clean sampling. Limnol. Oceanogr. Methods 6, 384–394.

Measures, C.I., Landing, W.M., Brown, M.T., Buck, C.S., 2008b. High-resolution Al and Fe data from the Atlantic Ocean CLIVAR-CO_2 Repeat Hydrography A16N transect: Extensive linkages between atmospheric dust and upper ocean geochemistry. Global Biogeochem. Cycles 22, GB1005.

Merbach, C., Culberson, C.H., Hawley, J.E., Pytkowicz, R.M., 1973. Measurement of the apparent dissociation constant of carbonic acid in seawater at atmospheric pressure. Limnol. Oceanogr. 18, 897–907.

Millero, F. J., Zhang, J.Z., Lee, K., Campbell, D.M., 1993. Titration alkalinity of seawater. Mar. Chem. 44, 153–165.

Millero, F.J., 1995. Thermodynamics of the carbon dioxide system in the oceans. Geochim. Cosmochim. Acta 59, 661–677.

Millero, F.J., 2006. Composition of the major components of seawater. in *Chemical Oceanography,* 3rd ed*.,* pp. 55–88, CRC Press, Boca Raton, Fla.

Milliman, J., Troy, P., Balch, W., Adams, A., Li, Y., Mackenzie, F., 1999. Biologically mediated dissolution of calcium carbonate above the chemical lysocline? Deep-Sea Res. I 46*,* 1653–1669.

Mucci, A., 1983. The solubility of calcite and aragonite in seawater at various salinities, temperatures, and one atmospheric total pressure. Am. J. Sci. 283, 781–799.

Paulmier, A., Ruiz-Pino, D., Garçon, V., 2011. CO_2 maximum in the oxygen minimum zone (OMZ). Biogeosci. 8, 239–252.

Peltola, E., Wanninkhof, R., Feely, R., Hansell, D., Castle, R., Greeley, D., Zhang, J.-Z., Millero, F., Gruber, N., Bullister, J., Graham, T., 2005. *Inorganic and Organic Carbon, Nutrient, and Oxygen Data from the R/V Ronald H. Brown Repeat Hydrography Cruise in the Atlantic Ocean: CLIVAR CO_2 Section A16N_2003a (4 June - 11 August, 2003), ORNL/CDIAC-149, NDP-085,* Carbon Dioxide Information Analysis Center, Oak Ridge National Laboratory, U.S. Department of Energy, Oak Ridge, Tennessee, doi: 10.3334/CDIAC/otg.ndp085.

Planquette, H., Sherrell, R., 2012. Sampling for particulate trace metal determination using water sampling bottles: methodology to in situ pumps. Limnol. Oceanogr. Methods 10, 367–388.

Poulton, A.J., Sanders, R., Holligan, P.M., Stinchcombe, M.C., Adey, T.R., Brown, L., Chamberlain, K., 2006. Phytoplankton mineralization in the tropical and subtropical Atlantic Ocean. Global Biogeochem. Cycles 20*,* GB4002.

Sabine, C.L., Key, R.M., Feely, R.A., Greeley, D., 2002. Inorganic carbon in the Indian Ocean: Distribution and dissolution processes. Global Biogeochem. Cycles 16, 1067.

Sabine, C.L. et al., 2004. The oceanic sink for anthropogenic CO_2. Science 305, 367–71.

Schiebel, R., 2002. Planktic foraminiferal sedimentation and the marine calcite budget. Global Biogeochem. Cycles 16, 1065.

Schlitzer, R., 2010. Ocean Data View. http://odv.awi.de.

Schütz, L., Sebert, M., 1987. Mineral aerosols and source identification. J. Aerosol Sci. 18, 1–10.

Sherrell, R.M., Field, M.P., Gao, Y., 1998. Temporal variability of suspended mass and composition in the Northeast Pacific water column: relationships to sinking flux and lateral advection. Deep Sea Res. II 45*,* 733–761.

Stramma, L., Hüttle, S., Schafstall, J., 2005. Water masses and currents in the upper tropical northeast Atlantic off northwest Africa. J. Geophys. Res. 110, C12006.

Stramma, L., Johnson, G.C., Sprintall, J., Mohrholz, V., 2008. Expanding oxygen-minimum zones in the tropical oceans. Science 320, 655-658.

Wanninkhof, R., Doney, S.C., Bullister, J.L., Levine, N.M., Warner, M., Gruber, N., 2010. Detecting anthropogenic CO_2 changes in the interior Atlantic Ocean between 1989 and 2005. J. Geophys. Res. 115, C11028.

Wedepohl, K.H., 1995. The composition of the continental crust. Geochim. Cosmochim. Acta. 59, 1217–1232.

Wilson, R.W., Millero, F.J., Taylor, J.R., Walsh, P.J., Christensen, V., Jennings, S., Grosell, M., 2009. Contribution of fish to the marine inorganic carbon cycle. Science 323, 359–362.

Woosley, R.J., Millero, F.J., Grosell, M., 2012. The solubility of fish-produced high magnesium calcite in seawater. J. Geophys. Res. *117,* C04018.

Zondervan, I., 2007. The effects of light, macronutrients, trace metals and CO2 on the production of calcium carbonate and organic carbon in coccolithophores—A review. Deep-Sea Res II 54, 521–537.

Table 4.1. Summary of upper-water column $CaCO_3$ dissolution estimates along A16N in 2003 and 2013 and previously reported estimates.

reference	method	location	depth (m)	$CaCO_3$ dissolution (mmol m^{-2} d^{-1})	
				2003[a]	2013
this work	pCa_B	mid-latitude N. Atlantic	200–1000	0.2	0.7
	pCa_B	(sub)tropical N. Atlantic	200–1000	0.9	0.8
this work	TA*	mid-latitude N. Atlantic	200–1000	0.5[a,b]	
	TA*	(sub)tropical N. Atlantic	200–1000	0.7[a,b]	
Berelson et al. [2007]	TA*	Atlantic	200–1500	0.3	
	TA*	Pacific	200–1500	0.8	
	TA*	Indian	200–1500	1.1	

[a]as reported in *Barrett et al*. [2014]

[b]value calculated from TA* concentrations less than the range of standard error

Table 4.2. Contributions of biogenic $CaCO_3$ (pCa_B), lithogenic pCa, and organic pCa to Ca concentrations measured in particulate matter samples along A16N in 2003 and 2013.

	A16N 2003		A16N 2013	
	surface ocean (<100 m)	all (0–1000 m)	surface ocean (<100 m)	all (0–1000 m)
biogenic $CaCO_3$	88%	89%	87%	91%
lithogenic pCa	4%	6%	2%	3%
organic pCa	8%	5%	11%	6%

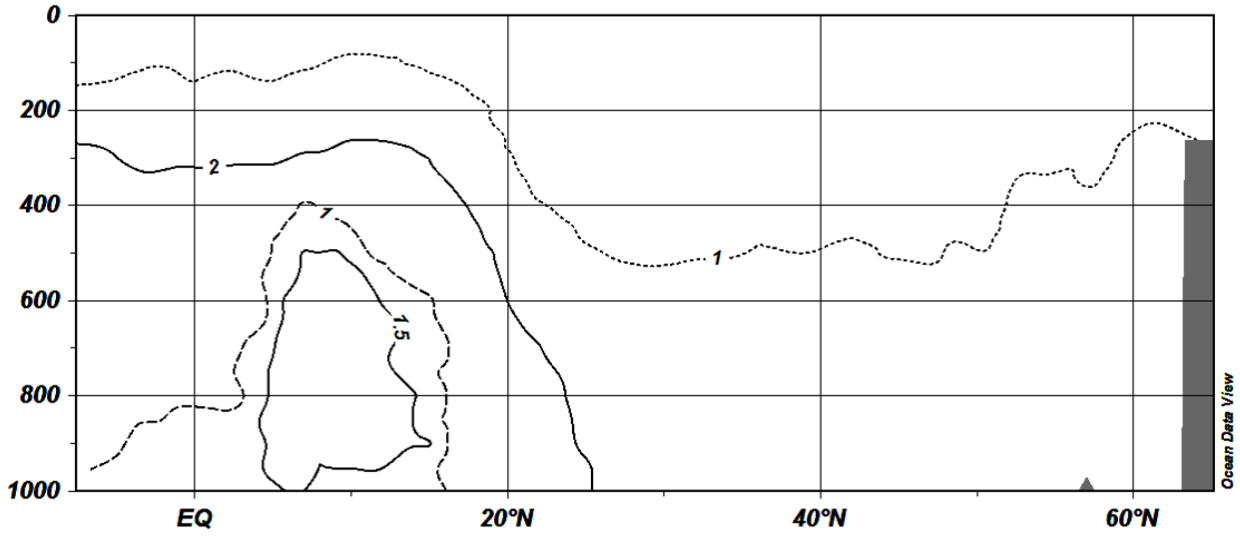

Figure 4.1. The saturation state of seawater with respect to calcite (solid line), aragonite (dashed line), and fish-produced high-Mg calcite (dotted line) in the top 1000 m along CLIVAR A16N in 2003.

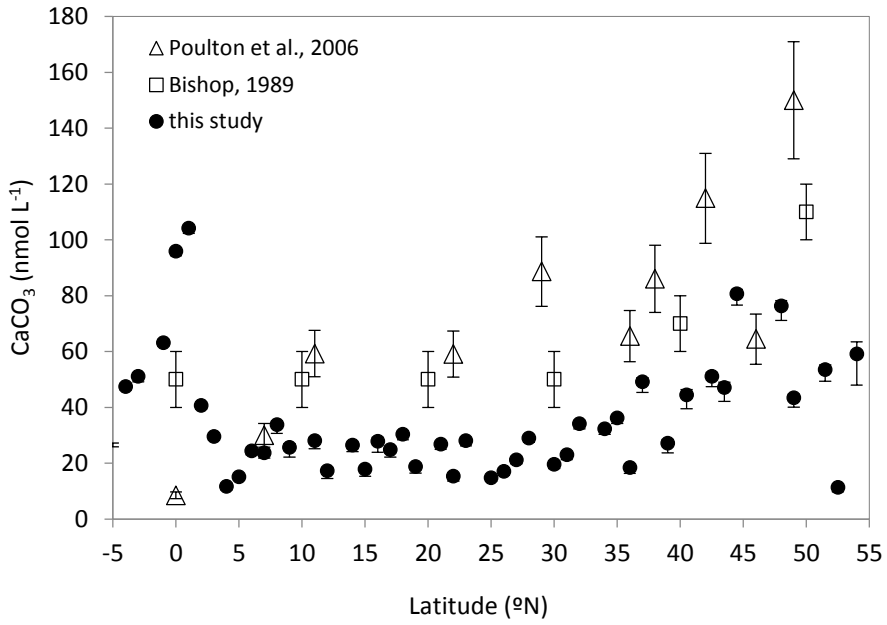

Figure 4.2. A comparison of average euphotic zone concentrations (<100 m) of pCa_B (this study), average particulate inorganic carbon (PIC) in the euphotic zone reported by *Poulton et al*. [2006], and average particulate calcium carbonate estimates for the top 500 m from *Bishop* [1989]. Error calculations for pCa_B are detailed in section 4.3.2; where no error bar is shown, error is contained within the symbol. Error bars shown for *Bishop* [1989] represent adjacent contour values; error bars shown for *Poulton et al.* [2006] represent reported relative standard deviation of 14%.

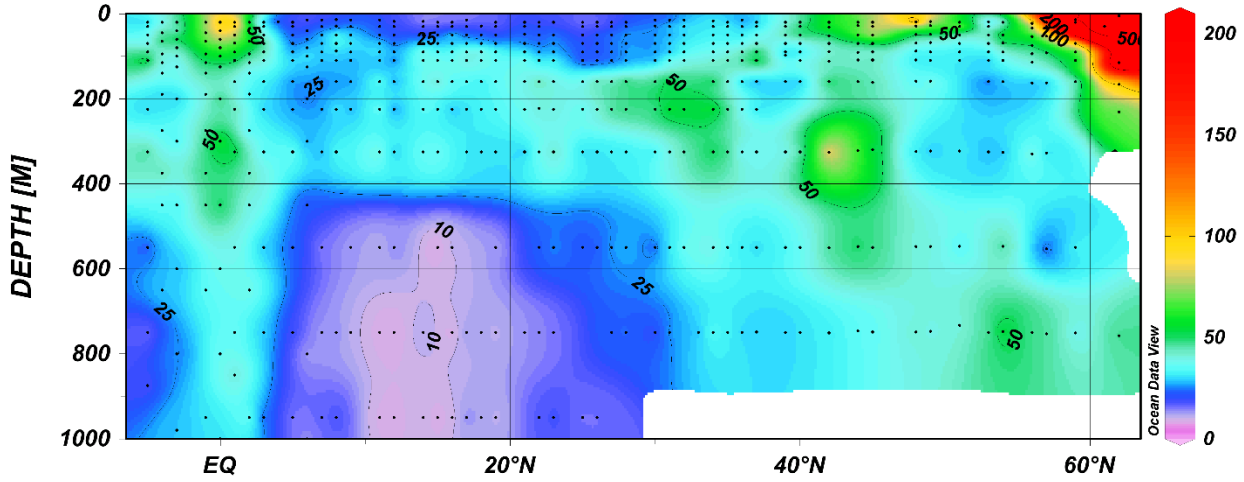

Figure 4.3. Distribution of biogenic particulate Ca (nmol L^{-1}) in the top 1000 m along CLIVAR A16N in 2003. The color-scale at right has been restricted to a range of 0 to >200 nmol L^{-1} to focus on the concentrations observed in open-ocean samples; higher concentrations (> 1 µmol L^{-1}) are found in coastal samples. Black points indicate individual samples.

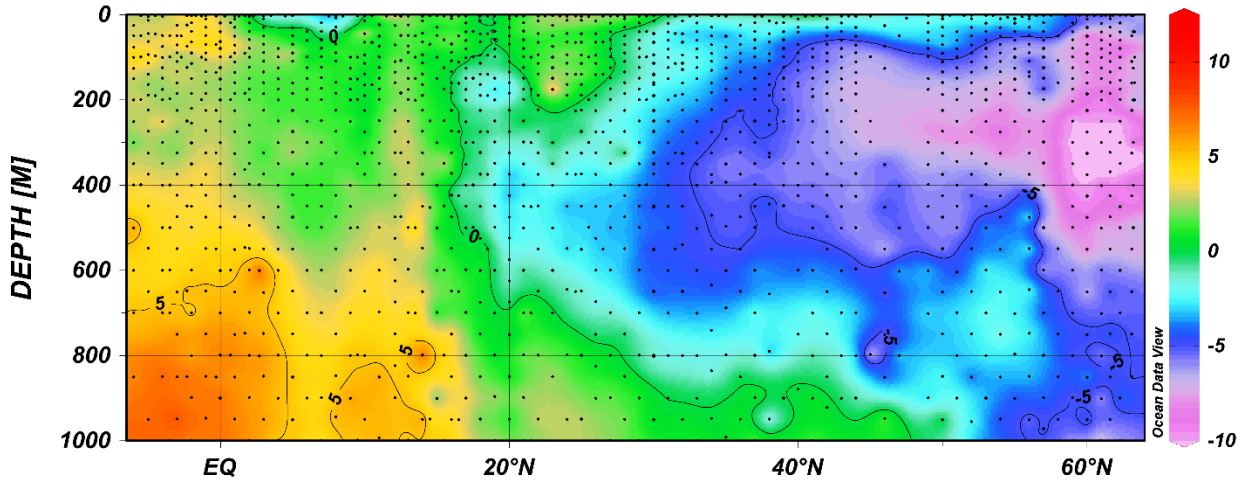

Figure 4.4. Estimated TA* concentrations (µmol kg^{-1}) in the top 1000 m along CLIVAR A16N in 2003. Black points indicate individual samples.

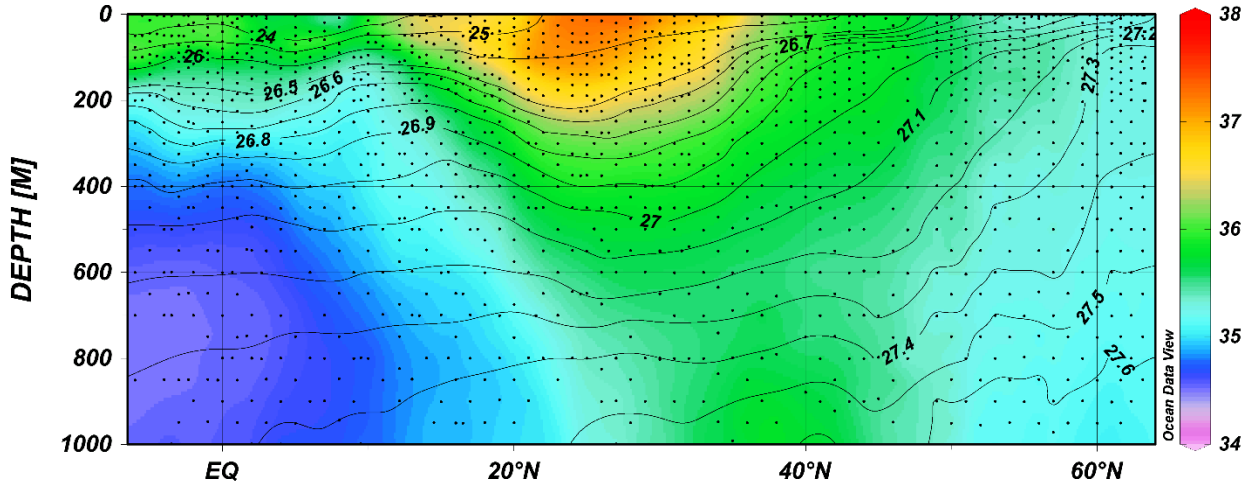

Figure 4.5. Salinity in the top 1000 m along CLIVAR A16N in 2003 overlaid with contours of potential density. Black points indicate individual samples.

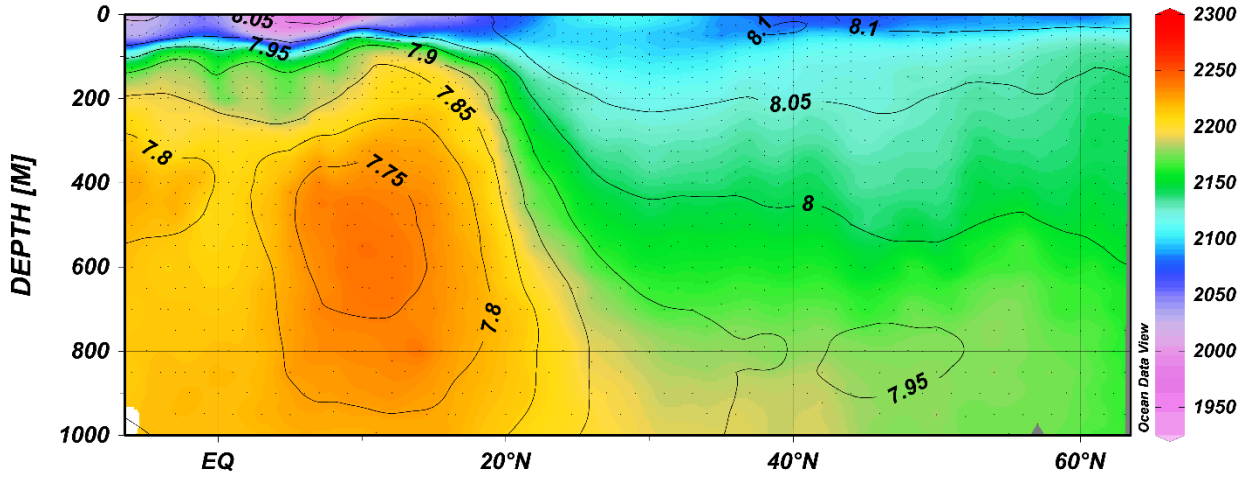

Figure 4.6. Distribution of DIC (µmol kg^{-1}) with contours indicating pH values in the top 1000 m along CLIVAR A16N in 2003. Black points indicate individual samples.

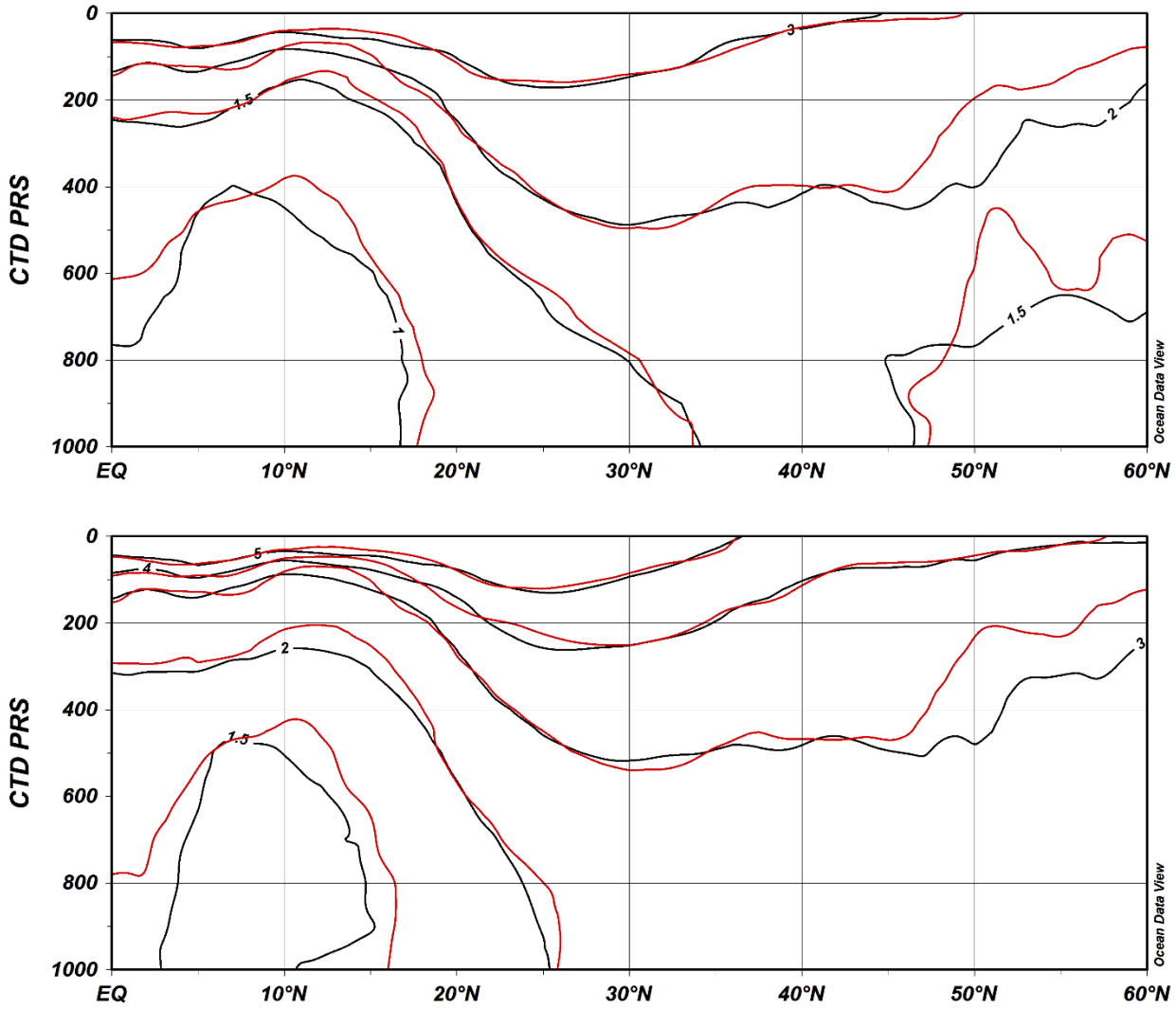

Figure 4.7. The saturation state of seawater with respect to aragonite (top) and calcite (bottom) in the top 1000 m along CLIVAR A16N in 2013 (red) compared to 2003 (black).

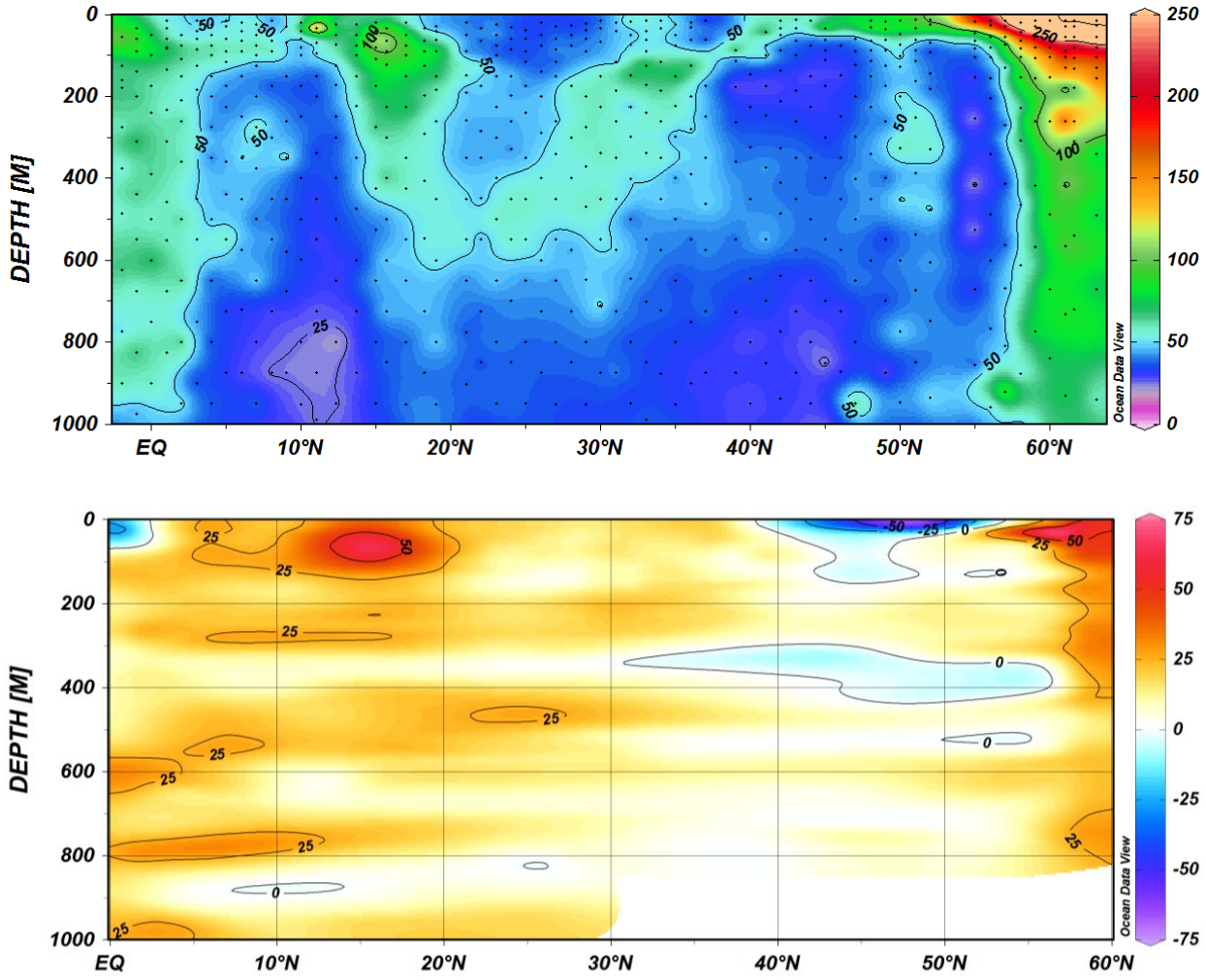

Figure 4.8. Distribution of biogenic particulate Ca in the top 1000 m along CLIVAR A16N in 2013 (top). The color scale at right has been restricted to <250 nmol L^{-1} to focus on the range of concentrations observed in open ocean samples; higher concentrations (>1 µmol L^{-1}) are observed in surface waters at stations near the Icelandic coast. Black points indicate individual samples. Change in biogenic particulate Ca concentrations (nmol L^{-1}) between the equator and 60°N in 2013 relative to 2003 (bottom).

Chapter 5. Stable isotope composition of particulate Cu in the North Atlantic

5.1 Introduction

Cu is an essential micronutrient required in various phytoplankton metalloenzymes [*Morel et al.*, 2003 and references therein]. However, Cu is also a potential toxin at sufficiently high concentrations [*Sunda and Guillard*, 1976], affecting rates of photosynthesis and cell division. Different phytoplankton populations are known to have varying metabolic requirements for Cu. For example, diatoms have relatively high Cu uptake rates, especially under Fe-limiting conditions, while bacterioplankton such as prochlorococcus display low Cu-tolerance [*Mann et al*., 2002]. Dissolved Cu in seawater is known to be strongly complexed (>99.9%) to organic ligands [*Coale and Bruland*, 1988; *Moffet and Dupont*, 2007], which are thought to be produced by a wide range of phytoplankton taxa in response to the toxicity of the free Cu^{2+} ion [*Coale and Bruland*, 1990; *Moffett and Brand*, 1996].

Continental run-off and atmospheric deposition are a major supply of dissolved Cu to the surface ocean. Estimates of riverine Cu inputs are relatively well-constrained ($\pm$ 40%) [*Boyle et al*., 1977; *Gaillerdet et al*., 2003] [*Duce et al*., 1991] compared to current estimates for the atmospheric flux of aerosol Cu, which range over an order of magnitude, in part because of uncertainty about the relative importance of lithogenic mineral aerosols and anthropogenic pollution sources. Cu is taken up by phytoplankton and remineralized at depth, although the surface depletion and enrichment at depth is typically not as strong as for other nutrient-like trace elements. Particle scavenging processes are also thought to be a strong control on the distribution of dissolved Cu [*Bruland and Lohan*, 2003] and recent work has shown that dissolved Cu profiles can be explained by a reversible scavenging model [*Little et al*., 2013]. Release from benthic sediment is also thought to represent a strong supply of dissolved Cu in the deep ocean [*Boyle et al*., 1977; *Takano et al*., 2014].

The Cu stable isotope composition ($\delta^{65}Cu$) of seawater has been investigated in recent studies to further understanding of the marine biogeochemical cycling of Cu [*Bermin et* al., 2006; Vance *et al.*, 2008; *Thompson et al*., 2013; *Little et al*., 2014a,b]. Box models employing a Cu isotopic mass balance for the global ocean have been proposed to better constrain fluxes such as the atmospheric input of Cu to the surface ocean [*Takano et al*., 2014]. However, there are still relatively few measurements of seawater $\delta^{65}Cu$ reported in the literature to date and the cycling of Cu isotopes in the modern ocean is still poorly understood. In particular, previous studies have reached contradictory conclusions about the role of active biological uptake of Cu by phytoplankton and passive adsorption of Cu onto particles in controlling seawater $\delta^{65}Cu$ values. In a study of estuarine Cu isotopic composition, *Vance et al*. [2008] found a consistent offset between dissolved and particulate $\delta^{65}Cu$ and suggested that equilibrium

fractionation between the two pools results in isotopically light particulate Cu in rivers. By contrast, *Thompson et al.* [2013] observed a δ^{65}Cu minimum at the depth of the fluorescence maximum in dissolved Cu profiles in the Tasman Sea and proposed that marine particles may preferentially scavenge heavy Cu. *Bermin et al.* [2006] similarly proposed that release of isotopically heavy Cu from remineralization of particulate organic matter could be responsible for subsurface maxima in dissolved δ^{65}Cu profiles in the Northeast Pacific. Most recently, examining profiles of dissolved δ^{65}Cu from the North Pacific and South Indian Oceans, *Takano et al*. [2014] concluded that biological uptake of Cu and adsorption onto biogenic particles resulted in no significant isotopic fractionation of Cu in the surface ocean.

Another possible factor complicating interpretation of seawater δ^{65}Cu is the effect of anthropogenic pollution on the isotopic signature of atmospheric Cu inputs. Anthropogenic emission sources are thought to be a significant source of aerosol Cu deposited on the surface ocean [*Duce et al*., 1991; *Paytan* et al., 2009]. However, few measurements of δ^{65}Cu in marine aerosols have been reported [*Dong et al*., 2013; *Little et al*., 2014a], making systematic variation in aerosol δ^{65}Cu with atmospheric source region difficult to determine from current datasets. However, there are indications that anthropogenic Cu sources may impact the δ^{65}Cu signature of the aerosol Cu flux to the oceans. Analysis of marine aerosols from the eastern tropical North Atlantic by *Dong et al*. [2013] revealed that aerosol samples were enriched in Cu and isotopically heavy relative to the composition of dust from source regions in the Sahel desert, suggesting contributions of Cu from non-lithogenic sources. Similar findings were reported by *Thapalia et al.* [2010] in a study of δ^{65}Cu variation in a sediment record from an urban lake in which increased anthropogenic Cu input from local smelter emissions was found to be associated with isotopically heavy Cu.

In this work, particulate matter samples from 4 stations along CLIVAR/CO_2 Repeat Hydrography section A16N were analyzed for stable Cu isotopic composition (**Fig. 5.1**). The station locations span diverse geochemical provinces in the North Atlantic with varying levels of primary production and both natural lithogenic and anthropogenic aerosol Cu inputs. Analyses of particulate fractions of open-ocean Cu will be used to constrain the effects of biological uptake, particle scavenging, and aerosol source in controlling seawater δ^{65}Cu distributions.

5.2 Methods

5.2.1 Sample collection

Seawater was collected at 12 depths in the upper 1000 m using 12 L GO-FLO bottles mounted on a trace metal-clean rosette and processed in a clean laboratory van equipped with a HEPA filtered air system [*Measures et al.*, 2008]. Subsamples were pressure-filtered (<55 kPa, filtered compressed air) through acid-cleaned, 0.4 µm track-etched polycarbonate filters. The average filtration volume was 9 L. Suspended particulate matter filter samples were rinsed immediately after collection with a 15–20 mL DI water (adjusted to pH 8 with dilute ammonia) with a low vacuum applied to remove residual seasalt while avoiding loss or redistribution of particles.

5.2.2 Analytical methods for Cu concentration

Concentrations of particulate Cu in suspended particulate matter filter samples were determined by energy-dispersive X-ray fluorescence (ED-XRF) conducted under a vacuum atmosphere using thin film principles on a Thermo Fisher Quant'X equipped with a Rhodium Target X-Ray tube and an electronically-cooled, lithium-drifted solid state detector [*Barrett et al*., 2012]. The minimum detection limit was 1.25 ng Cu cm^{-2}, or 0.027 nmol L^{-1} for the average filtration volume of 9 L. Dissolved Cu concentrations were determined by HR ICP-MS at Florida State University [*P. Morton*, personal communication] using the isotope dilution method of *Milne et al*. [2010] with a minimum detection limit of 0.007 nmol L^{-1}.

5.2.3 Microwave digest and anion-exchange column separation

All sample digest and purification procedures were performed in a clean lab using double-distilled acid reagents. Suspended particulate matter samples were first subjected to a HNO_3/HF acid microwave digestion procedure as described in **section 2.2.4** then run on an anion exchange column (AG MP-1) to separate the pure Cu fraction from major ions and other trace elements using a procedure modified from *Maréchal et al*. [1999]. The AG MP-1 columns were cleaned by eluting with 10 mL 0.5 N HNO_3 followed by 5 mL deionized water, repeated three times. The resin was conditioned with 6 mL 7N HCl + 0.001% H_2O_2 and dried sample digest solutions were re-dissolved and loaded with 1 mL 7 N HCl + 0.001% H_2O_2. Major ions were eluted with 4 mL 7 N HCl + 0.001% H_2O_2 before eluting Cu with an additional 26 mL 7 N HCl + 0.001% H_2O_2. The Cu fractions were evaporated to dryness, re-dissolved in several drops of concentrated HNO_3, dried down again, and then brought up in 2 mL 2% HNO_3 for MC ICP-MS analysis.

Incomplete yields from the column separation procedure have been shown to significantly affect sample δ^{65}Cu [*Thompson et al*., 2013]. The column separation procedure was tested for potential isotopic fractionation effects by loading up to 5 μg Cu (in-house Claritas PPT standard) on the anion exchange columns and comparing the isotopic composition of the Cu eluate to the untreated Cu standard (**Figure 5.2**). The measured δ^{65}Cu of column-eluted Cu standard solutions was statistically indistinguishable from the untreated Cu standard (0.012 $\pm$ 0.095 ‰, 2SD, n = 9), indicating complete Cu recovery from the anion exchange column procedure with no significant isotopic fractionation effects.

5.2.4 Mass spectrometry

Isotopic analyses were performed on a NuPlasma multi-collector ICP-MS (MC ICP-MS). Sample solutions were introduced under dry plasma conditions using a DSN-100 Desolvating Nebuliser. Standard operating conditions and Faraday cup configuration for Cu isotope analysis are detailed in **Table 5.1**. The background was recorded prior to taking data by deflecting the beam out of the faraday cups. The instrument was tuned daily to optimize signal intensity and peak shape. Typical total beam intensities were 0.4 V for 25 ppb Cu and 1.2 V for 25 ppb Zn.

Instrumental fractionation was corrected by normalizing to an external Zn standard. All standards and samples were spiked with Claritas PPT Zn standard in a 2:1 Cu:Zn ratio. The instrumental fractionation was determined according to the exponential form of the generalized power law for mass fractionation:

$$R = r\left(\frac{M_2}{M_1}\right)^{\beta} \tag{5.1}$$

where r is the measured ratio of isotopes with masses M_1 and M_2, R is the true isotopic ratio, and β is the mass fractionation coefficient. Reported Cu isotope data were corrected using the ^{66}Zn/^{64}Zn ratio. Instrumental drift was corrected using standard-sample bracketing. All Cu isotope data are reported using standard delta notation:

$$\delta^{65}\text{Cu (‰)} = \left[\frac{R_{\text{sample}}}{R_{\text{standard}}} - 1\right] \times 10^3 \tag{5.2}$$

where R_{sample} is the corrected $^{65}Cu/^{63}Cu$ ratio calculated using Eq. (5.1) and $R_{standard}$ is the mean of bracketing standard runs. Samples were measured relative to standard reference material NIST 976. The precision of the isotopic analysis (±0.11‰, 2 standard deviations) was determined from the variability of in-house Cu standard (Claritas PPT) relative to NIST 976 (**Figure 5.3**). The separation factor between the $\delta^{65}Cu$ values of particulate and dissolved Cu in seawater is discussed using Δ notation:

$$\Delta^{65}Cu_{particle-dissolved} = \delta^{65}Cu_{particle} - \delta^{65}Cu_{dissolved} \quad (5.3)$$

where $\delta^{65}Cu_{particle}$ and $\delta^{65}Cu_{dissolved}$ are the isotopic composition of the particulate and dissolved phase, respectively, in delta notation from equation 5.2.

5.3 Results

5.3.1 Hydrography

Salinity, temperature, and dissolved oxygen are plotted for Cu isotope stations along A16N (see **Fig. 3.1**) in **Figure 5.4**. Although the hydrography of the entire section has been presented previously [*Wanninkhof et al*., 2010], the major features in the upper 1000 m at selected stations for $\delta^{65}Cu$ are discussed briefly here. The T-S properties in the main thermocline at stations 21 (55°N) and 41 (55°N) are characteristic of North Atlantic Central Water. Low surface salinities at stations 107 (10°N) and 130 (0°) indicate the influence of excess precipitation in the equatorial North Atlantic. The main thermocline at these stations is occupied by South Atlantic Central Water based on T-S characteristics [*Stramma and England*, 1999]. The presence of Antarctic Intermediate Water (AAIW), which extends to approximately 15°N in the North Atlantic, is evident at stations 107 and 130 by the subsurface salinity minimum at approximately 700–900 m [*Wanninkhof et al*., 2010]. Stations 107 and 130 are also within the oxygen minimum zone in the eastern tropical Atlantic and have minimum dissolved O_2 concentrations of 40–100 μmol kg^{-1} at depths of 300–500 m.

5.3.2 Dissolved and particulate Cu concentrations

Vertical profiles of particulate (pCu) at stations 21, 42, 107, and 130 are presented in **Figure 5.5** with corresponding dissolved Cu (dCu) data where available [*P. Morton*, personal communication]. Vertical profiles of pCu show maximum concentrations in near-surface samples due to the large inputs of pCu from aerosol deposition on open-ocean surface waters. Below depths of ~60 m, pCu concentrations are relatively constant with depth, ranging from 0.10 ± 0.01 at station 130 to 0.16 ± 0.1

nmol L^{-1} at station 21. Overall, pCu concentrations decreased slightly from the northernmost station at 55°N to the southernmost station at the equator, likely reflecting the importance of Cu-rich anthropogenic aerosols from pollution sources in North America and Europe [*Buck et al*., 2010] in supplying Cu to the North Atlantic.

Similar features are apparent in pCu profiles reported by *Twining et al*. [2015] in the upper 150 m of the North Atlantic along the 2010/2011 GEOTRACES NAZT. Their dataset also shows maxima in pCu concentrations in near-surface samples above the depth of the subsurface chlorophyll maximum. The maximum surface enrichments (up to ~80 pmol L^{-1}) observed by *Twining et al.* [2015] in the North Atlantic (17–40°N) are somewhat lower than the maximum values observed in this work, likely due to sampling location in the subtropical gyre where both anthropogenic [*Paytan et al*., 2009] and lithogenic [*Jickells et al*., 2005] aerosol deposition is relatively low. *Kuss and Kremling* [1999] observed similarly low pCu in North Atlantic subtropical surface waters (17 pmol L^{-1}) but significantly higher average pCu concentrations (254 pmol L^{-1}) at higher latitudes (44–60°N) that are comparable to surface-ocean pCu concentrations observed at stations 21 and 41 (45–55°N) in this work.

Dissolved Cu profiles show minimum values in the surface layer that gradually increase with depth up to 1.5 nmol L^{-1}. The distribution of dCu also shows a general trend of decreasing concentrations from north to south throughout the upper 1000 m along the A16N transect. This trend is most pronounced in surface waters where dCu concentrations decline from 1.2 to 0.6 nmol L^{-1} from the northernmost to the southernmost station. This trend is likely due in part to the large inputs of soluble anthropogenic Cu from anthropogenic sources in the mid- and high-latitude North Atlantic. However, both *Jacquot and Moffett* [2015] and *Roshan and Wu* [2015] have shown that upper-ocean dCu concentrations are also relatively depleted in the eastern (sub)tropical North Atlantic due to scavenging by high concentrations of suspended particles from both aerosol deposition and biological productivity. Observations along the A16N transect generally compare well with dCu concentrations of 0.5 to 1.5 nmol L^{-1} measured in the upper 1000 m in the subtropical North Atlantic during the 2010/2011 GEOTRACES NAZT [*Jacquot and Moffett*, 2015; *Roshan and Wu*, 2015].

5.3.3 Particulate δ^{65}Cu profiles

Vertical profiles of particulate δ^{65}Cu at all stations are shown in **Figure 5.6**. The δ^{65}Cu in near-surface samples ranges from -0.49 $\pm$ 0.1‰ to 0.31 $\pm$ 0.1‰, similar to the range of isotopic values observed in North Atlantic aerosols (-0.18 $\pm$ 0.11‰ to 0.30 $\pm$ 0.11‰) [*Dong et al*., 2013; *Little et al*.,

2014a]. Hence, isotopic signature of pCu in surface waters is consistent with atmospheric deposition as the dominant supply of pCu to the upper ocean, as suggested by dissolved Cu profiles.

We observed a subsurface enrichment in δ^{65}Cu up to 1.0‰ at stations 21, 41, and 130 at depths of 60–85 m that appears to largely coincide with the depth of the subsurface fluorescence maximum, where such data is available. This feature is not apparent at station 130, although relatively poor sampling resolution in the top 200 m (n = 2) may have precluded observation of a similar feature in this profile. In deeper waters, δ^{65}Cu values are more variable between stations with measured δ^{65}Cu values of -0.6‰ to +2.6‰. This variability in δ^{65}Cu at depth appears to be a function of particle loading below the surface layer. Vertical profiles of particulate Al and particulate Si at all stations are compared in **Figure 5.7**. Particulate Al concentrations along A16N largely reflect the distribution of lithogenic particles from fluvial input, resuspension of shallow shelf sediments, and atmospheric deposition of mineral aerosols [*Barrett et al.*, 2012]. Particulate Si concentrations also have contributions from lithogenic material, but are largely dominated by production of biogenic opal by diatoms, especially in temperate and sub-polar waters.

Station 41 has the lowest particulate Al (1–2 nmol L^{-1}) and particulate Si (7–35 nmol L^{-1}) concentrations at depth compared to other stations (**Fig. 3.2**). This reflects station location just south of the diatom bloom in the subpolar North Atlantic at the time of sampling (**Appendix, Figure D.1**) and relatively low rates of dust deposition on surface waters in the mid-latitude North Atlantic [*Buck et al.*, 2010]. Low concentrations of both biogenic and lithogenic particles result in minimal scavenging. Average δ^{65}Cu at depths >100 m is relatively constant (-0.10 $\pm$ 0.29‰) and comparable to the average isotopic composition of aerosol sources in the North Atlantic (0.0 $\pm$ 0.2‰) [*Dong et al.*, 2013; *Little et al.*, 2014a]. Hence, at this station, it appears that the isotopic composition of subsurface pCu is controlled by the vertical transport of aerosol particles through the upper water column with little change in δ^{65}Cu values from interactions with dissolved Cu pool (i.e., reversible scavenging).

By contrast, station 21 (55°N) has relatively high concentrations of biogenic particulate Si throughout the upper 1000 m. This signal results from particle export following seasonal diatom productivity in the subpolar North Atlantic [*Barrett et al.*, 2012]. δ^{65}Cu values below 200 m average 1.5 $\pm$ 1.0‰ at this station, compared to average ocean δ^{65}Cu of +0.9‰ [*Little et al.*, 2014b and references therein]. At this station, biogenic particle scavenging in intermediate waters (200–1000 m) appears to sequester isotopically heavy pCu with an average separation factor, $\Delta^{65}Cu_{particle-dissolved}$, of +0.5‰, similar to that observed for biogenic particles in the surface ocean.

Station 107 (10°N) also has a high subsurface particle loading and average subsurface $\delta^{65}Cu$ values of 1.0 ± 0.7‰. Particulate matter at station 107 is heavily impacted by lithogenic, rather than biogenic, particle inputs, as evident from elevated pAl concentrations below 200 m. Intense atmospheric deposition of mineral aerosols on surface waters in the eastern (sub)tropical North Atlantic result in particulate Al concentrations up to 18.3 nmol L^{-1} at station 107 (see discussion in section 3.3.1.1; **Fig. 3.2**). These large lithogenic particle loadings exert strong scavenging pressures on dissolved metals in this region. For example, previous studies have shown that much of the dissolved iron (60–90%) released during organic matter remineralization in these waters is quickly removed from the water column by particle scavenging [*Hatta et al*., 2015]. Observations of low dCu measurements in the upper water column in the eastern North Atlantic are also consistent with high particle scavenging rates in this region [*Jacquot and Moffett*, 2015; *Roshan and Wu*, 2015]. It is more difficult to estimate the magnitude of $\Delta^{65}Cu_{particle-dissolved}$ resulting from particle scavenging using data at low latitudes where the pCu pool at depth is likely to have a significant contribution from isotopically light, insoluble, lithogenic aerosol pCu. However, given that $\delta^{65}Cu$ of the total pCu pool (lithogenic + scavenged) has an average isotopic signature that is equal to or greater than the $\delta^{65}Cu$ of dissolved Cu (+0.9‰), particle scavenging appears to result in preferential sequestration of the heavy ^{65}Cu isotope. Assuming the magnitude of $\Delta^{65}Cu_{particle-dissolved}$ is similar to that observed at station 21 (+0.5‰) implies that ~70% of pCu concentrations at depth result from scavenging of the dissolved pool.

Station 130 (0°N) is located at the southern edge of the region in the tropical North Atlantic that is impacted by the intense plume of mineral aerosols transported from the African continent [*Husar and Prospero*, 1997] and in a region of high spatial gradients in ocean particle loadings [*Barrett et al*., 2012]. Maximum particulate Al concentrations at this station (8.1 nmol L^{-1}) are much lower than those observed at station 107, but elevated compared to other stations along the A16N transect. A feature with isotopically enriched pCu (1.0–1.4‰) is observed at depths of 200–500 m, while $\delta^{65}Cu$ values below 500 m are closer to the average isotopic signature of aerosol source particles (+0.17 ± 0.18‰).

5.4 Discussion

5.4.1 Controls on the isotopic composition of Cu in the ocean

Continental run-off and atmospheric deposition are the primary sources of dissolved Cu to the upper ocean. Riverine inputs deliver isotopically heavy dissolved Cu to the oceans (+0.02 to +1.45‰) relative to the Cu signature of the bulk continental crust (0.16‰) [*Vance et al*., 2008]. By contrast, the average $\delta^{65}Cu$ of aerosol Cu sources (0.0‰) is much closer to the average isotopic signature of crustal

material [*Little et al*., 2014a and references therein]. The similarity between δ^{65}Cu values measured in near-surface particulate samples (-0.49 $\pm$ 0.10‰ to 0.31 $\pm$ 0.10‰) and δ^{65}Cu measured in North Atlantic aerosol samples (-0.18 $\pm$ 0.11‰ to 0.30 $\pm$ 0.11‰) suggests no evidence for isotopic fractionation during dissolution of aerosol Cu in the surface ocean. This is consistent with previous studies which found total aerosol δ^{65}Cu values comparable to the δ^{65}Cu of both dissolved Cu in aerosol leach experiments [*Little et al*., 2014a] and dissolved Cu in natural rainwater samples [*Takano et al*., 2014]. In this regard, Cu isotope cycling appears different from that of other transition metals such as Fe, for which significant isotopic fractionation is observed as a result of aerosol dissolution in the surface ocean [*Conway and John*, 2014].

There is some variation in surface-ocean particulate δ^{65}Cu with latitude. Near-surface samples at station 41 (45°N) are noticeably heavier than in tropical and subpolar surface waters. As discussed above, this station is the least influenced by scavenging processes that appear to result in isotopically heavy particulate Cu. One possible explanation is that the relatively high δ^{65}Cu observed in surface waters at station 41 is due to high inputs from anthropogenic sources. Studies of aerosol trace metal composition along A16N [*Buck et al*., 2010] indicate that aerosol samples in the mid-latitude North Atlantic (~30–50°N) have unique chemical signatures that most likely indicate contributions from anthropogenic emissions. In **Figure 5.8**, surface-ocean particulate δ^{65}Cu is plotted with aerosol vanadium enrichment (relative to Al) and solubility of aerosol Fe, both of which are expected to be higher in aerosols sourced from fossil fuel combustion than lithogenic minerals [*Sholkovitz et al*., 2009]. The direction of the presumed anthropogenic signal is consistent with the conclusions of *Thapalia et al.* [2010], who found heavy δ^{65}Cu in sediment cores indicating increased delivery of anthropogenic Cu.

One previous report of dissolved δ^{65}Cu [*Thompson and Ellwood, 2014*] also measured the isotopic composition of particulate matter from the Pacific. However, high analytical uncertainties and extreme values outside expected natural variability (up to -80‰) limited data interpretation. In the absence of robust measurements of the δ^{65}Cu of marine particulate matter, previous studies have primarily theorized about the magnitude and sign of isotopic fractionation between dissolved and particulate Cu pools using observations of dissolved δ^{65}Cu profiles and experimental studies on the biotic and abiotic processes thought to be possible mechanisms. Proposed hypotheses regarding controls on the δ^{65}Cu of particulate Cu include i) light pCu due to preferential biological uptake of ^{63}Cu, ii) heavy pCu due to preferential abiotic scavenging and adsorption of ^{65}Cu, and iii) light pCu due to preferential binding of ^{65}Cu by strong ligands in seawater.

Experiments investigating both active Cu uptake and surface adsorption by living bacteria have demonstrated preferential sequestration of light ^{63}Cu in biomass (-0.3‰ to -4.4‰ $\Delta^{65}Cu_{particle-dissolved}$)

[*Navarrete et al*., 2011]. Isolated Cu-binding proteins have also been shown to preferentially take up the lighter ^{63}Cu isotope [*Zhu et al*., 2002]. Together, these studies point to Cu isotopic fractionation controlled by active metabolic processes resulting in an isotopically light particulate phase, possibly related to the reduction of Cu (II) to Cu(I) that occurs as part of cellular Cu transport and regulation mechanisms [*Semeniuk et al*., 2015 and references therein]. Reduced Cu(I) has been found to be isotopically lighter than Cu (II) in naturally-occurring minerals, in reduction experiments, and in fractionation induced by oxidative weathering [*Ehrlich et al., 2004*; *Asael et al*., 2007; *Fernandez et al*., 2009]. Hence, if active biological uptake of Cu is the mechanism controlling dissolved-particle Cu fractionation in the ocean, the pCu pool would be isotopically light compared to seawater Cu.

Another possibility is that abiotic scavenging processes dominate isotopic fractionation, which would result in an isotopically heavy pCu phase. Studies have demonstrated that abiotic precipitation of Cu oxy-hydroxides results in isotopic fractionation with enriched $\delta^{65}Cu$ particles up to +2‰ ($\Delta^{65}Cu_{particle-dissolved}$) [*Navarette et al*., 2011]. Heavy ^{65}Cu isotope is preferentially adsorbed onto amorphous and crystalline Fe-oxyhydroxides during equilibrium fractionation with $\Delta^{65}Cu$ of +0.4 to +0.7‰ compared to the dissolved Cu reservoir [*Clayton et al.,* 2005; *Balistrieri et al*., 2008]. Likewise, adsorption onto dead bacteria cells showed a similar fractionation effect with the heavier ^{65}Cu isotope associated with the particulate phase up to +0.7‰ [*Navarrete et al*., 2011]. Previous authors have posited that this fractionation likely results as an effect of the heavy ^{65}Cu ion being thermodynamically stabilized by the stronger bonding environment with fewer, shorter Cu-O bonds formed during adsorption compared to the aqueous $Cu(H2O)_6^{2+}$ complex.

Finally, other authors have hypothesized that the stabilization of the heavy ^{65}Cu isotope in the strong binding environment of the Cu-ligand complex would lead to isotopically light free Cu^{2+} ions in seawater [*Vance et al*., 2008]. *Little et al*. [2014b] observe isotopically light Cu ($\Delta^{65}Cu$ -0.4‰ to -0.6‰) in ocean Fe-Mn crusts compared to source seawater and attribute the apparent seawater-crust isotopic separation to the combined effect of a large, positive $\Delta^{65}Cu$ between ligand-bound and free Cu^{2+} ions and a $\Delta^{65}Cu$ of smaller magnitude and opposite sign between free Cu^{2+} ions and Cu in Fe-Mn crusts.

The particulate $\delta^{65}Cu$ data presented in this work suggests that adsorptive and passive scavenging processes resulting in an isotopically heavy pCu phase are the primary control on isotopic fractionation between the dissolved and particulate Cu pool in the top 1000 m of the ocean. The isotopically heavy particulate matter samples in the euphotic zone have Cu:P ratios that are up to an order of magnitude higher than the expected cellular stoichiometry [*Twining and Baines*, 2013], suggesting the bulk of pCu associated with biogenic particles may be scavenged or adsorbed. The

estimated magnitude of isotopic fractionation (+0.3‰ to +0.5‰) is comparable to experimental observations of isotopic fractionation by abiotic particle processes [*Clayton et al.,* 2005; *Balistrieri et al*., 2008; *Navarette et al*., 2011]. This model is consistent with the hypothesis of *Thompson and Ellwood* [2014] who posited that excursions towards light dissolved δ^{65}Cu values at the deep chlorophyll maximum in the Tasman Sea may indicate the dominance of scavenging processes over biological uptake in controlling variations in seawater δ^{65}Cu in the surface ocean. Our observations also corroborate the conclusion of *Bermin et al*. [2006] that release of isotopically heavy Cu adsorbed to particles is responsible for heavy dissolved δ^{65}Cu in subsurface waters.

Takano et al. [2014] recently presented a series of dissolved δ^{65}Cu profiles from the Pacific and Indian Oceans. Profiles typically showed an increase in dissolved δ^{65}Cu (+0.2‰ to +0.5‰) between the surface ocean and depths of 1000-2000 m. Below 2000 m, dissolved δ^{65}Cu was constant or decreased slightly. The authors hypothesized that the increase in δ^{65}Cu values with depth was primarily due to scavenging of isotopically light Cu. We propose an alternate hypothesis where isotopically heavy Cu is scavenged by particles in the surface layer, the increase in dissolved δ^{65}Cu in the upper 1000 m is due to release of heavy pCu during remineralization of organic particles as proposed by *Bermin et al*. [2006], and δ^{65}Cu values in the deep ocean are controlled by preferential scavenging of ^{65}Cu and/or release of isotopically light Cu from sediments.

In contrast to conclusions of *Little et al.* [2014b], this study of particulate δ^{65}Cu in the upper ocean suggests that particle scavenging processes lead to isotopically heavy pCu even in the presence of organically-bound dCu. There are a number of possible explanations for discrepancies between our observations and the proposed model of *Little et al*. [2014b]. For example, Cu incorporation into Fe-Mn crusts may reflect kinetic isotopic fractionation rather than an equilibrium scavenging process. Alternatively, it is possible that changes in either the character of organic ligands or the scavenging properties of particles may vary between the top 1000 m and the deep ocean. Particulate organic matter plays an important role in scavenging processes in the upper ocean [*Balistrieri et al*., 1981]; higher particulate organic carbon fluxes in the upper ocean may lead to more efficient competition with Cu-binding ligands than in the organic-poor environment surrounding the deep oceanic crusts investigated by *Little et al*. [2014b]. Additionally, recent studies have suggested that weak Cu-binding ligands and rapid, biologically-mediated cycling between dissolved and particulate Cu may play important roles in the cycling of Cu in the upper ocean [*Semeniuk et al*., 2015].

5.4.2 Box model for global surface-ocean Cu

A box model for the surface-ocean dissolved Cu budget is shown in **Figure 5.9**, adapted from the work of *Takano et al*. [2014]. It assumes steady state conditions for the global ocean using the following system of equations to describe the isotopic mass balance of Cu in the surface mixed layer:

$$F_{river} + F_{atmos} + F_{upwell} = F_{downwell} + F_{particle} \quad (5.4)$$

$$F_{river}\delta_{river} + F_{atmos}\delta_{atmos} + F_{upwell}\delta_{upwell} = F_{downwell}\delta_{downwell} + F_{particle}\delta_{particle} \quad (5.5)$$

where F_i and δ_i represent the magnitude and δ^{65}Cu value, respectively, of each input and output flux term. Surface-ocean Cu is supplied by fluvial sources (*river*), atmospheric deposition (*atmos*), and upwelling (*upwell*), and removal of Cu occurs by downwelling (*downwell*) and particle export processes (*particle*). The values assigned to F_{river}, δ_{river}, F_{upwell}, δ_{upwell}, $F_{downwell}$, $\delta_{downwell}$, and δ_{atmos} are based on previous studies (**Table 5.2**) and are discussed briefly below. Where previous studies report estimated errors, we include these in **Table 5.2** as uncertainties in each term and where applicable, the number of observations from which each value is determined. Our best estimate for $\delta_{particle}$ is based on the observations of particulate δ^{65}Cu in this work and values for F_{atmos} and $F_{particle}$ are calculated from the box model isotopic mass balance.

Riverine flux

The global riverine flux of dissolved Cu to the oceans is estimated to be 6–8.7 x 10^8 mol yr^{-1} [*Boyle et al*., 1977; *Gaillerdet et al*., 2003; *Vance et al*., 2008]. A discharge-weighted average value of 7.2 x 10^8 mol yr^{-1} is used for mass balance calculations. The δ^{65}Cu of riverine inputs is assigned a value of 0.68‰ based on the work of *Vance et al*. [2008] that determined a discharge-weighted average dissolved δ^{65}Cu using measurements from rivers representing ~25% of the total global riverine discharge to the oceans.

Upwelling and downwelling Cu fluxes

The model assumes a mixing rate of 1.2 x 10^{15} m^3 yr^{-1} between the surface layer and deep ocean [*Sarmiento and Gruber*, 2006]. The upwelling flux to the surface ocean is estimated assuming a deep-ocean Cu reservoir with an average dissolved Cu concentration of 2.5 nmol L^{-1} [*Takano et al*., 2014] and

average global seawater δ^{65}Cu (+0.9‰) [*Little et al*., 2014b]. The downwelling flux is calculated using a global average surface-ocean dissolved Cu concentration of 1.1 nmol L^{-1} [*Takano et al*., 2014] and a δ^{65}Cu value of 0.6‰, representing the average of all previously-reported surface ocean (<100 m) dissolved Cu isotopic measurements (**Figure 5.10**).

Particulate Cu flux

The isotopic composition of the surface ocean particulate Cu pool is assigned a value of 0.95‰, the average δ^{65}Cu at the depth of the subsurface isotopic enrichment observed at stations 21, 41, and 107. Based on available fluorescence data, this feature appears at the depth of the subsurface fluorescence max where particulate Cu is assumed to be primarily biogenic, originating from the bioavailable dissolved Cu pool. This assumption is supported by studies that observe low concentrations of lithogenic particles at the depth of the subsurface chlorophyll maximum [*Barrett et al*., 2012; *Ohnemus and Lam*, 2015] due to rapid aggregation and sinking in the surface ocean. This "lithogenic shadow zone" has been found to be a major feature in one-dimensional models of lithogenic particle fluxes [*Ohnemus and Lam*, 2015]. However, if lithogenic Cu represents a significant portion of particulate Cu at these depths, the δ^{65}Cu of dissolved Cu removed via particle processes would be isotopically heavier than estimated in our model. Hence, a value of 0.95‰ reflects a conservative estimate of the isotopic fractionation induced by dissolved-particulate interactions.

The magnitude of the particulate Cu flux out of the surface ocean is calculated from the isotopic mass balance in equations 5.4 and 5.5 and is estimated to be 2.6 x 10^9 mol yr^{-1}, ranging from 2.2 x 10^9 to 3.1 x 10^9 mol yr^{-1} within known uncertainties for input values indicated in **Table 5.2.** Estimates for global ocean carbon export generally range from 5 to 13 Pg C yr^{-1} [*Boyd and Trull*, 2007; *Dunne et al*., 2007; *Henson et al*., 2011; *Siegel et al*., 2014]. Comparing the range of our calculated particulate Cu flux to the equivalent organic P flux using a C:P ratio of 106:1 for organic matter yields a Cu:P ratio of 0.2–0.8 mmol mol^{-1} in sinking particles. This ratio is comparable to reported Cu:P ratios of 0.2–2.1 mmol mol^{-1} for phytoplankton and bulk particle samples [*Twining and Baines*, 2013 and references therein], giving confidence that the magnitude of our calculated Cu particle flux is a reasonable estimate.

Aerosol Cu flux

A value of 0‰ is assumed for the Cu isotopic composition of aerosol Cu inputs to the surface ocean based on measurements of δ^{65}Cu of Cu in Atlantic marine aerosols (n = 8) [*Dong et al*., 2013; *Little et al*., 2014a]. The aerosol Cu flux calculated from the isotopic mass balance in equations 5.4 and 5.5 is

1.2 x 10^8 mol yr^{-1}. The magnitude of this flux estimate is relatively more sensitive to the range of known uncertainties of input values (**Table 5.2**) and tuning calculations within the full range of error estimates results in negligible aerosol Cu inputs to fluxes up to 7.9 x 10^8 mol yr^{-1}. **Table 5.3** compares our value to other recent estimates for atmospheric deposition of soluble Cu on the global surface ocean. *Little et al*. [2014a] calculate an atmospheric Cu flux of 5.4 x 10^7 mol yr^{-1} using a global dust deposition rate of 450 Mt yr^{-1} [*Jickells et al*., 2005], an average composition of continental crust (28 ppm Cu) [*Rudnick and Gao*, 2003], and a solubility of 27% for aerosol Cu [*Desboeufs et al*., 2005]. Our estimate is approximately twice as large as that of *Little et al*. [2014a], possibly due to the presence of anthropogenic Cu sources, which have higher concentrations of highly soluble aerosol Cu compared to natural lithogenic dust [*Sholkovitz et al*., 2010; *Shelley et al.*, 2015]. However, our best estimate for atmospheric Cu inputs is still almost an order of magnitude lower than the aerosol Cu flux of 9.6 x 10^8 mol yr^{-1} recently reported by *Takano et al*. [2014] from an isotopic mass balance model for surface-ocean Cu. These authors suggest that their high estimate compared to previous studies is largely a result of implicit inclusion of potentially large anthropogenic sources, or possibly due to unaccounted-for fluxes from continental shelf sediments. However, their assumption that no isotopic fractionation occurs as a result of particle-mediated processes in the surface ocean would lead to overestimation of the aerosol Cu inputs. Hence, the estimate of *Takano et al*. [2014] should be considered an upper limit on atmospheric-ocean Cu fluxes.

5.5 Conclusions

We present some of the first observations of the Cu stable isotope composition of particulate matter in the upper water column, which indicate that passive adsorptive and scavenging processes likely dominate the dissolved-particle partitioning of Cu in the upper ocean. Isotopic enrichment relative to average surface seawater dissolved $\delta^{65}Cu$ suggests that particle-mediated processes in the surface ocean result in isotopically heavy pCu with a separation factor ($\Delta^{65}Cu_{particle-dissolved}$) of +0.3‰ to +0.5‰. Using a modified box model for the surface-ocean Cu isotopic mass balance that takes into account an isotopically heavy particle sink, we estimate a flux of soluble Cu of 1.2 x 10^8 mol yr^{-1} from atmospheric deposition. The magnitude of this aerosol flux compared to estimates accounting only for deposition of lithogenic mineral dust implies that anthropogenic Cu aerosol sources to the upper ocean are significant and on the order of natural inputs as suggested by *Duce et al*. [1991]. Our small initial sample set of surface-ocean particulates may indicate that anthropogenic trace metal emissions may have a heavier $\delta^{65}Cu$ signature as suggested by *Thapalia et al.* [2010]. Increased aerosol Cu transport and deposition on

the surface ocean from anthropogenic combustion emissions has been suggested to impact modern marine ecosystem productivity and community structure [*Paytan et al*., 2009]. Variation in the isotopic signature of seawater Cu could be a useful tool to assess that importance of anthropogenic sources to ocean Cu budgets, but further analysis of a more extensive sample set is required.

5.6 Appendix

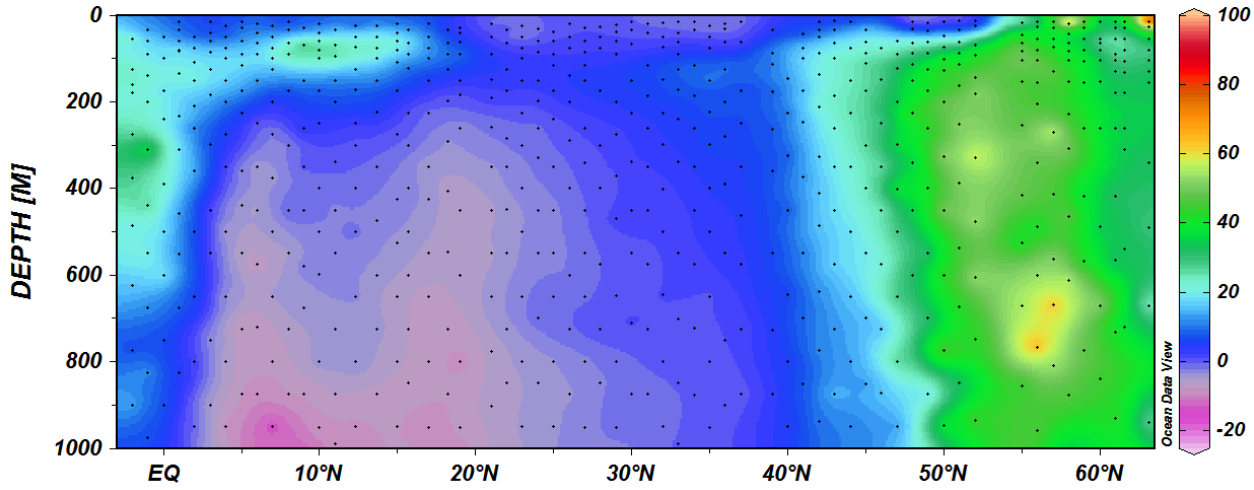

Figure D.1. Distributions of biogenic particulate Si (in nmol L^{-1}) along the CLIVAR A16N transect in 2013. The biogenic fraction of measured particulate Si concentrations is determined by normalizing to particulate Al, a proxy for lithogenic particle inputs**.**

5.7 References

Asael, D., Matthews, A., Bar-Matthews, M., Halicz, L., 2007. Copper isotope fractionation in sedimentary copper mineralization (Timna Valley, Israel). Chem. Geol. 243, 238–254.

Balistrieri, L., Brewer, P.G., Murray, J.W., 1981. Scavenging residence times of trace metals and surface chemistry of sinking particles in the deep ocean. Deep Sea Res. 28, 101–121.

Balistrieri, L.S., Borrok, D.M., Wanty, R.B., Ridley, W.I., 2008. Fractionation of Cu and Zn isotopes during adsorption onto amorphous Fe(III) oxyhydroxide: Experimental mixing of acid rock drainage and ambient river water. Geochim. Cosmochim. Acta 72, 311–328.

Barrett, P.M., Resing, J.A., Buck, N.J., Buck, C.S., Landing, W.M., Measures, C.I., 2012. The trace element composition of suspended particulate matter in the upper 1000 m of the eastern North Atlantic Ocean: A16N. Mar. Chem. 142–144, 41–53.

Bermin, J., Vance, D., Archer, C., Statham, P.J., 2006. The determination of the isotopic composition of Cu and Zn in seawater. Chem. Geol. 226, 280 – 297.

Boyd, P.W., Trull, T.W., 2007. Understanding the export of marine biogenic particles: Is there consensus? Prog. Oceanogr. 72, 276–312.

Boyle, E.A., Sclater, F.R., Edmond, J.M., 1977. Distribution of dissolved copper in the Pacific. Earth Planet. Sci. Lett. 37, 38–54.

Bruland, K.W., Lohan, M.C., 2003. Controls of trace metals in seawater. in *Treatise on Geochemistry*. Holland, H.D., K.K. Turkekian.

Buck, C.S., Landing, W.M., Resing, J.A., Measures, C.I., 2010. The solubility and deposition of aerosol Fe and other trace elements in the North Atlantic Ocean: observations from the A16N CLIVAR/CO_2 repeat hydrography section. Mar Chem. 120, 57–70.

Clayton, R.E., Hudson-Edwards, K.A., Houghton, S.L., 2005. Isotopic effects during Cu adsorption onto goethite. Geochim. Cosmochim. Acta 69, A216.

Coale, K.H., Bruland, K.W., 1988. Copper complexation in the Northeast Pacific. Limnol. Oceanogr. 33, 1084–1101.

Coale, K.H., Bruland, K.W., 1990. Spatial and temporal variability in copper complexation in the Northeast Pacific. *Deep-Sea Res*., 37, 317–336.

Conway, T.M., John, S.G., 2014. Quantification of dissolved iron sources to the North Atlantic Ocean. Nature 511, 212–215.

Desboeufs, K.V., Sofikitis, A., Losno, R., Colin, J.L., Ausset, P., 2005. Dissolution and solubility of trace metals from natural and anthropogenic aerosol particulate matter. Chemosphere 58, 195–203.

Dong, S., Weiss, D.J., Strekopytov, S., Kreissig, K., Sun, Y., Baker, A.R., Formenti, P., 2013. Stable isotope ratio measurements of Cu and Zn in mineral dust (bulk and size fractions) from the Taklimakan Desert and the Sahel and in aerosols from the eastern tropical North Atlantic. Talanta 114, 103–109.

Duce et al., 1991. The atmospheric input of trace species to the world ocean. *Global Biogeochem. Cycles*, 5, 193–259.

Dunne, J.P., Sarmiento, J.L., Gnanadesikan, A., 2007. A synthesis of global particle export from the surface ocean and cycling through the ocean interior and on the seafloor. Global Biogeochem. Cycles 21, GB4006.

Ehlrich, S., Butler, I., Halicz, L., Rickard, D., Oldroyd, A., Matthews, A., 2004. Experimental study of the copper isotope fractionation between aqueous Ci(II) and covellite, CuS. Chem. Geol. 209, 259–269.

Fernandez, A., Borrok, D.M., 2009. Fractionation of Cu, Fe, and Zn isotopes during oxidative weathering of sulfide-rich rocks. Chem. Geol. 264, 1–12.

Gaillerdet, J., Viers, J., Dupré, B., 2003. Trace elements in river waters. Treatise Geochem. 5, 225–272.

Hatta, M., Measures, C.I., Wu, J., Roshan, S., Fitzsimmons, J.N., Sedwick, P., Morton, P., 2015. An overview of dissolved Fe and Mn Distributions during the 2010–2011 U.S. GEOTRACES North Atlantic Cruises: GEOTRACES GA03. Deep-Sea Res. II 116, 117–129.

Henson, S.A., Sandres, R., Madsen, E., Morris, P.J., Le Moigne, F., Quartly, G.D., 2011. A reduced estimate of the strength of the ocean's biological carbon pump. Geophys. Res. Lett. 38, L04606.

Husar, R., Prospero, J., 1997. Characterization of tropospheric aerosols over the oceans with the NOAA advanced very high resolution radiometer optical thickness operational product. J. Geophys. Res. 102, 16899–16909.

Jacquot, J.E., Moffett, J.W., 2015. Copper distribution and speciation across the International GEPTRACES Section GA03. Deep-Sea Res. II 116, 187–207.

Jickells, T., An, Z., Andersen, K.K., Baker, A., Bergametti, G., Brooks, N., Cao, J., Boyd, P., Duce, R., Hunter, K., Kawahata, H., Kubilay, N., laRoche, J., Liss, P.S., Mahowald, N., ProsperoJ.M., Ridgwell, A.J., Tegen, I., Torres, R., 2005. Global iron connections between desert dust, ocean biogeochemistry, and climate. Science 308, 67–71.

Kuss, K., Kremling, K., 1999. Spatial variability of particle associated trace elements in near-surface waters of the North Atlantic (30°N/60°W to 60°N/2°W), derived by large volume sampling. Mar. Chem. 68, 71–86.

Little, S.H., Vance, D., Siddall, M., Gasson, E., 2013. A modelling assessment of the role of reversible scavenging in controlling oceanic dissolved Cu and Zn distributions. Global Biogeochem. Cycles 27, 780–791.

Little, S.H., Vance, D., Walker-Brown, C., Landing, W.M., 2014a. The oceanic mass balance of copper and zinc isotopes, investigated by analysis of their inputs, and outputs to ferromanganese oxide sediments. Geochim. Cosmochim. Acta 125, 673–693.

Little, S.H, Sherman, D.M., Vance, D., Hein, J.R., 2014b. Molecular controls on Cu and Zn isotopic fractionation in Fe-Mn crusts. Earth Planet. Sci. Lett. 396, 213–222.

Mann, E.L., Ahlgren, N., Moffett, J.W., Chisholm, S.W., 2002. Copper toxicity and cyanobacteria ecology in the Sargasso Sea. Limnol Oceanogr. 47 976–988.

Maréchal, C.N., Télouk, P., Albarède, F., 1999. Precise analysis of copper and zinc isotopic compositions by plasma-source mass spectrometry. Chem. Geol. 156, 251–273.

Mathur, R., Ruiz, J., Titley, S., Liermann, L., Buss, H., Brantley, S., 2005. Cu isotopic fractionation in the supergene environment with and without bacteria. Geochim. Cosmochim. Acta 69, 5233–5246.

Measures, C. I., Landing, W.M., Brown, M.T., Buck, C.S., 2008. A commercially available rosette system for trace metal-clean sampling. Limnol. Oceanogr. Methods 6, 384–394.

Milne, A., Landing, W.M., Bizimis, M., Morton, P.L., 2010: Determination of Mn, Fe, Co, Ni, Cu, Zn, Cd and Pb in seawater using high resolution magnetic sector inductively coupled mass spectrometry (HR-ICP-MS). Anal. Chim. Acta 665, 200–207.

Moffett, J.W., Brand, L.E., 1996. Production of strong, extracellular Cu chelators by marine cyanobacteria in response to Cu stress. Limnol. Oceanogr. 41, 388–395.

Moffett, J.W., Dupont, C., 2007. Cu complexation by organic ligands in the sub-arctic NW Pacific and Bering Sea. Deep-Sea Res. I 54, 586–595.

Morel, F.M.M., Milligan, A.J., Saito, M.A., 2003. Marine bioinorganic chemistry: The role of trace metals in the oceanic cycles of major nutrients. Treatise Geochem. 6, 113–143.

Navarrete, J.U., Borrok,, D.M., Viveros, M., Ellzey, J.T., 2011. Copper isotope fractionation during surface adsorption and intracellular incorporation by bacteria. Geochim. Cosmochim. Acta 75, 784–799.

Ohnemus, D.C., Lam, P.J., 2015. Cycling of Lithogenic Marine Particles in the US GEOTRACES North Atlantic Transect. Deep-Sea Res. II 116, 283–302.

Paytan, A., Mackey, K.R.M., Chen, Y., Lima, Y.D., Doney, S.C., Mahowald, N., Labiosa, R., Post, A.F., 2009. Toxicity of atmospheric aerosols on marine phytoplankton. Proc. Nat. Acad. Sci. 106, 4601–4605.

Roshan, S., Wu, J., 2015. The distribution of dissolved copper in the tropical-subtropical north At;antic across the GEOTRACES GA03 transect. Mar. Chem. 176, 189–198.

Rudnick, R., Gao, S., 2003. Composition of the continental crust. Treatise Geochem. 3, 1–64.

Sarmiento, J.L., Gruber, N., 2006. Ocean Biogeochemical Dynamics. Princeton University Press.

Semeniuk, D.M., Bundy, R.M., Payne, C.D., Barbeau, K.A., Maldanado, M.T., 2015. Acquisition of organically complexed copper by marine phytoplankton and bacteria in the northeast subarctic Pacific Ocean. Mar. Chem. 173, 222–233.

Shelley, R.U., Morton, P.L., Landing, W.M., 2015. Elemental ratios and enrichment factors in aerosols from the US-GEOTRACES North Atlantic transects. Deep-Sea Res. II 116, 262–272.

Sholkovitz, E.R., Sedwick, P.N., Church, T.M., 2009. Influence of anthropogenic combustion emissions on the deposition of soluble aerosol iron to the ocean: Empirical estimates for island sites in the North Atlantic. Geochim. Cosmochim. Acta 73, 3981–4003.

Sholkovitz, E.R., Sedwick, P.N., Church, T.M., 2010. On the fractional solubility of copper in marine aerosols: Toxicity of aeolian copper revisited. Geophys. Res, Lett. 37, L20601.

Siegel, D.A., Buesseler, K.O., Doney, S.C., Sailley, S.F., Behrenfeld, M.J., Boyd, P.W., 2014. Global assessment of ocean carbon export by combining satellite observations and food-web models. Global Biogeochem. Cycles 28, 181–196.

Stramma, L., England, M., 1999. On the water masses and mean circulation of the South Atlantic Ocean. J. Geophys. Res. 104, 20863–20883.

Sunda W.G., Guillard R.R.L., 1976. The relationship between cupric ion activity and the toxicity of copper to phytoplankton. J. Mar. Res. 37, 761–777.

Takano, S., Tanimizu, M., Hirata, T., Sohrin, T., 2014. Isotopic constraints on biogeochemical cycling of copper in the ocean. Nature Comm., 5, doi:10.1038/ncomms6663.

Thapalia, A., Borrok, D.M., Van Metre, P.C., Musgrove, M., Landa, E.R., 2010. Zn and Cu isotopes as tracers of anthropogenic contamination in a sediment core from an urban lake. Environ. Sci. Tech. 44, 1544–1550.

Thompson, C.M., Ellwood, M.J., Willies, M., 2013. A solvent extraction technique for the isotopic measurement of dissolved copper in seawater. Anal. Chim. Acta 125, 106–113.

Thompson, C.M., Elwood, M.J., 2014. Dissolved copper isotope biogeochemistry in the Tasman Sea, SW Pacific Ocean. Mar. Chem. 165, 1–9.

Twining, B.S., Baines, S.B., 2013. The trace metal composition of marine phytoplankton. Ann. Rev. Mar. Sci. 5, 191–215.

Twining, B.S., Rauschenberg, S., Morton, P.L., Vogt, S., 2015. Metal contents of phytoplankton and labile particulate material in the North Atlantic Ocean. Prog. Oceanogr. 137, 261–283.

Vance, D., Archer, C., Bermin, J., Perkins, J., Statham, P.J., Lohan, M.C., Ellwood, M.J., Mills, R.A., 2008. The copper isotope geochemistry of rivers and the oceans. Earth. Planet. Sci. Lett. 274, 204 – 213.

Wanninkhof, R., Doney, S.C., Bullister, J.L.,. Levine, N.M., Warner, M., Gruber, N., 2010. Detecting anthropogenic CO2 changes in the interior Atlantic Ocean between 1989 and 2005. J. Geophys. Res. 115, C11028.

Zhu, X.K., Guo, Y., Williams, R.J.P., O'Nions, R.K., Matthews, A., Belshaw, N.S., Canters, G.W., de Waal, E.C., Weser, U., Burgess, B.K., Salvato, B., 2002. Mass fractionation of transition metal isotopes. Earth Planet. Sci. Lett. 200, 47–62.

Table 5.1. Typical MC ICP-MS typical operating conditions and cup configurations

NuPlasma						
RF power				1300 W		
nebulizer pressure				30–32 psi		
membrane gas flow rate				2.9–3.0 L min^{-1}		
hot gas flow rate				0.4–0.5 L min^{-1}		
integration time				10 s		
cycles				30		
cup configuration	H5	H4	H2	axial	L2	L3
	68	67	66	65	64	63

Table 5.2. Isotopic composition and mass flux for each term in box model for Cu cycling in the surface ocean. Where reported, estimated error for each value is given in parentheses (± 1 SD) and number of observations is indicated below the average value. Values in bold are calculated from isotopic mass balance equations.

		δ^{65}Cu (‰)	reference	Cu flux (10^9 mol yr^{-1})	reference
Inputs	Rivers	0.68	*Vance et al*. [2008]	0.72 (0.14)	*Boyle et al.* [1977] *Gaillerdet et al.* [2003] *Vance et al*. [2008]
	Atmosphere	0.0 (0.2) (n = 8)	*Dong et al.* [2013] *Little et al*. [2014a]	**0.12**	this work
	Upwelling	0.9	*Little et al*. [2014a]	3.0	*Takano et al*. [2014]
Outputs	Downwelling	0.6 (0.2) (n = 35)	*Vance et al*. [2008] *Boyle et al.* [2012] *Takano et al*. [2014] *Thompson and Ellwood* [2014]	1.3	*Takano et al*. [2014]
	Particulate	0.95 (0.07) (n = 4)	this work	**2.6**	this work

Table 5.3. Summary of estimates of input of soluble Cu from atmospheric deposition of aerosol Cu on the global ocean.

reference	global atmospheric input of soluble Cu (mol yr^{-1})
Duce et al. [1991]	2.2–7.1 x 10^8
Little et al. [2014a]	0.5 x 10^8
Takano et al. [2014]	9.6 x 10^8
this work	1.2 x 10^8

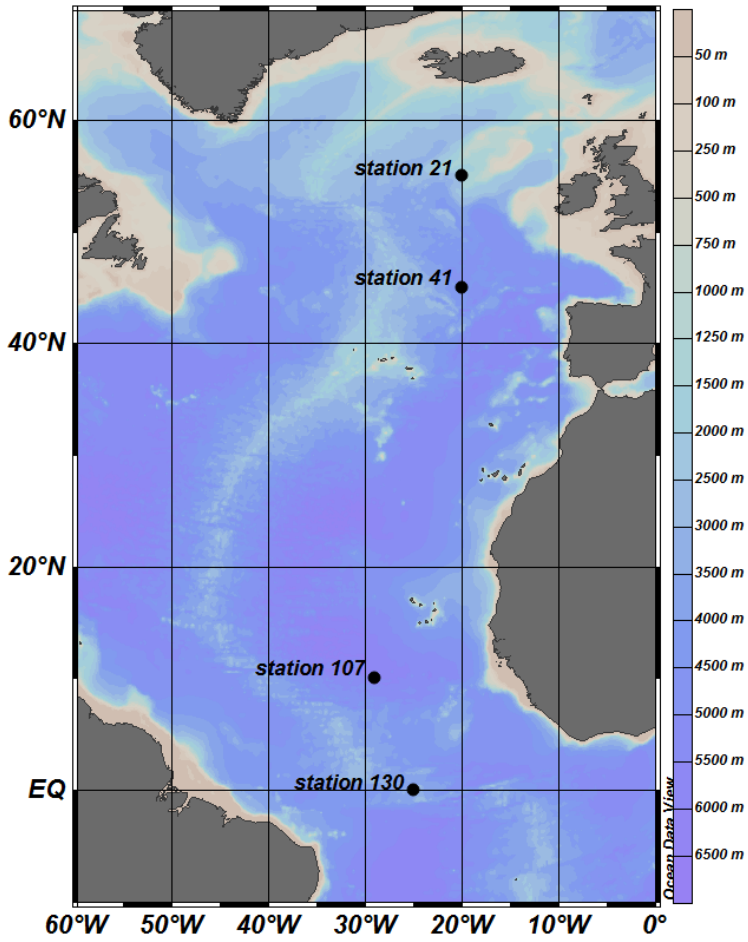

Figure 5.1. Location of δ^{65}Cu sampling stations along A16N.

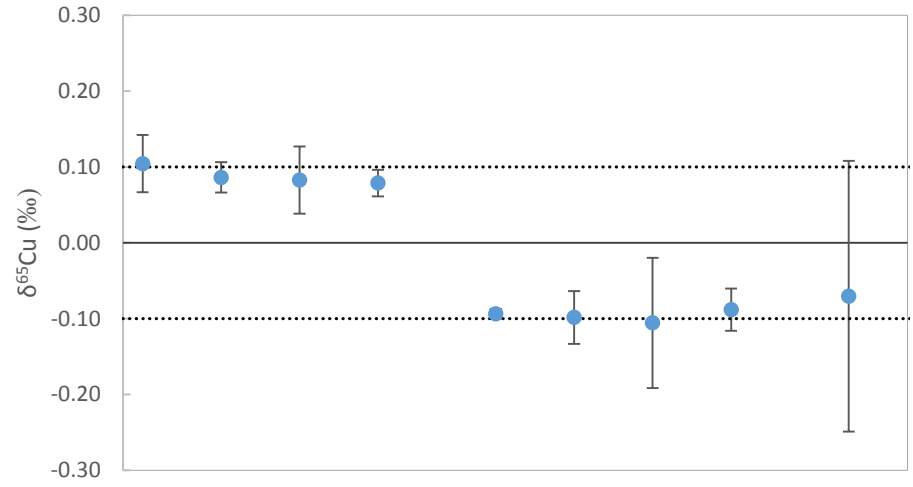

Figure 5.2. Analysis of in-house Claritas PPT Cu standard run through the anion exchange columns (n=9) reported as δ^{65}Cu relative to measured isotopic composition of untreated Claritas standard using standard-sample bracketing. Error bars represent standard deviation on duplicate measurements. Dotted lines represent precision of the analytical method as determined from the variability of in-house standard (±0.10‰, 2 standard deviation).

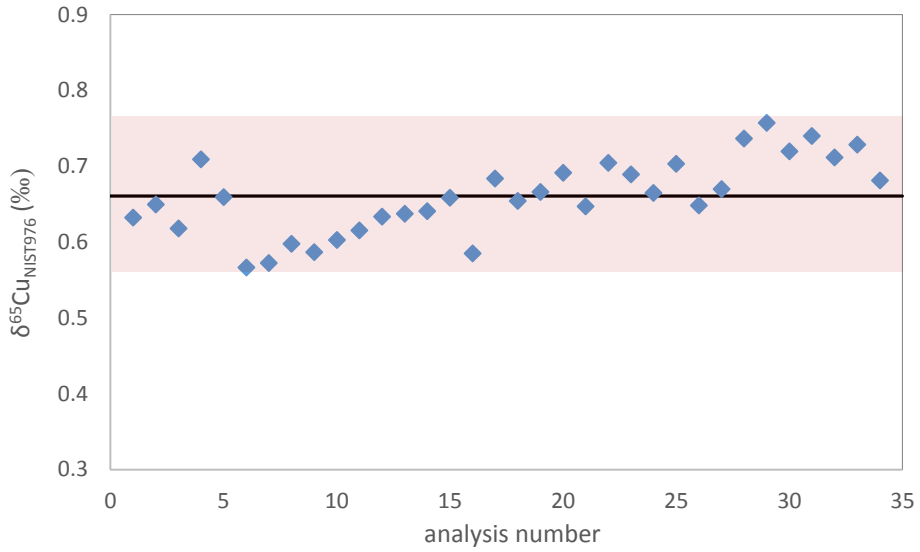

Figure 5.3. Variability of in-house Claritas PPT Cu standard reported relative to NIST 976 shown as mean bounded by 2 standard deviations (0.67 ± 0.10‰).

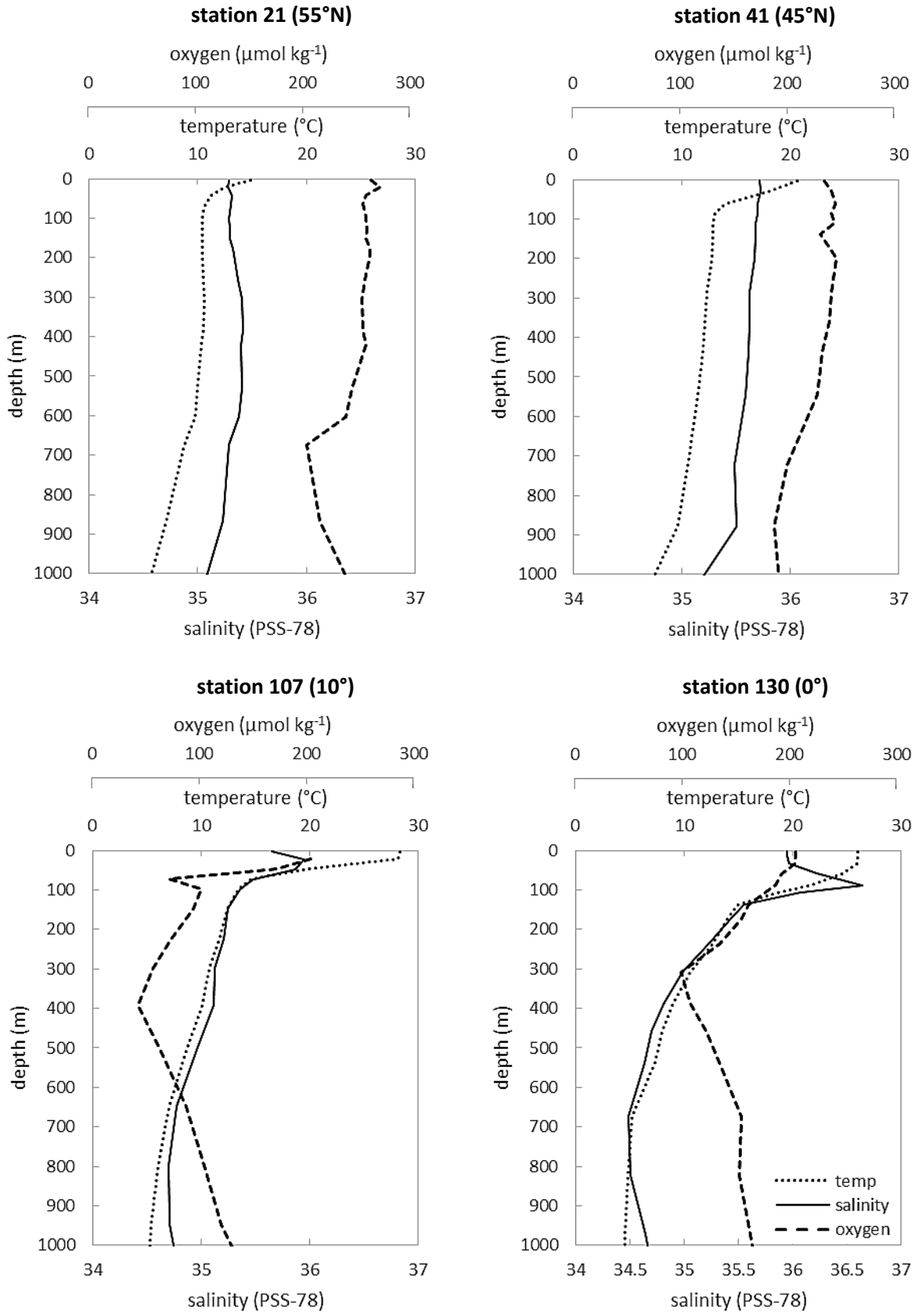

Figure 5.4. Salinity (solid line), temperature (dotted line), and dissolved oxygen (dashed line) at stations 21 (55°N, 20°W), 41 (45°N, 20°W), 107 (10°N, 29°W), and 130 (0°N, 25°W) along CLIVAR A16N in 2013. Legend shown for station 130 is the same for all stations.

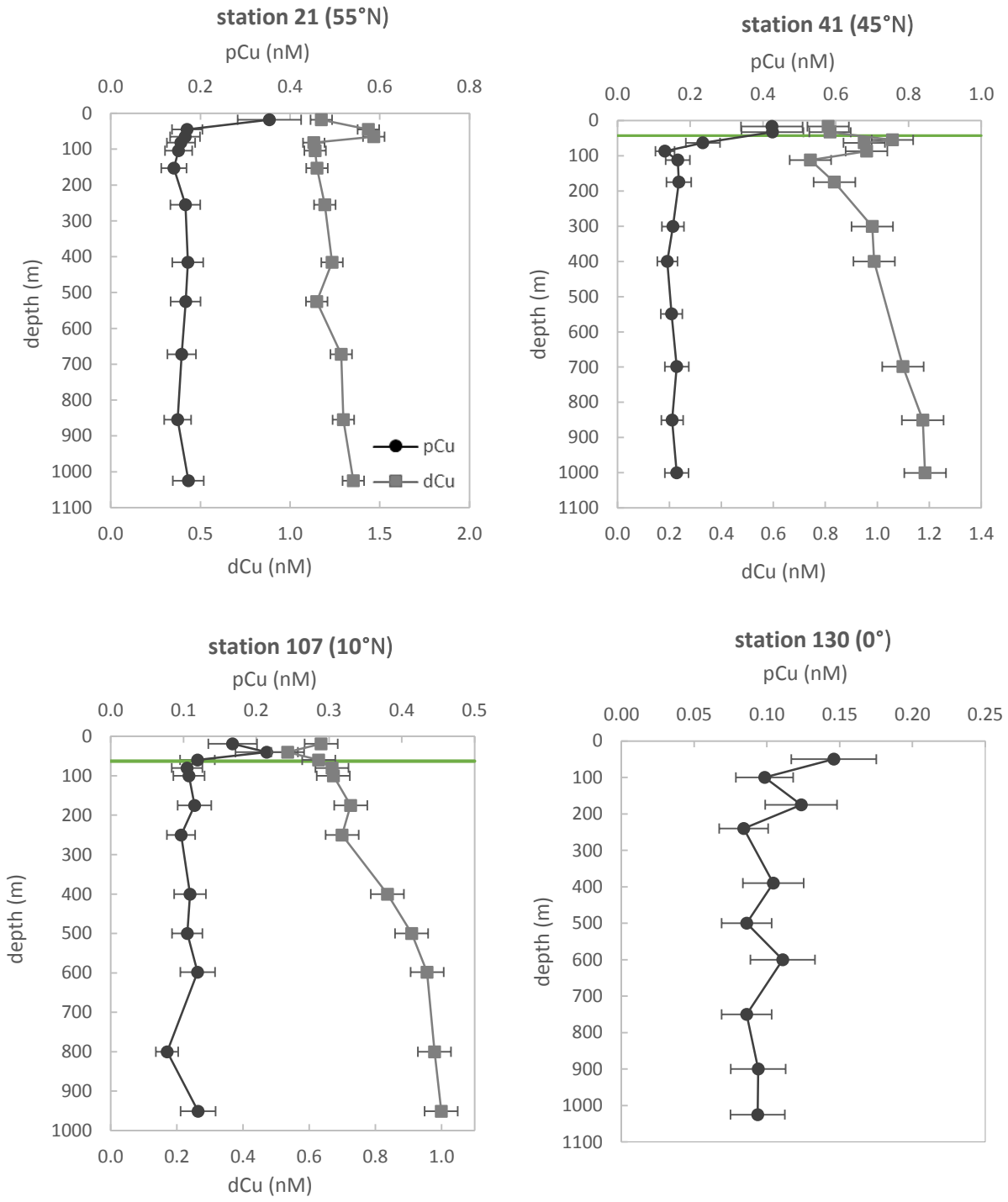

Figure 5.5. Distributions of particulate Cu (black circles) and dissolved Cu (grey squares) in nmol L^{-1} stations 21 (55°N), 41 (45°N), 107 (10°N), and 130 (0°) along the 2013 A16N transect; dissolved Cu data is not available for station 130. Note scale changes for each figure. Solid green lines indicate the approximate depth of the subsurface fluorescence maximum at stations where data is available. Legend shown for station 21 is the same for all stations.

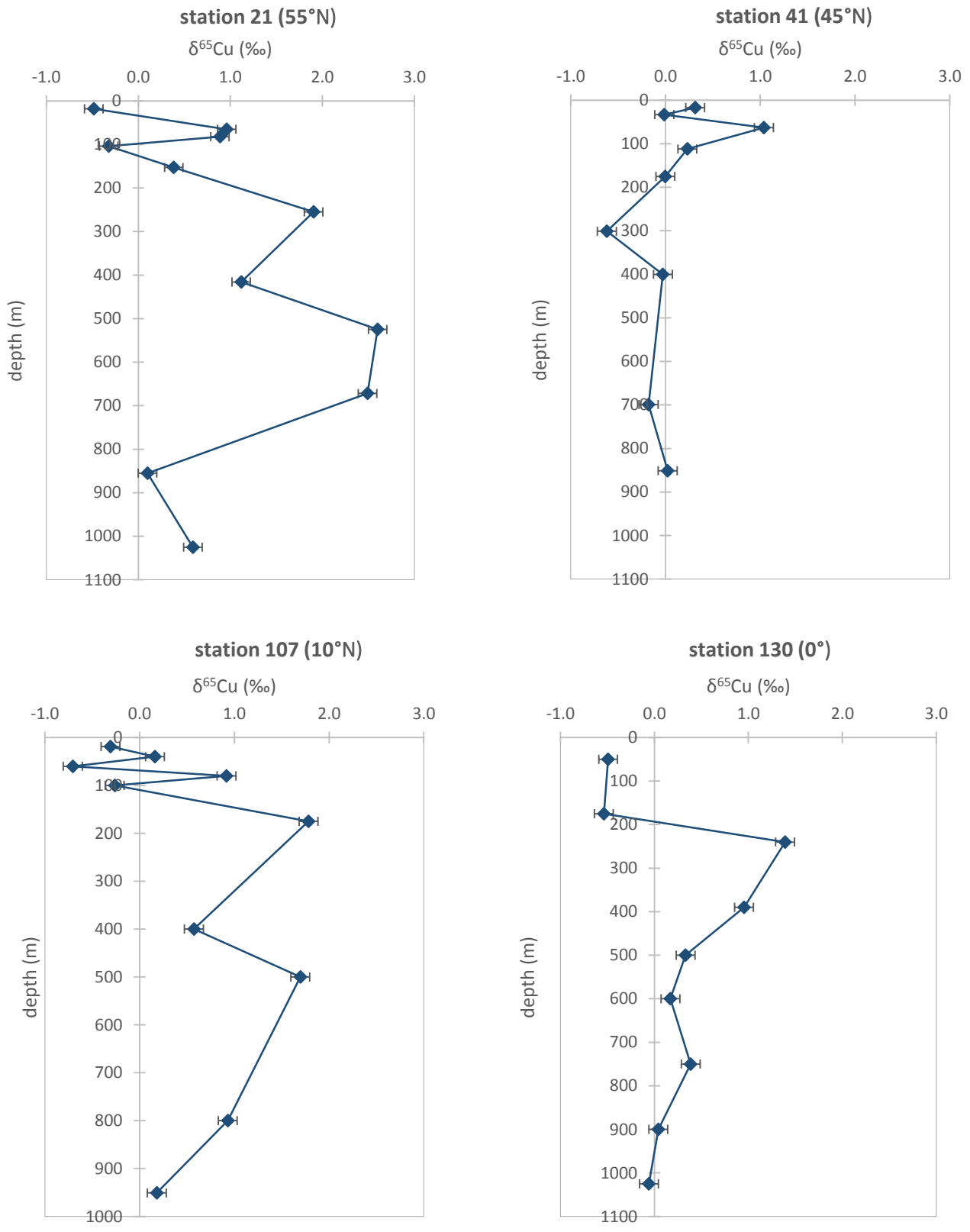

Figure 5.6. Particulate $\delta^{65}Cu$ (‰) at stations 21 (55°N), 41 (45°N), 107 (10°N), and 130 (0°) along the 2013 A16N transect. Error bars indicate ± 2 standard deviations (0.1‰)

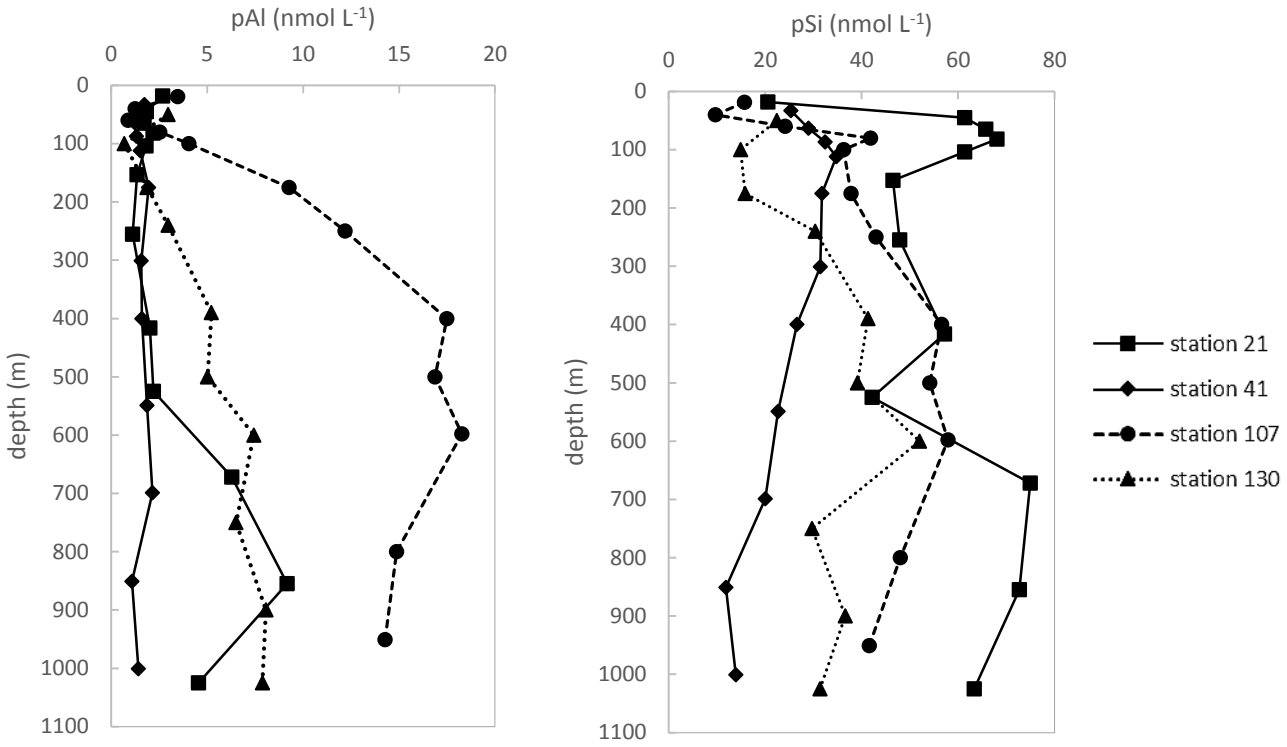

Figure 5.7. Concentrations of particulate Al, Si, and P (nmol L^{-1}) at A16N stations 21 (squares), 41 (diamonds), 107 (circles), and 130 (circles).

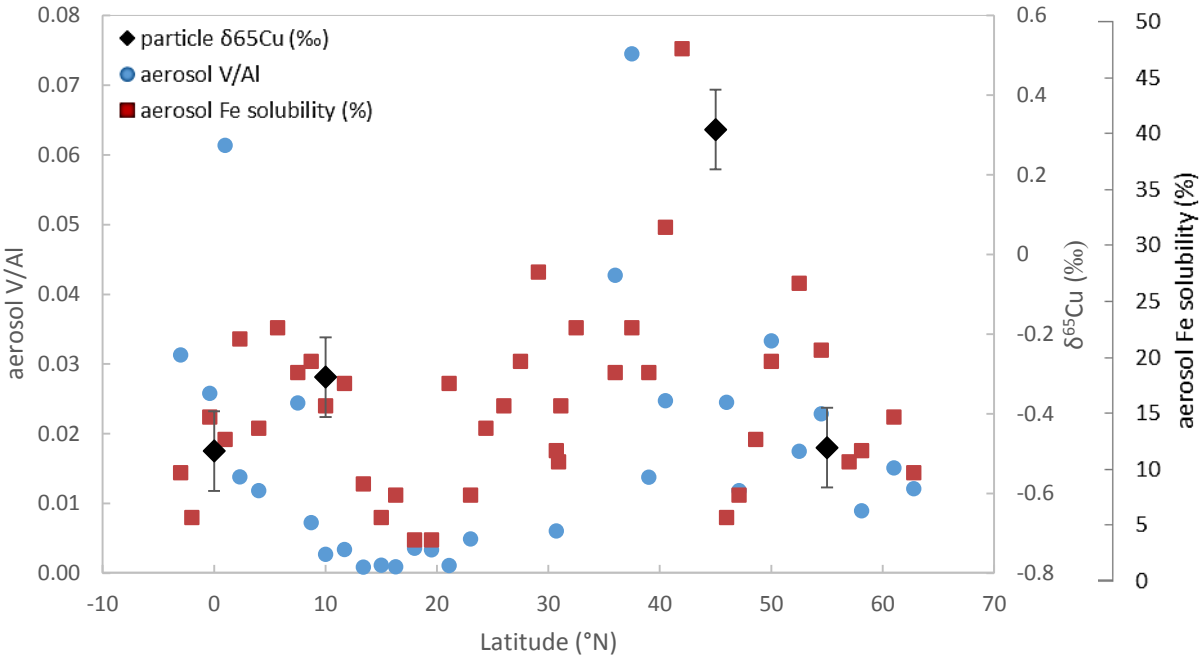

Figure 5.8. δ^{65}Cu of surface-ocean particulate matter samples at 4 stations along CLIVAR A16N (black diamonds) plotted with aerosol V/Al ratios (blue circles) and solubility of aerosol Fe (red squares) in shipboard aerosol samples collected along A16N in 2003 [*Buck et al.*, 2010].

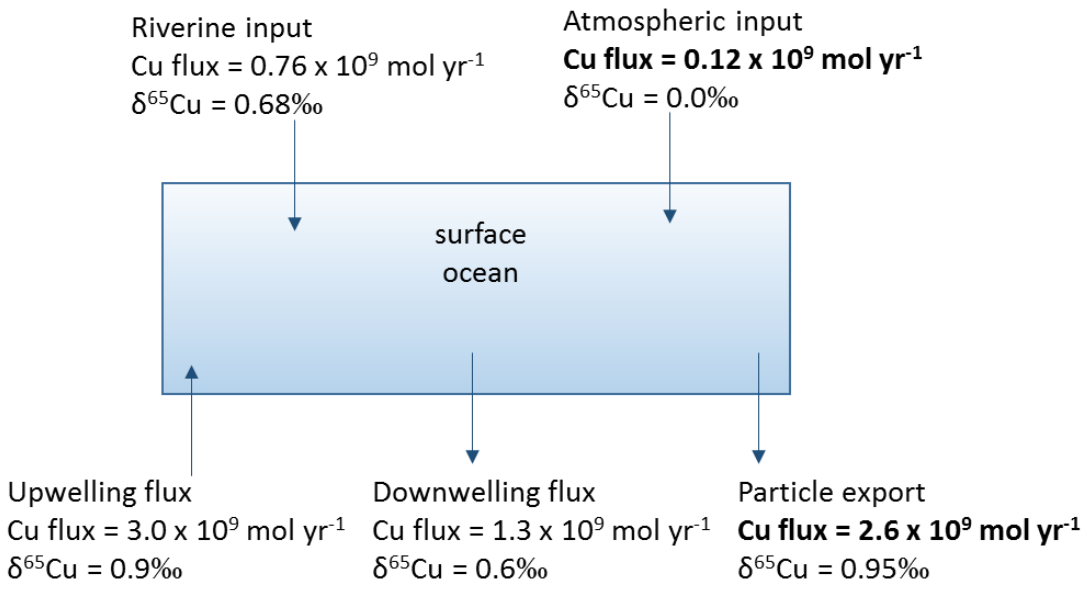

Figure 5.9. Box model for surface-ocean Cu fluxes, adapted from *Takano et al*. [2014]. Values in bold are calculated from the isotopic mass balance.

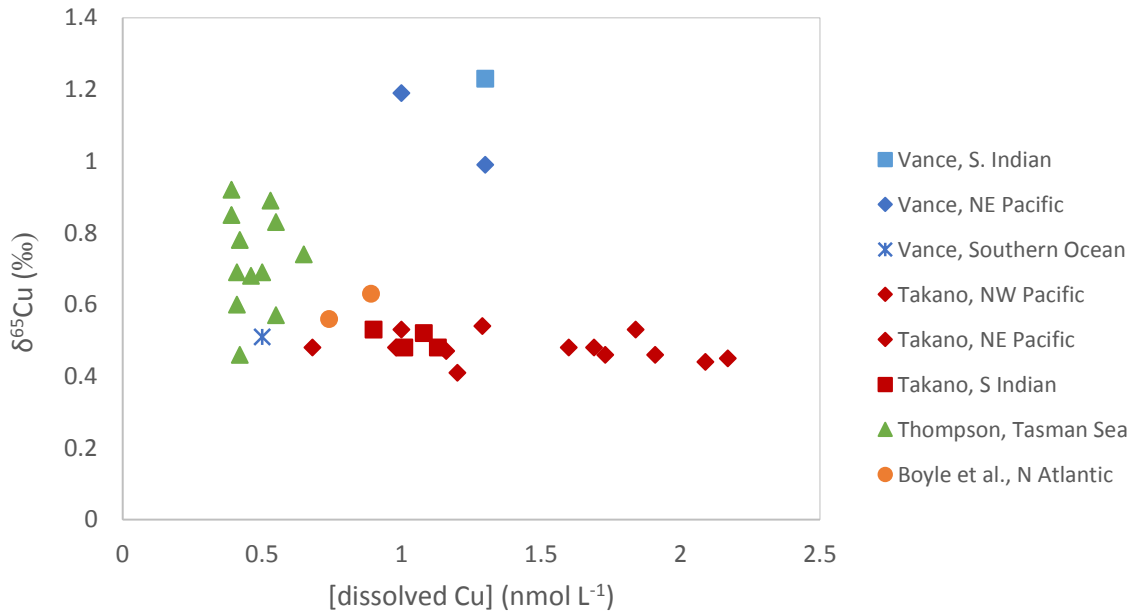

Figure 5.10. Surface-ocean (<100 m) dissolved δ^{65}Cu plotted against Cu concentration using data from *Vance et al*. [2008] (blue), *Boyle et al*. [2012] (orange), *Takano et al*. [2014] (red), and *Thompson and Ellwood* [2014] (green) from the North Pacific Ocean (♦), South Indian Ocean (■), Tasman Sea (▲), Southern Ocean (*), and North Atlantic Ocean (●).

Vita

Education

Ph.D. Chemical Oceanography, 2015
Graduate Certificate in Climate Science, 2014
M.S. Chemical Oceanography, 2012
University of Washington, Seattle, WA

Teaching Credential, Secondary Science, 2009
San Francisco State University, San Francisco, CA

B.S. Chemistry and B.A. Political Science, 2006
University of Rochester, Rochester, NY

Awards

2013–2015	NSF-IGERT Graduate Fellowship
2014	Dean A. McManus Excellence in Teaching Award, University of Washington
2008	Crumpton/Baxter/Bonham Memorial Scholarship, San Francisco State University
2006	American Chemical Society Section Award
2006	Helen S. Jones Prize in Political Science, University of Rochester
2005	Catherine Block Memorial Prize in Science, University of Rochester
2005	Merck Scholar Award, University of Rochester

Professional experience

2009–2015	Graduate Research Assistant, School of Oceanography, University of Washington Advisor: Joseph Resing
2007–2009	Teacher, Oakland Unified School District, Oakland, CA
2006–2007	Research Scientist, Chemical Development, AMRI, Syracuse, NY
2004–2006	Research Assistant, Department of Chemistry, University of Rochester
2005	Undergraduate Summer Fellow, Woods Hole Oceanographic Institute
2004	Undergraduate Summer Fellow, Cornell Center for Materials Research, Cornell University
2003	Undergraduate Summer Fellow, Department of Chemistry, Syracuse University

Publications

<u>Manuscripts in preparation</u>

Barrett, P.M., Resing, J.A., Grand, M.M., Morton, P.L., Measures, C.I., and W.M. Landing. Trace element composition of suspended particulate matter from high-resolution sampling along meridional CLIVAR sections in the Indian sector of the Southern Ocean. in preparation for submission to Marine Chemistry.

Barrett, P.M., Resing, J.A., Grand, M.M., Morton, P.L., Measures, C.I., and W.M. Landing. Trace element composition of suspended particulate matter from high-resolution sampling in the Bay of Bengal and the South Indian subtropical gyre. in preparation for submission to Marine Chemistry.

Barrett, P.M., Buck, N.J., Zurbrick, C.M. and J.A. Resing. Comparison of ED-XRF and HR ICP-MS for analysis of the trace-element composition of marine particulate matter. in preparation for submission to Limnol. Oceanogr. Methods

Gambs, M., **Barrett, P.M**., and N. Dolsak. U.S. Congressional action on climate change: 1993–2012. in preparation for submission to Climatic Change.

Peer-reviewed articles

Barrett, P.M., Resing, J.A., Buck, N.J., Landing, W.M., Morton, P.L. and R.U. Shelley. 2015. Changes in the distribution of Al and Fe along A16N in the eastern North Atlantic Ocean between 2003 and 2013: Implications for changes in dust deposition. *Mar. Chem*. in press.

Grand, M.M., Measures, C.I., M.S., Hatta, M., Morton, P.L., **Barrett, P.M.,** Milne, A., Landing, W.M. and J.A. Resing. 2015. The impact of circulation and dust deposition in controlling the distributions of dissolved Fe and Al in the south Indian subtropical gyre. *Mar. Chem.* 176, 110–125.

Grand, M.M., Measures, C.I., Dinniman, M.S., Hatta, M., Hiscock, W.T., Landing, W.M., Morton, P.L., Buck, C.S., **Barrett, P.M.** and J.A. Resing. 2015. Dissolved Fe and Al in the upper 1000 m of the eastern Indian Ocean: a high-resolution transect along 95°E from the Antarctic margin to the Bay of Bengal. *Global Biogeochem. Cycles* 29, 375–396.

Resing, J.A. and **P.M. Barrett**. 2014. Ocean chemistry: Fingerprints of a trace nutrient. *Nature*, 511, 164–165.

Marsay, C.M., Sedwick, P.N., Dinniman, M.S., **Barrett, P.M.**, Mack, S. and D.J. McGillicuddy. 2014. Estimating the benthic efflux of dissolved iron on the Ross Sea continental shelf. *Geophys. Res. Lett.* 41, 7576–7583.

Barrett, P.M., Resing, J.A., Buck, N.J., Feely, R.A., Bullister, J., Buck, C.S., Landing, W.M. and C.I. Measures. 2014. Calcium carbonate dissolution in the upper 1000 m of the eastern North Atlantic. *Global Biogeochem. Cycles* 28, 386–397.

Barrett, P.M., Resing, J.A., Buck, N.J., Buck, C.S., Landing, W.M. and C.I. Measures. 2012. The trace element composition of suspended particulate matter in the upper 1000 m of the eastern North Atlantic Ocean: A16N. *Mar. Chem*. 142–144, 41-53.

Chiang, K.P., **Barrett, P.M.**, Smith, J.M., Kingsley, S., Brennessel, W.W., Clark, M.M., Lachicotte, R.J. and P.L. Holland. 2009. Ligand Dependence of Binding to Three-Coordinate Fe(II) Complexes. *Inorg. Chem*. 48, 5106–5116.

Selected presentations

Trace metal composition of suspended particulate matter along meridional and zonal CLIVAR sections in the Indian Ocean. AGU Fall Meeting, San Francisco, CA. 15–19 Dec. 2014. Poster.

Decadal comparison of particulate trace metal distributions along CLIVAR A16N: 2003–2013. Ocean Sciences Meeting, Honolulu, Hawaii, 23-28 Feb. 2014. Poster.

Impacts of Anthropogenic Emissions of Aerosol Metals on Surface Ocean Chemistry. American Meteorological Society Annual Meeting, Austin, TX. Jan 7, 2013.

Impacts of Anthropogenic Emissions of Aerosol Metals on Surface Ocean Chemistry. AGU Science Policy Conference, Washington, DC. Apr 30-May 5, 2012. Poster.

Aerosol Cu Inputs to the North Atlantic: Distributions and Sources. GEOTRACES workshop on Stable Isotopes of Biologically Important Trace Metals, London, UK. 13-14 Sept. 2012. Poster.

Estimating shallow-water $CaCO_3$ dissolution in the North Atlantic. Graduate Climate Conference, Pack Forest, WA. 26-28 Oct. 2012.

Lipid Biomarkers as Recorders of late Holocene Climate Variability. Ocean Sciences Meeting, Honolulu, Hawaii, 20-24 Feb. 2006. Poster.

Oceanographic field experience

May 2014	NOAA Mariana Archipelago Reef Assessment and Monitoring Program *NOAA Ship Hi'ialakai*, Maug (10 days) trace metal sampling, shipboard pH analysis
July–Oct 2013	CLIVAR/CO_2 Repeat Hydrography section A16N *NOAA Ship Ronald H. Brown*, North Atlantic Ocean (53 days) trace metal sampling
Dec 2011–Feb 2012	Processes Regulating Iron Supply at the Mesoscale (PRISM) *RVIB Nathaniel B. Palmer*, Ross Sea (49 days) trace metal sampling
May 2010	Exploration of NE Lau Basin *RV Kilo Moana*, NE Lau Basin (14 days) trace metal sampling, shipboard pH analysis, shipboard H_2S analysis

Teaching experience

2013	Co-Instructor, *Introduction to Oceanography*, University of Washington
2012	Teaching Assistant, *Introduction to Oceanography*, University of Washington
2011	Teaching Assistant, *The Changing Ocean*, University of Washington
2005	Teaching Assistant, *Physical Chemistry*, University of Rochester
2004	Teaching Assistant, *Organic Chemistry*, University of Rochester

Professional service and science outreach

2014	Abstract Committee Chair, Graduate Climate Conference
2014	Co-organizer, UW seminar series "*Ocean Change: Proactive Approaches*"
2014	seminar speaker, UW Forum on Science, Ethics, and Policy
2014	seminar speaker, UW Program on Climate Change
2013–present	Reviewer, Limnology & Oceanography
2011–2015	Volunteer, Orca Bowl (National Ocean Sciences Bowl) `
2010–2014	Volunteer Instructor, Ocean Inquiry Project